Tampere University

Mehedi Hasan Dhruba

DEVELOPMENT OF A MINIATURE CAPACITIVE SENSOR FOR LIQUID LEVEL MEASUREMENT IN ORGAN-ON-CHIP APPLICATIONS

Master of Science Thesis
Faculty of Medicine and Health Technology
Prof. Pasi Kallio
Jari Väliaho
June 2023

ABSTRACT

Mehedi Hasan Dhruba: Development of a miniature capacitive sensor for liquid level measurement in organ-on-chip application
Master of Science Thesis
Tampere University
Biomedical Micro and Nanodevices, Biomedical Sciences and Engineering
June 2023

Background and aim: Organ on chip (OOC) are multi-channel 3D microfluidic integrated circuits that mimic human mechanics, physiology and functions of a whole human organ and organ system. OOC devices offer a more realistic setting for studying biological responses to medicines and other stimuli because they imitate the shape and operation of human organs as microfluidic systems. However, for OOC devices to deliver exact and dependable findings, fluidic conditions must be precisely controlled. In organ-on-chip applications, liquid level monitoring is an important factor, especially in applications that use gravity-based pumping, which consists of an inlet and outlet chamber to measure and control the flow of the liquid. The aim of this thesis was to develop a capacitive interdigital sensor for organ-on-chip (OOC) applications that can measure liquid levels. Capacitive sensors were chosen due to their simplicity, linearity and easily accessibility. When the liquid level in the OOC device fluctuates, the sensor's capacitance varies, which can be measured. The size and shape of the sensor and the electrode geometry's design are important element for the sensor's sensitivity and accuracy.

Material and Method: After studying sensor geometry sensors were designed by AutoCAD and fabricated. The material for the substrate of the sensor was chosen PCB-FR4 because it is strong, water resistant and gives a good insulation layer. The sensor was fabricated and then soldered with copper wire then coated with Parylene C for the insulation layer and then tested with liquid DPBS (Dulbecco’s phosphate-buffered saline). Based on theory, 3 types of sensors, including different versions, were fabricated and tested and analyzed the data from the experiment. Type A consists of two single parallel electrodes with different dimensions and different gaps between electrodes. Type B consists of vertical finger electrodes with different dimensions for different versions based on 1-1-1 IDT sensor theory. Type C is horizontally placed finger electrodes where the gap between each electrode is same. In the experiment all the sensors then tested with different flow rate and the experiment were repeated to check the performance. Experiments were done both automatic and manual insertion and suction of liquid.

Results: In sensor characterization and comparison of data from different types of sensors, 1-1-1 IDT sensor Type B Version 3 had better average sensitivity compared to other versions of Type B as well as Type A and Type C sensors, including each version which was 3.92 pF/mm. The theoretical results of the sensor, like maximum capacitance and sensitivity, were almost close enough to the experimental results of the sensors, except there were some minor errors due to experimental limitations.

Conclusion: The sensor performance was quite good as it has high sensitivity, accuracy, and repeatability. Fabrication of the sensor is simple, fast, inexpensive, and easily accessible. The sensor can be customized as needed for the application. The findings show that the sensors are capable of accurately measuring liquid levels. Then sensor can be customized as needed for the application.

Keywords: Organ-on-Chip, Liquid Level Sensor, PCB-FR4, Sensitivity; Capacitance

PREFACE

First of all, I would like to express our gratitude to the Almighty, without whose consent nothing is achievable.

I would like to convey my heartiest gratitude and profound respect to my supervisor, Prof. Pasi Kallio and Jari Väliaho, for guiding me through this effort with their wholehearted support and encouragement. Their prudence and inspiration motivated me to work in this challenging field of biomedical engineering. This work would not have been feasible without the critical guidance, inspiration, and help of both, whose knowledge and ideas have been crucial in this research work.

I would also like to thank Antti Mäki, Joose Kreutzer, Kyriacos Yiannacou and Kaisa Tornberg for their input and contributions throughout my thesis period. I also want to express my profound gratitude to each and every member of the Micro- and Nanosystems Research Group and laboratory colleagues, whose unwavering encouragement and constructive criticism have been crucial at every point of this journey. Their input has helped me to improve my ideas and develop new skills.

Moreover, I would also like to show my gratitude to all my friends who supported me during the difficult times of this journey.

Last, but not least, I am obligated to thank my parents, whose love and guidance were the working forces behind every bit of success we have accomplished so far in our life.

Tampere, June 2023

Mehedi Hasan Dhruba

CONTENTS

LIST OF FIGURES

LIST OF TABLES

LIST OF SYMBOLS AND ABBREVIATIONS

OOC	Organ on Chip
IDT	Interdigital
AFE	Analog Front End
TOF	Times of Flight
FBG	Fiber Bragg Grating
STP	Standard Temperature and Pressure
PTFE	Polytetrafluoroethylene
PVC	Polyvinyl Chloride
PCB	Printed Circuit Board
SUT	Sample Under Test
WE	Working Electrodes
SE	Sensing Electrodes
DPBS	Dulbecco's Phosphate-Buffered Saline
RPM	Rotation per Minute
SNR	Signal to Noise Ratio
Nb-Ti	Niobium Titanium
LHe	Liquid Helium
N	Total Number of Received Samples
NDT	Non-Destructive Testing
C	Capacitance
C_{eq}	Equivalent Capacitance
Q	Charge
V_0	Voltage
ε_r	Relative Static Permittivity
ε_0	Permittivity of Free Space
n	Number of Electrodes
l	Length of Sensor
A	Electrode Area
d	Separation Distance
w	Electrode’s Width
h	Electrode height
T	Thickness
pF	Picofarads

π	Pi
λ	Wavelength
g	Gap Between Electrodes
$g(n)$	Random Variable
$v(n)$	Modulated Signal
Avg_A	Average Active Level
Avg_1	Average Inactive Level
$Noise_1$	Peak Noise

1. INTRODUCTION

Organ-on-chip (OOC) technology is a potential substitute for conventional in vitro and animal testing in drug discovery and toxicity screening [1]. OOC devices offer a relatively realistic setting for studying biological responses to medicines and other stimuli because they imitate the shape and operation of human organs as microfluidic systems. However, for OOC devices to deliver exact and dependable findings, fluidic conditions must be precisely controlled [2]. Real-time monitoring of liquid levels is a critical aspect that must be followed to guarantee the proper operation of OOC devices.

Due to their simplicity, accuracy, and affordability, capacitive sensors have become a popular method for measuring liquid levels [3]. The study presented in this thesis aims to develop a capacitive interdigital sensor for organ-on-chip (OOC) applications that can measure liquid levels. Interdigital sensors include electrodes that lock together to increase their surface area and increase sensitivity. Two electrode arrays that interlock and are separated by a dielectric layer make up the proposed capacitive interdigital sensor. As the liquid level in the OOC device fluctuates, the sensor's capacitance varies, which can be measured. To achieve great precision, selecting the proper dielectric layer between the electrodes is essential, and it should be based on the liquid's dielectric constant.

The size of the sensor and the electrode geometry's design are crucial components in determining a sensor's sensitivity and accuracy. It is expected that the capacitive interdigital sensor will perform better than traditional liquid-level monitoring methods. Due to its broad surface area, the sensor is more sensitive and can detect even minute changes in liquid level. Additionally, it is simple to produce and can be tailored to the OOC devices' dimensions. The sensor is straightforward to integrate into OOC devices and can be utilized in real-time monitoring systems.

There may be difficulties in developing a reliable capacitive interdigital sensor for OOC applications. The presence of air bubbles in the liquid, which might impair the sensor data accuracy, is one of the major difficulties. Another difficulty is the requirement for a reliable and strong signal conditioning circuit to measure capacitance changes accurately. Despite the challenges, creating a capacitive interdigital sensor for measuring liquid levels in OOC applications is a crucial and tough task to guarantee the precise operation and dependable results of OOC devices [4].

This thesis aims to develop a miniature capacitive sensor that can detect the changes at the liquid level to be used in organ-on-a-chip applications. The sensor's geometry and design were thoroughly studied to develop it, as shown in Figure 13 and Figure 14. After

the sensor's design was finalized, the sensors' materials were chosen, and the manufacturing was done. The sensor's surface was then coated with various materials, and contact angle measurements were conducted to ascertain its surface characteristics. The sensor was then evaluated for accuracy, reliability, and repeatability, and the findings were examined using MATLAB.

2. THEORETICAL BACKGROUND

In this Section background study related to the platform is presented. In Section 2.1 Organ on chip technology and the technical developments in the field are described and some notable advantages of using organ-on-chip technology are also included in the discussion, followed by examples of research works conducted in recent years. In Section 2.2, 3D vasculature in organ-on-chip is discussed. Liquid-level measurement and state-of-the-art measurement techniques of different liquid-level sensors are considered respectively in Sections 2.3 and 2.4. Section 2.5 represents about sensor coating, while SNR is explained in Section 2.6.

2.1 Organ-on-Chip (OOC):

The organ-on-a-chip technology is a fascinating advancement in science and technology that combines biology and microtechnology to imitate important aspects of the human body's physiology [5], [6]. Organ-on-a-chip is a relatively recent method for studying human pathophysiology and disease [7]. It is a rapidly evolving field that seeks to create miniature models of human organs using microfluidics. The term "organ" refers to the miniature tissues grown in these microfluidic chips, which can replicate the functions of one or more specific tissues[7]. Organ-on-chip technology is based on microfluidic cell cultures replicating human organ structures[5]. Though these systems are simpler than natural tissues and organs, they can often effectively replicate human physiology and disease [5]. The microfluidic device used in OOC technology contains an intricate network of micro-channels that can guide and manipulate small amounts of liquid, ranging from picolitres to milliliters [8]. The Organ-on-chip technology involves using microfluidic devices to replicate the microenvironment of various human organs, allowing researchers to do experiments on biological cells and tissues outside the body [6] with greater accuracy and control. The microscale permits more exact regulation of the tissue-supporting environment and intimate observation of cell and tissue activities.

Organ-on-chip technology has many potential applications in drug discovery, toxicology, understanding disease mechanisms and personalized medicine. In drug discovery, organ-on-chip can be used to test the effectiveness of new drugs on a miniature model of a specific organ, allowing researchers to screen for potentially harmful or ineffective compounds before testing them in animals or humans [9]. In toxicology, organ-on-chip models can be used to study the effects of toxins or chemicals on specific organs, helping to identify potential hazards and develop safer products[8]. In personalized medicine, organ-on-chip models can be used to understand the effects of drugs on individual patients, allowing for personalized treatment plans.[6]

One of the key advantages of organ-on-chip technology is its ability to replicate the complex microenvironment of human organs. Microfluidic devices can be designed to mimic the mechanical, electrical, and biochemical properties of various tissues, providing researchers with a more accurate representation of how drugs or toxins interact with human organs[7]. These devices can also study the interactions between different organs, allowing researchers to understand how diseases such as cancer metastasis or how drugs are metabolized in the body[8].

Organ-on-chip technology is currently in its early stages, and many challenges must be overcome before it can be widely adopted. One of the key challenges is the complexity of the microfabrication process required to create the devices. The devices must be fabricated with high precision to ensure the accuracy of the results, which can be time-consuming and expensive. Another challenge is integrating multiple organs into a single device, which requires complex fluidic networks and sophisticated control systems[10].

2.2 3D Vasculature Chip:

The human vasculature is a complex system of interconnected blood arteries shaped like a tree [11]. It eliminates waste and metabolites from the body and distributes essential nutrients, gases, cells, and signaling molecules [12]. Protected from the shear stress of blood flow, the vasculature also controls the blood's pH and osmolality.[13] Blood arteries are essential regulators of homeostasis, the immunological response, blood pressure, and tissue healing [14]. Including cancer and cardiovascular disorders, several illnesses are linked to aberrant vasculature form and function [15]. 3D cell culture and tissue engineering applications would benefit from incorporating microvasculature for more robust, representative, and long-lasting in vitro constructs [16].

The three main types of blood vessels that their structure and function can classify are arteries, veins, and capillaries [11]. They are further classified into subsets according to their size and placement in the circulatory system. The smaller arterioles branch off the main arteries and carry the blood to the organs and muscles of the body's periphery. Arterioles, found in most human tissues, connect the arterial side of the vascular tree to the capillary network. Venules branch off from the ends of the capillary beds and join larger veins. Blood is pumped back to the heart via the veins [11]. Arteries and veins have three layers: intima, media, and adventitia [17]. In the tunica intima's innermost layer, endothelial cells cover a basement membrane. Endothelial cells, using angiocrine signaling, create a selective interface between the circulatory system and the rest of the body[14]. Connective tissue, smooth muscle, and elastic fibers comprise the tunica media layer. To control blood flow distribution and blood pressure, smooth muscle cells

change the diameter (d) of blood arteries [18]. The tunica externa acts as a shield and a point of contact between the vessel and its surroundings. Collagenous connective tissue and perivascular nerve endings are found there[13]. Endothelial cells, a basement membrane, and pericytes all work together to form a single layer in capillaries. The vascular tree takes on a variety of features and functions. Capillary morphologies can be either continuous, fenestrated, or discontinuous, depending on the type of tissue they're located in[11].

Vasculogenesis and angiogenesis are processes that generate and modify blood vessels. During early embryonic development, vasculogenesis organizes angioblasts or endothelial precursor cells into a primitive vascular plexus to form first vessel architectures. The process of angiogenesis, in which new blood vessels grow into an existing network, is ongoing. At this point, the arterial-venous connection is predetermined. Blood flow is finally established when smooth muscle cells and pericytes seal and reinforce the freshly formed endothelial tubules. Despite their dormant state in adulthood, blood vessels can and do respond to angiogenic signals [19], [20].

3D vascular integration is frequently used in organ-on-chip systems to replicate the anatomy and operations of genuine organs. These applications seek to imitate the structure and functionality of human organs by integrating living cells onto microfluidic devices. The incorporation of 3D vasculature is particularly important since it makes it possible to replicate the complex web of blood arteries found in human organs. The organ tissues depend on the vasculature for the delivery of oxygen, nutrition, and necessary chemicals, as well as for the disposal of waste materials. Researchers can more precisely mimic the physiological circumstances and interactions between blood arteries and organ cells by using 3D vasculature.

Many methods, such as template-based construction, layer-by-layer deposition, 3D (bio)printing, and self-assembly, have been used to model and simulate vasculature on OOCs [15]. Single microchannels or networks of fluidic architecture can be formed using templates that are later removed or dissolved [21]. Templates are removed from solidified scaffolds to create a single structure resembling a blood vessel [22]. Moreover, 3D printing can make dummy prototypes of more sophisticated micro vessel networks [23]. Insufficiently wide microchannels cause seeded cells to congregate; hence this is the main constraint of templating [21], [24]. Moreover, the method is restricted to simple geometries, and removing templates introduces tension that could potentially harm the scaffold.

Layer-by-layer deposition is a build-up method in which layers of material are laid down in succession. Layer-by-layer deposition creates microstructures that are both intricate and precise to a higher degree than traditional templating does[15], [25]. Nevertheless, misalignment and insufficient layer adhesion pose challenges for developing a 3D vascular network from poly (ethylene glycol) diacrylate utilizing stereolithographic printing. Cell-matrix suspension can be layered on-chip directly using 3D bioprinting to create vascular architectures[26], [27]. Endothelial cells were seeded into the vessel lumen after the rod was removed and two layers of hollow filaments were printed with smooth muscle cells (inner layer) and fibroblasts (outer layer). By changing the rod's diameter and bending it into different shapes, we could create vessels of varying sizes and shapes [27].

Precursor cell-driven self-assembly of 3D microvasculature is the basis for models of vasculogenesis [21]. Strong 3D vascular networks can be formed in microfluidic devices by suspending endothelial cells (vascular structures) and vascular-supporting fibroblasts in a fibrin matrix [15], [23]. The microvasculature created by the vasculogenesis method is anatomically and physiologically relevant to that found in living organisms [15]. Hence, it has become generally considered to have less influence over biological processes and constituents than is possible with alternative approaches. A further self-assembly method is the modeling of angiogenesis [28], [29]. With this technique, a microchannel coated with endothelial cells serves as a miniature version of a bigger blood artery [30]. The directed sprouting of micro vasculature through a hydrogel scaffold is achieved by introducing a gradient of proangiogenic factors across the cell culture [30]. As interstitial flow controls angiogenic sprouting, it is typically included in vascular models [31].

2.3 Liquid Level Measurement:

Liquid level measurement is an important factor for OOC applications as well as for several domains of the industry. Liquid level measurement is a way to detect or measure the liquid level height in a tank or container, or Reservoir[32]. This technique is widely used in industries. Several industries use liquid level measurement to detect liquid leaks and measure diverse liquid kinds like chemicals, hazardous compounds, and multilayer liquids [33]. To process or store liquid, the liquid level must be precisely controlled. Additionally, since proximity sensing, location sensing, humidity sensing, and liquid sensing all operate according to similar principles, this field of study provides opportunities to investigate them. A few methods can be used to measure liquid levels, including ultrasonic, thermal, optical, hydrostatic pressure, conductance, and capacitance[34]. Liquid level measuring technologies frequently use computers to

calculate the information obtained in a device-readable manner from the sensor monitoring system in situations when many physical principles are at play. Digital processing techniques and modern electronics control and analyze data through embedded microprocessor-based digital computers [33].

The visual approach in Figure 1 shows a simplified representation of liquid level measurement on different types of liquid tanks. It is relatively expensive and requires careful setup to reduce level measuring errors brought on by light source interference with ambient light.

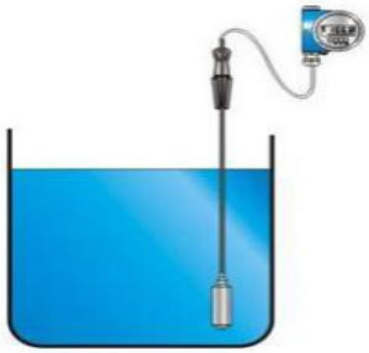

Figure 1: Liquid level measurement with sensor, image taken from Renkeer blog portal [32].

The use of an ultrasonic sensor necessitates a high-frequency signal source to generate and transmit ultrasonic waves, for that a crystal oscillator is used[35]. These waves are then used to measure the time of flight, which is the duration it takes for the ultrasonic signal to travel to an object and reflect back to the sensor, which ranges from a microsecond to a nanosecond. The piezoelectric transducer's fluctuating signal frequency impacts the ultrasonic sensor's output. It also displays the frequency drift brought on by changes in the surrounding temperature. In resistive liquid level sensors, a thin metal probe comprised of conductive materials, such as stainless steel or metal alloys, is frequently utilized. It functions on the theory that the electrical resistance changes depending on whether the liquid is present or not. The resistance of the sensor changes together with the liquid level. By measuring the sensor's resistance, the level of the liquid can be determined. Despite the resistive sensor's low cost of level measurement, it only works with conductive liquids and has a significant power consumption.

The capacitive sensor is the most practical liquid-level sensing method for insulating and conducting liquid [36]. High resolution, low-temperature error, low power consumption, high sensitivity, and the potential for noncontact level measurement are all features of

capacitive sensors. As a result, the capacitive approach is frequently used to measure liquid levels [36] [37]. The contact method, in which the electrodes are submerged in the liquid, and the noncontact approach, in which the electrodes are not in contact with the liquid, can be used to measure the level. The highly reliable and long-lasting sensor makes the noncontact approach very appealing and practical. Over time, electrodes submerged in liquid become polluted, which lowers their accuracy and durability. Moreover, the contact sensor needs to be maintained. This sort of sensor is not appropriate for liquids with a high viscosity and high chemical reactivity, such as paints, lubricants, and oils.

The most common topologies to create capacitive sensors are cylindrical, parallel, coaxial, or coplanar [38]. Most capacitive sensors measure level by contact. Planer interdigital (IDT) sensor is the coplanar sensor. It comprises of several parallel-plate capacitors that are wired together. The electrodes' front sides are exposed to the tested samples [39]. This straightforward IDT architecture offers the ability to measure fringing fields with extreme sensitivity. Several studies have employed coplanar IDT sensors for level measurement in recent years, but the main benefits of coplanar capacitive sensors are their low energy consumption and potential for noncontact level measurement[40]. In order to design liquid level transducers for measuring liquid levels in different industrial processes, factors for example, pressure at depth, thermal and electrical conductivity, relative electrical permittivity, buoyancy, absorption of radiation and liquid surface reflection of light or sound waves are taken into account. These characteristics of the liquid are utilized to create different types of liquid-level transducers that are appropriate for specific measurement requirements.

2.4 State of Art of Measurements Techniques:

2.4.1 Ultrasound Sensor:

The sensor stimulates and detects the echo after it returns for a single transducer in fluid identification, fluid level, and distance applications, as shown in Figure 2. High-frequency sound waves are used by an ultrasonic liquid-level sensor to detect the distance between the sensor and the liquid surface. A transducer that produces sound waves makes up the device. These waves pass through the atmosphere, arrive at the liquid's surface, and some of them are partially reflected to the sensor. Transducer detects reflected waves by switching to receive mode. The sensor measures the distance between itself and the liquid surface by calculating the time required for waves to go back and forth between the transducer and the liquid surface using the known speed of sound in the air. A typical Analog Front End (AFE) circuit works by exciting the transducer by the AFE by being hit

repeatedly with pulses between kHz and MHz frequencies. The sensor is excited with up to 31 pulses at a time, with a frequency range of 31.25 kHz to 4 MHz. A START pulse shows the sensor's excitation; therefore, a STOP pulse indicates the echo. The distance, fluid level, and fluid ID/concentration are all shown by the time difference between the START and STOP times of flight (TOF) [41].

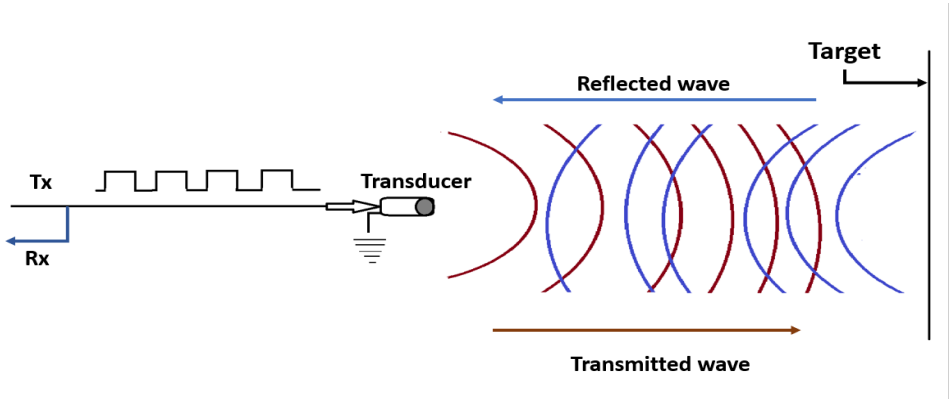

Figure 2: Working process of ultrasonic for single transducer [41].

The other type makes use of the transducers in a pitch-and-catch manner for dual transducer applications such as flow meters Figure 3. In this technique, transducer A is excited while transducer B serves as a receiver to produce STOP pulses. The gap between the transducers is shown by the time-of-flight (TOF_{AB}) between the stimulation and STOP pulses. To determine the flow of medium (gas or water) between the two transducers, a differential ToF, TOF_{AB} - TOF_{BA}, must be performed [41].

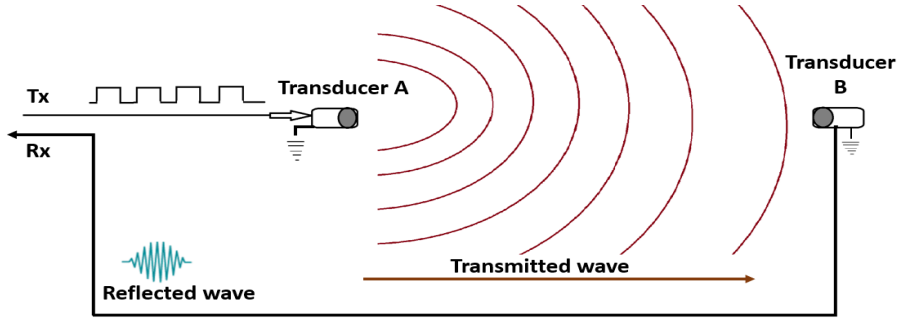

Figure 3: Working process of ultrasonic for dual transducer [41].

2.4.2 Differential Pressure Sensor:

The measurement of liquid level can be accomplished by a differential pressure level sensor. This kind of sensor makes use of the difference in pressure that exists between the internal pressure of the vessel and the fluid's hydrostatic pressure at the base of the container. The ratio of the liquid density to the liquid height in the container is calculated to get the difference in hydrostatic pressure. The atmospheric pressure is used as a

reference point by including a vent at the top of the tank to maintain that pressure inside the empty area. Differential pressure sensors can also be used in pressurized vessels as long as the reference pressure port, which is the low-pressure side, is linked to a port in the vessel located above the maximum fill level[42]. Depending on transmitter location and the process of the physical conditions related to the process connections, bubblers or liquid purges may still be necessary. Figure 4 shows a simplified representation of the differential pressure sensor.

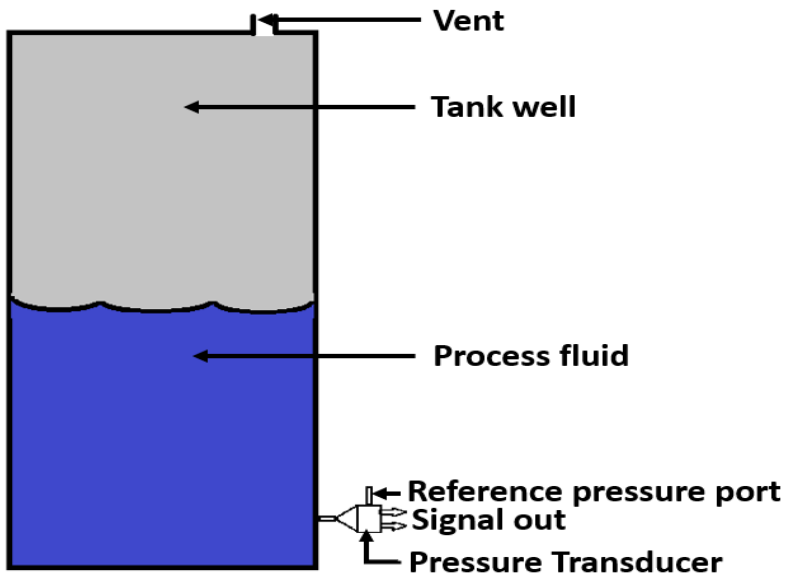

Figure 4: Differential pressure sensors monitor for the process fluid level [42].

2.4.3 Thermal Sensor:

Thermal sensors are used in the liquid-level measurement. One example that is presented here is a special sensor that is used for liquid Helium measurements. The working principal is explained to understand how the thermal sensors work in liquid-level measurements.

One form of a thermal liquid level sensor consists of a Nb-Ti wire as well as a small heater located at the top in series with the wire. The main purpose of the heater at the top is to start the thermal quench of the upper part of the sensor wire, which is exposed to cold helium gas. This results in a reduction in the joule heat load that is transferred to the liquid when the cold helium gas moves upwards along with the wire because of the natural convection flow. The current is applied to the sensor in series, and the voltage is measured throughout the superconducting wire. Figure 5 shows a schematic diagram of the thermal level sensor. The basic principle behind this sensor is that the portion of the

superconducting niobium wire submerged in LHe has zero resistance, while the area that is in contact with the gas phase exhibits practically constant resistance at the operating current [43].

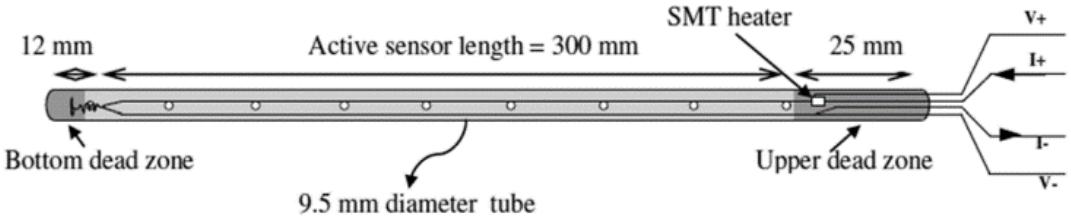

Figure 5: Schematic diagram of the thermal level sensor [44].

The resistance of the wire that is measured changes in proportion to the length of the sensor exposed to cold helium gas, which is influenced by the liquid level. An electronic meter interprets the opposite linear correlation between the voltage across the wire and the level of the liquid and shows the level that corresponds to it [44].

2.4.4 Optical Sensor:

Optical level measurement sensors work by using the principles of light reflection and refraction to detect changes in the level of a liquid or solid material. The basic working principle of an optical-level measurement sensor involves a light source, a receiver, and a prism or lens. The light source emits a beam of light that is aimed toward the material being measured. The light either passes through the material or is reflected back toward the receiver, depending on the properties of the material. If the material is transparent, the light will pass through it, and the receiver will detect the light that is transmitted through the material. However, if the material is opaque, the light will be reflected back toward the receiver [45].

The sensor detects the level of the material based on the amount of light that is reflected or transmitted through the material. As the level of the material changes, the amount of light that is reflected or transmitted also changes. The sensor can then convert this change in light into a signal that can be used to determine the level of the material. Different types of optical level measurement sensors use different techniques to detect changes in light, such as the use of prisms, lenses, or fiber-optic cables. They can be used to measure the level of liquids, powders, and solids and are often used in industrial applications where accurate level measurement is important [46].

2.4.5 Optical Fiber Based Sensor:

Various innovative techniques have been developed to enhance the performance of liquid level measurement, such as linear, accurate, repeatable, reliable, retrofittable, recalibrable, versatile, long-lasting, simple, durable, and inexpensive methods. Among these techniques, optical fiber sensors have experienced significant advancement in recent years. Initially used as point-level switches, optical fiber sensors have been developed in various ways to measure liquid levels using light transmission and reflection, with most of them being based on the effect of liquid refraction indices on the characteristics of optical fibers [47]–[49]. Typically, when an optical fiber meets a liquid's outer surface, it results in a loss of internal reflection of guided electromagnetic waves. To achieve continuous liquid level measurement, a fiber Bragg grating (FBG) optical fiber sensor is commonly used[50]. A reliable liquid-level sensor with good linearity, repeatability, and hysteresis can be achieved by integrating a fiber Bragg grating in a cantilever to measure the bending of the optical fiber [50]. However, this method requires mechanical apparatus, particularly in pressure containers, and is dependent on the specific gravity (the relative weight of that liquid compared to an equal volume of water) of the liquid. Recently, two novel liquid level measurements were developed that simultaneously measure the unknown level and specific gravity of the liquid, using dual-pressure-sensor and dual-optical-fiber systems, both utilizing FBG level sensors and Fabry-Pérot pressure sensors [50]. As the sensitivity and repeatability of these sensors increased, so did their capabilities. With periodic calibration, a liquid-level gauge which is an intensity-based fiber-optic, can continually gauge the levels of all types of liquids [51].

The operation of two optical level sensors is coordinated. Both systems use a right-angle prism as a sensor; however, one has the hypotenuse face down and the other has the shorter face pointing downward. The gradient-index lens collimator collimates the light from the optical fiber, which then propagates parallel to the optical axis. It precisely strikes the right-angle prism's face at a 45-degree incident angle because of the prism's geometric design. The light is then refracted into the same fiber after being reflected back from the prism. The full amount of light is reflected into the fiber when the sensor is in a vapour environment because the 45-degree angle is greater than the critical angle. An optical fiber-based liquid level sensor is shown in Figure 6 below.

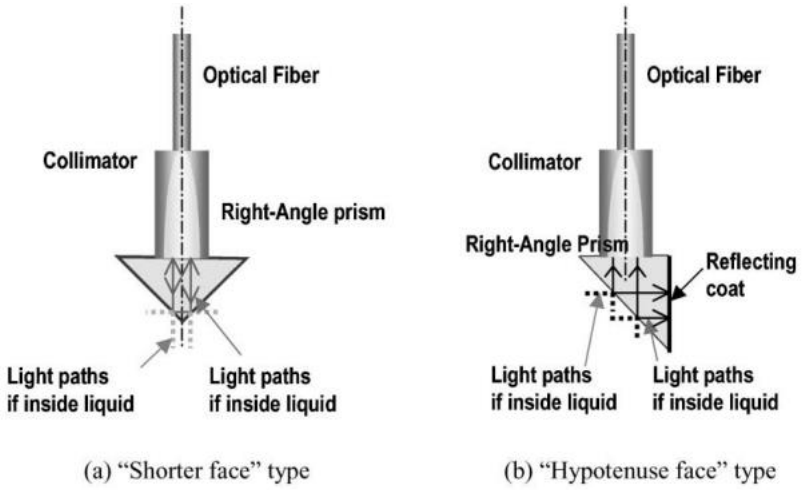

Figure 6: Optical fiber-based liquid level sensor [47].

When the sensor is near a liquid, the critical angle is smaller than the incident angle of 45 degrees, which causes the majority of the light energy to be refracted into the liquid. It is feasible to detect whether the probe is in a liquid or vapor environment by measuring the brightness of the reflected light. The position of the sensing point is the primary distinction between the two types of sensors. The light is reflected from the shorter face of the prism around the prism's tip in the "shorter face" sensor. The light reflects in the center of the hypotenuse surface of the prism in the "hypotenuse face" sensor, in contrast [47].

Optical fiber-based optical sensors are widely used for a variety of applications. These types of sensors analyze changes in the characteristics of light interacting with the substance. Absorption spectroscopy is a well-established optical technique for identifying sample chemical composition. A lot of existing work is done on the basis of optrode structures or complex waveguide. These types of waveguides are custom fabricated. For single and double-wavelength measurements, laser diodes or LEDs are used. Some other approaches utilize round-section glass capillaries [52].

2.4.6 Capacitive Sensor:

Capacitive sensors operate by identifying alterations in the electrical capacitance that exists between two plates [53]. These modifications are influenced by the gap between the plates, their surface area, and the dielectric constant of the material that lies between them. Any modification in these aspects can be interpreted into an electrical signal, which can be evaluated and interpreted [54].

$$C = f(d, A, \varepsilon_r) \tag{1}$$

A dielectric, a non-conductive material with a property called permittivity (ε_r) (or dielectric constant), serves as the fundamental component of a capacitor. Capacitance, measured in Farads (F), indicates how much charge *Q* a capacitor can store at a particular voltage V. By applying a voltage to the transmitting electrode, an electric field is generated between the two electrodes of the capacitor. A key characteristic of a capacitive sensor is that its capacitance changes in response to alterations in the electric field caused by different materials utilized to separate the electrodes. As an example, the capacitance of a capacitor with two parallel plates can be represented by[36]:

$$C = \varepsilon_r \varepsilon_0 \frac{A}{d} \tag{2}$$

Where *C* represents the capacitance; ε_r expresses as relative static permittivity; ε_0 represents permittivity of free space; *A* is expressed as electrode area, and *d* is the gap between parallel plates.

Capacitive sensors can identify the existence of dielectric substances, such as water, by detecting changes in capacitance that result from differences in permittivity between air and water. Under Standard Temperature and Pressure (STP) conditions, the permittivity of air ($\varepsilon_r \approx 1$) is significantly lower than that of water ($\varepsilon_r \approx 80$). This dissimilarity in permittivity enables the capacitive sensor to identify and gauge the presence of water by detecting changes in the dielectric substance, which impacts its capacitance.

Capacitive sensors are widely used in both industrial and automotive environments for a variety of applications. These sensors are able to convert changes in the position or properties of dielectric materials into electrical signals. While most capacitors are designed to have a fixed physical structure, various factors can cause changes in the structure of the capacitor, which can then be used for sensing. Capacitive sensors can be designed in various shapes and structures for their sensing electrodes. The quantity and complexity of the system variables used in an application determine the number of electrodes and their placement. A single sensing device, such as a concentric ring sensor, is adequate for proximity estimation based on capacitance in straightforward situations like proximity or displacement measurement, where capacitance values immediately represent the distance of a target item. However, a sensor array can be used in more complicated applications like imaging or non-destructive testing (NDT) to collect many readings for activities like image reconstruction or parameter estimation. For a precise analysis, it is essential to have a thorough understanding of how capacitance measurements relate to system factors[55]. The arrangement of electrodes, encompassing their shape, spacing, and separation, is a critical aspect that determines the performance of the sensor[56]. Electrodes can have either simple shapes like square,

round, rectangular, or ring-shaped or more intricate forms like comb or spiral shapes. The geometry of electrodes significantly impacts the sensor's performance in terms of penetration depth, signal strength, and measurement sensitivity. The gap between electrodes pertains to the distance between the centers of two neighboring electrodes, while the separation of electrodes signifies the width of empty gap between adjacent electrodes. These capacitive sensors' main benefits included their low cost, low power consumption, linearity, simplicity of application-specific modification, and appropriateness for usage in severe environments.

The concepts behind a capacitor can be utilized to measure the quantity of liquid present in a storage tank [57]. In a typical capacitive-level sensing setup, two electrodes are employed for a non-metallic tank, while a single electrode is employed for a conducting tank. Calculating the capacitance between the conductors immersed in the liquid can determine the fluid level as long as the distance between the two terminals is fixed. As fluids fill up the gap between the two parallel rods, the capacitance of the measuring cell increases proportionally to the dielectric constant, thereby determining the fluid height. One electrode function as a sensing electrode, and the other functions as a drive electrode. An excitation voltage is delivered using the rive electrode to gauge the liquid level and detected using the sense electrode.

Capacitive Sensor Types and Liquid Level Measurement:

Different types of liquid-level transducers utilize properties of liquids, such as buoyancy, pressure, permittivity, conductivity, and absorption. It is mainly due to the physical or chemical reactions between the probe material and the liquid. The exact origins of capacitive water level sensors are unclear, Bera et al. [58] proposed a low-cost, noncontact capacitive technique for measuring conducting liquid levels. Their method aims to overcome the limitations of conventional noncontact capacitance-type probes by using a uniform right circular cylinder made of insulating materials like glass, ceramic, nylon, PVC, etc., as the dielectric material of the cylindrical capacitor.

Numerous research publications have introduced capacitive sensors as a solution for practical water-level measurement [4], [59], [60]. Chetpattananondh et al. [57] analyzed designing and constructing a water-level measurement system based on an interdigital capacitive sensor. The system consists of a printed circuit board (PCB) with two interpenetrating finger electrodes, and the capacitance between parallel finger electrodes varies with the water level. To measure the change in capacitance, a signal conditioning circuit has been developed to record the discharge time of the interdigital electrode. According to the experimental results, the proposed sensor has good

reliability, repeatability, linearity, non-recalibration, resolution, cost-effectiveness, ease of use, portability, and low power consumption [57]. Additionally, the sensor can display real-time waveform data for a range of flood levels through an experiment that simulates a flood and can be used for monitoring river or open channel flood levels [61].

Two main categories of capacitive level sensors are employed to measure water levels: contact-based and noncontact-based. Reverter et al. [59] conducted a study that included a remote grounded capacitive sensor for liquid level measurement. The electrode of this sensor is made of polytetrafluoroethylene (PTFE)-insulated wire and stainless-steel rod. Bera et al. [58] developed a low-cost capacitance-based level sensor that is noncontact and reduces the impact of air in the dielectric for a conducting liquid. They also presented a modified capacitance-based level sensor that eliminates the effect of the self-inductance of the metallic rod for any type of liquid. Guirong et al. [62] proposed a capacitive liquid level sensor that can measure the gradient direction and angle incrementally in addition to the liquid level. This sensor uses four electrodes. In addition, Sheroz Khan et al. [63] designed a low-cost noncontact capacitance-based liquid level sensor that employs a circular cylinder made of polyvinyl chloride (PVC) as the dielectric for the capacitive sensor.

Furthermore, there are two primary types of capacitive sensors: grounded capacitive sensors and floating capacitive sensors. Floating-type capacitive sensors have the advantage of being inherently resistant to stray capacitances [64]. Stray capacitance is the unexpected and undesired capacitance in a circuit. Any two-surface placed close to each other with different electric potentials, which can create electric fields, can act like a capacitor, and can have a capacitance that is unexpected, that is, stray capacitance. However, grounded capacitive sensors are still required in certain applications, such as level monitoring of conductive liquids in grounded metallic containers, due to safety concerns and/or working limitations of floating capacitive sensors. Reverter et al. [59] [65] created and implemented a distant grounded capacitive sensor-based liquid-level measurement system. Khan et al. [63] developed a new noncontact capacitance-type with polyvinyl chloride (PVC) made uniform circular cylinder-level transducer for liquid identification purposes. The use of PVC also reduced the overall cost of the sensor.

Most capacitive-level sensors rely on approximations due to the differences in dielectric constants between liquids and air. However, in 2009, Canbolta proposed a technique to eliminate the impact of air and accurately measure liquid levels in tanks. The methodology was based on capacitance measurements from three parallel plate capacitive structures. These are used as level, reference, and air sensors. The process completely removes the influence of several variables, such as air and temperature, on

the data. This method has been proven mathematically to remove the influence of other factors, such as air and temperature, that can affect readings [4].

Guirong et al. [62] [66] suggested a capacitive liquid-level sensor consisting of four electrodes that can assess both the liquid level and vessel gradient state. This method has been experimentally validated by the authors. Typically, a capacitive sensor with two identical electrodes is used to monitor liquid levels in non-metallic storage tanks, although Bera et al. [58] suggest that it can also be utilized in both conductive and non-conductive liquids storage tanks, which are metallic or non-metallic. Liquids that may conduct electricity are known as conducting liquids because they contain ions. The dissolved ions or ionized molecules in these liquids help the electrical charge to move through them. Non-conductors are liquids that stop electricity from moving through them. Ions, which are electrically charged mobile particles that may carry electrical charges, are absent from these liquids. In contact liquid level measurement, the level measurement tool makes direct physical contact with the liquid. This technique depends on direct touch or immersion with the liquid surface. On the other hand, As the name implies, non-contact liquid level measurement avoids establishing direct physical contact with the liquid. Instead, the level is measured using remote sensing methods.

2.4.7 Interdigital Capacitive Sensor:

An interdigital capacitive sensor consists of a coplanar structure composed of several comb electrodes that are interpenetrating [39]. This sensor operates using a similar principle to that of two parallel plate capacitors. A schematic diagram shown in Figure 7 represents how a parallel plate capacitor can be converted into an interdigital capacitive sensor [35]. By applying different potentials to the comb electrodes, fringing fields are created between the positive and negative electrodes. When the sample under test (SUT) comes into contact with the comb electrode, these fields move through it from the positive electrode to the negative electrode [61]. Consequently, the conductance and capacitance between the electrodes are affected by the geometry of both the electrodes and the sample being tested, as well as the dielectric properties of the sample.

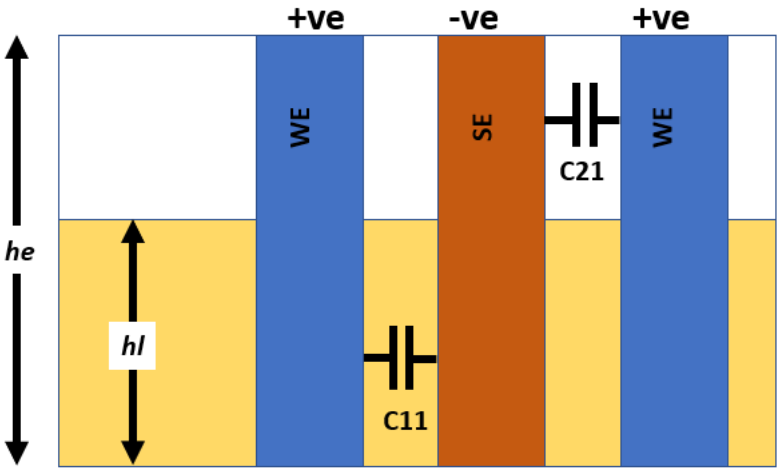

Figure 7: Schematic diagram of 1-1-1 interdigital sensor, images taken and modified from [35].

It works on the same principle as two parallel plate capacitors and can be converted from the latter using a diagram. The creation of fringing fields between the negative and positive electrodes is achieved by applying different potentials to the comb electrodes. These fields move through it from positive to negative electrodes when a contact is made between the comb electrode and SUT[61]. The geometry of both the electrodes and the sample being tested, as well as the dielectric characteristics of the sample, affect the conductance and capacitance between the electrodes [67]–[69].

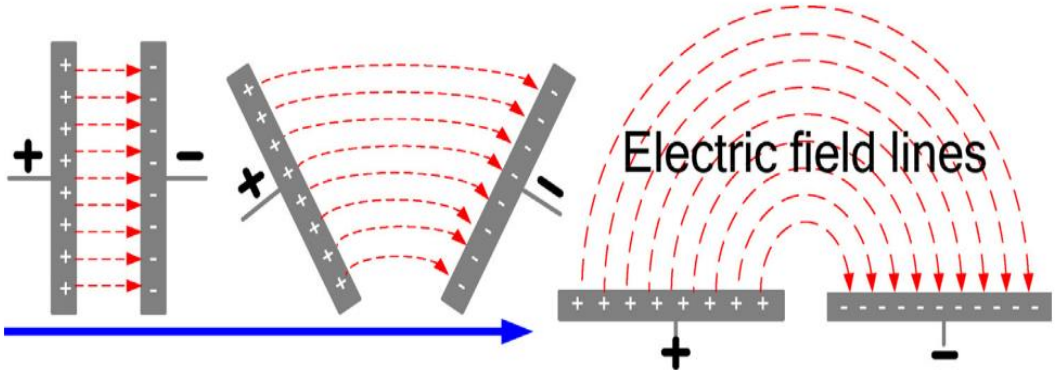

Figure 8: Interdigital sensor operating principle [67].

The capacitance measurement associated with water and air can be the basis for one common configuration of the interdigital capacitive sensor. Figure 9 displays the schematic for an interdigital capacitive water level sensor. The printed circuit board with FR4 substrate and a thin layer of a water-resistant insulation layer called liquid photo imageable solder mark are used to create the sensor design [57].

.

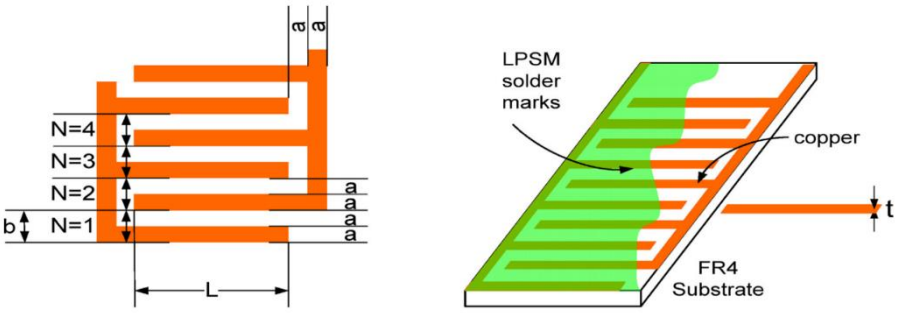

Figure 9: Typical interdigital capacitive sensor schematic drawing [57].

The illustration of the coplanar interdigitated (IDT) design of a sensor device that can be utilized for liquid-level assessment in shown in Figure 10. This sensor can be used for noncontact level detection on the wall of a liquid container. The working electrodes (WE) and sensing electrodes (SE) on the IDT's N number of fingers are evenly spaced apart. The length, width, and wavelength of the fingers are given in units of *L*, *w,* and *λ*, respectively (length between two fingers on the same side of the IDT). The sample under test (SUT) is contacted by a sensor that has a relative permittivity of ε_r and a height of SUT is *T*. An electric potential of ±V is applied to excite the electrodes, which enables electric field lines to pass through the dielectric SUT from positive electrode to the negative one.

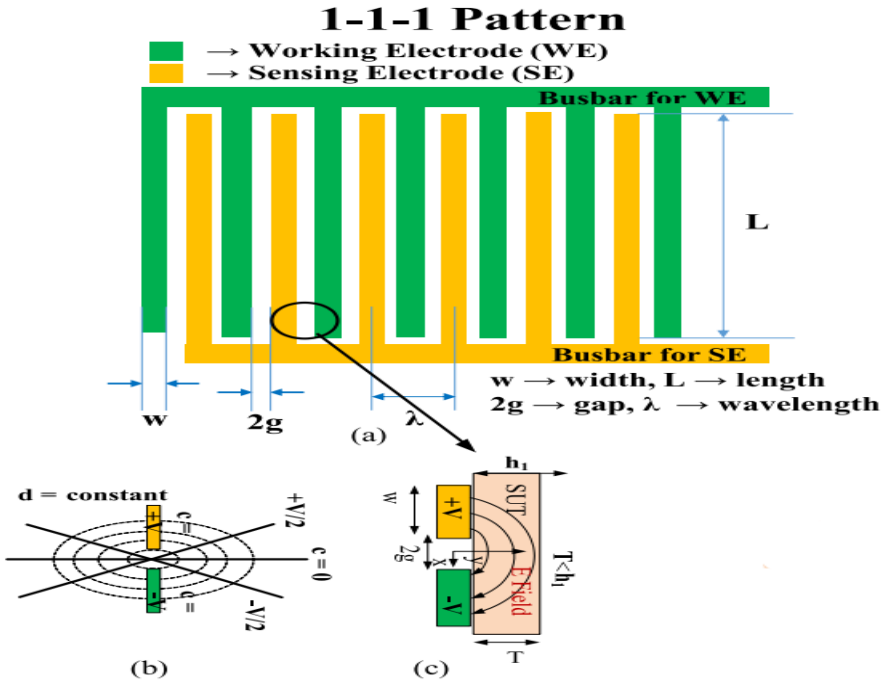

Figure 10: (a) The schematic diagram of the IDT structure (b) Distribution of electric field due to potential difference between the WE and SE (c) Penetration of electric field while $T<h_1$ [40].

The maximum height that the liquid can reach is h. The electrode's width is assumed to be much larger than the distance between its electrodes (*w* >> *2g*). Figure 10(b) shows an enlarged view of two semi-infinite coplanar parallel plate electrodes, which is separated by a distance of *2g*. From Figure 10(b) by using the conformal mapping technique the two-dimensional distribution of the electrode field can be solved and the inverse-cosine transform. The results of the conformal mapping solution can provide an approximate expression for capacitance [40].

Then capacitance value of two coplanar electrodes having *l* >> *w* and $\frac{W}{g} \gg 1$ 1 is given by [69]–[71],

$$C_{1,1} = \frac{Q}{2V_0} = \frac{2\varepsilon_r\varepsilon_0 l}{g\pi}\int_g^{g+w} \frac{1}{\sqrt{\left(\frac{x}{g}\right)^2 - 1}}dx \tag{3}$$

$$C_{1,1} = \frac{2\varepsilon_r\varepsilon_0 l}{\pi} ln\left[\left(1+\frac{w}{g}\right) + \sqrt{\left(1+\frac{w}{g}\right)^2 - 1}\right] \tag{4}$$

where $C_{1,1}$ = equivalent capacitance between two electrodes and

Q = charge

For the configuration of a 1-n-1 IDT sensor, the value of capacitance between WE and SE can be obtained by [71],

$$C_{1,n} = \frac{2\varepsilon_r\varepsilon_0 l}{g\pi}\int_{\frac{(n-1)}{2}w+ng}^{\frac{(n-1)}{2}w+ng+w} \frac{1}{\sqrt{\left(\frac{x}{g}\right)^2 - 1}}dx \tag{5}$$

As shown in Figure 11, the total equivalent capacitance for an approximation of 13 electrodes in a 1-1-1 configuration would be,

$$C_{eq,1-1-1} = 12C_{1,1} \tag{6}$$

Where the arrangement of interdigital electrodes on the sensor surface is defined with the term "1-n-1 configuration". The term corresponds to the pattern of electrode pairs used for the sensor. The 1-n-1 configuration is composed of a single electrode at one end, followed by a series of "n" interdigital electrode pairs. The electrode is then completed with another single electrode at the opposite end. Where "n" is used to represent the number of interdigital electrode pairs in between the two single electrodes.

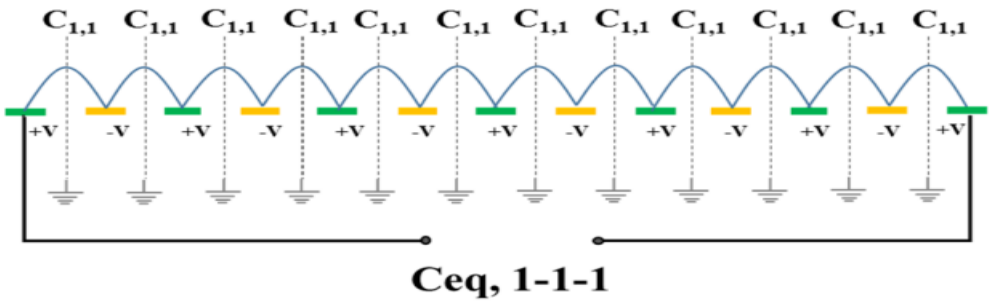

Figure 11: Total equivalent capacitance for 1-1-1 configuration [40].

After studying the sensor's working principle and based on previous research work done for liquid level measurements, the designed and selected sensor for this study is a floating interdigital capacitive sensor.

2.4.8 Example and Features of Commercial Liquid Level Sensor:

Table 1 shows selected commercially available liquid-level measurement sensors with some crucial features that are essential for the sensor's performance.

Table 1: Examples of commercial liquid level sensor

Ultrasonic Sensor	
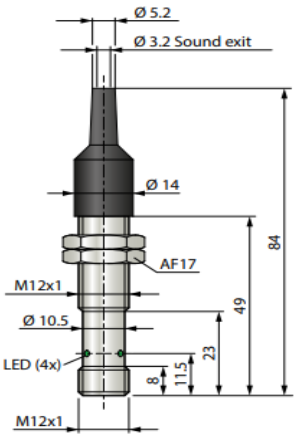	Details Probe length: up to 0.125 mm Output: 0-10 V and 4-20 mA Process pressure range: 1...10 bar Process temperature range: -25...+70 °C Measurement Accuracy: 0 to 50 mm with maximum linearity of <0.4 [%]
Capacitive Sensor	

	Details Probe length: 500 mm Output: 4-20 mA Process pressure range: 1...10 bar Process temperature range: 40...100 °C Measurement Accuracy: ± 1% of the upper limit of the measured value.
Resistive Sensor	
	Details Output Voltage: 5V Process temperature range: 40...85 °C Measurement Accuracy: Only can detect the liquid presence, cannot measure the liquid level
Optical Sensor	
	Details Output: 100 mA Switching current: Maximum 2.5 mA Process temperature range: -40...125 °C Liquid detection: Only can detect the liquid presence, cannot measure the liquid level

Parameters like temperature, measurement accuracy and resolution have an impact on the measurement data. Due to the thermal expansion or contraction of the liquid and the sensing elements, the temperature can have an impact on liquid level readings. Temperature fluctuations can affect a liquid's density and volume, which can result in errors in the liquid level being measured. Increased accuracy results in more reliable and accurate measurements. To reliably measure liquid levels, sensors or other equipment need to be calibrated and have a high degree of precision. By employing the proper installation, calibration, and compensating methods, accuracy can be increased. The

resolution establishes the degree of fineness or detail in the measurement. More precisely, it is possible to distinguish between various liquid levels with higher resolution.

A comparison table between some liquid-level measurement sensors focuses on their advantages and disadvantages [72], [73]. The table is given below:

Table 2: Advantages and disadvantages of different sensors.

Sensor Type	Advantages	Disadvantages
Ultrasonic	• The result is not dependent on the colour of the air-liquid or the reflectivity of the interface. • Contactless measurement method. • No moving parts.	• Needs to have a minimum measuring distance. • Output depends on the environmental condition. • Relatively expensive.
Capacitive	• Compatible with a vast range of liquids. • Compatible with a vast range of tank shapes.	• Needs to select suitable electrodes. • Constant distance between two electrodes should be maintained.
Resistive	• Simple in construction. • Offers good dynamic range. • It is much more durable compared to other sensors.	• Non-linear response. • Low sensitivity. • Higher power consumption.
Optical	• Noncontact method. • Fast response time.	• Not good for opaque liquid. • Not good for highly reflective liquid.
Thermal	• It can measure both high and low levels accurately. • Suitable for use in complicated device implementations.	• Requires contact with the liquid that can pose contamination risks.

Some commercially available sensors names and the manufacturer name with the price of the sensor, a table is shown below:

Table 3: List of liquid-level sensors and companies with references

Sensor name	Company info or link	Price	Flow rate	ink or website
Capacitive	Endress+Hauser	537.60 euros	Can measure the level of liquid, not flow rate	link capative [74]
Thermal	Elveflow	1550 Euros	From 0.07 to 5000 µL/min	Link Thermal 1 [75]
	Bronkhost	Not available on public domain	Not available on public domain	Link Thermal 2 [76]
Optical	Elveflow	Enquired through email. No response received	Not available on public domain	Link Optical1 [77]
Pressure Sensor	LabSmith	Contacted for price	7.5 µL	LinkP sensor1 [78]
Ultrasonic	WayCon Positionsmesstechnik GmbH	Contacted for price and delivery time.	Not available on public domain	Link Ultrasonic 1 [79]
	Baumer in Switzerland	456.32 euros	Not available on public domain	Link Ultrasonic 2 [79]

2.5 Coating:

A sensor's coating or substrate responds to changes in the number of certain molecules and ions in the fluid around it by engaging in adsorption and absorption processes. The coating substrate itself can contain the selective, sensitive layer of the sensor. Furthermore, it can be accompanied by diffusion and mass transfer. Making sure that the sensor's reaction is reversible is essential when the sensitive layer or substrate is used to increase signal strength. The sensor's durability and reliability are reduced by irreversible changes.

2.5.1 Parylene Coating:

Parylene is nowadays widely used in many applications for coating substrates. Parylene coating is convenient due to its properties. Parylene allows to form of a thin layer on top of electrodes. The commercially available types of parylene are parylene N, parylene C, parylene D, F-VT4, and parylene F-AF4.

Parylene should be able to endure constant exposure at a temperature of 220 degrees Celsius for the same amount of time in vacuum or inert atmospheres. While the expected lifespan of parylene is ten years of continuous exposure to air at a temperature of 100 degrees Celsius. Parylene has the propensity to link components, disengage from edges, or infiltrate into undesirable places, unlike most conformal coatings applied on a wider scale by spraying or dipping. [80].

Parylene C is the most widely used material because of both its barrier and dielectric properties. The aromatic hydrogen with a chlorine atom in parylene C contributes to its exceptionally low permeability. Because of this distinct feature, Parylene C is a suitable choice for enhanced resistance to moisture, chemicals, and corrosive gases[80] [81]. The polymer series is typically referred to as parylenes. Poly-p-xylylene, a totally linear and extremely crystalline material, is the series' principal member. It is referred to as parylene N particularly. The second product in the series, parylene C, is essentially the same monomer but differs in that one of the aromatic hydrogen atoms has been replaced with a chlorine atom.

Components are firmly positioned within a vacuum coating chamber, while a vaporizer is loaded with a powdered form of the parylene dimer. The parylene dimer is then heated within the vaporizer, causing it to change from a solid to a gaseous form. [82]The vaporized dimer is then directed into the pyrolysis furnace, where it is heated further, resulting in the conversion of the dimer gas into monomer vapor. [82]The highly excited monomer vapor is finally placed into a room-temperature deposition chamber with all parts fixedly positioned. The individual monomers in this chamber create bonds with one another and polymerize on all surfaces, resulting in the production of a thin and remarkably conformal covering through the deposition process. [80], [82].

2.5.2 Spin Coating:

Over the past few decades, spin coating has been a well-liked technique for creating thin films. The method is frequently used to create thin, homogeneous films on flat substrates. The substrate is rotated at high speed, typically around 3000 rpm [83]. A small amount

of liquid material is dispensed into the center of a substrate and spun quickly. The resin substance spreads outward as a result of the rotation's centrifugal force, finally reaching the substrate's edge and producing a thin resin layer on its surface. During spin coating, the substrate is rotated continuously until the appropriate film thickness is reached, at which point the fluid substance is spun off the substrate's edges. A Simplified illustration of spin coating is shown in Figure 12 below.

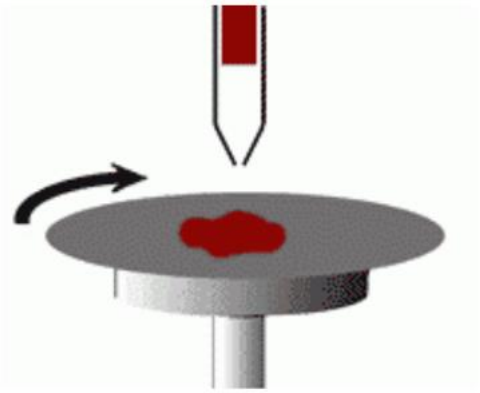

Figure 12: Simplified illustration of spin coating technique [84].

The physical features of the resin are its viscosity, drying rate, percentage of particles, and surface tension, which affect the final qualities and thickness of the deposited layer etc. [85]. Repeatability is essential to spin coating since even little deviations can significantly impact the thickness and caliber of the deposited film. This is because the process is sensitive to changes in these parameters. This technique is frequently used in photolithography to deposit photoresist layers on the substrate. Additionally, spin coating is also widely used in micro-fabrication to make films with a thickness of less than 10 nm.

2.6 Signal to Noise Ratio (SNR):

SNR represents the signal-to-noise ratio. SNR provides information on the ratio of signal power to noise power. The mathematical equation to obtain SNR is given as[86]:

$$SNR = 10 \times log_{10}\left[\frac{\frac{1}{N}\sum_{n=1}^{N}|v(n)|^2}{\frac{1}{N}\sum_{n=1}^{N}|g(n)|^2}\right] \quad (7)$$

Where, *g(n)* is a random variable, *v(n)* is the modulated signal, and *N* represents the total number of received samples, n=1, 2, 3 ……. N

SNR gives an approximate idea of how likely erroneous switching is to occur as well as a way to compare how well different implementations perform in comparison for different capacitive sensors.

Another way of calculating the SNR for capacitive sensors is by measuring the average active level, deducting the average Inactive level, and dividing the result by the peak noise level seen on the Inactive level. Capacitance or digital counts can be used to measure this. The alternative formula for SNR calculation can be written as [87]:

$$SNR = \frac{[Avg_A - Avg_I]}{Noise_I} \quad (8)$$

Where Avg_A is average active level, $Avg_I$is average inactive level and $Noise_I$ represents peak noise.

The electrode width has an inversely proportional relation with the singal-to-noise ratio (SNR) as the combined spherical and vertical diffusion field of electrodes helps to increase SNR with the decrease in electrode width[67]. On the contrary, the number of electrodes doesn't have any considerable influence on SNR because background noise is related to the surface area of the electrodes alone, and the signal value is proportional to the surface area of the entire array. Therefore, background noise will increase along with the signal value as the number of fingers increases[67].

3. OBJECTIVES

The primary objective of the thesis was to find out commercially available liquid-level sensors that can measure changes in liquid level for organ-on-chip applications and measure liquid levels in 3D vascularised chips. However, the initial survey did not provide suitable commercial sensors. Thus, the thesis aims to develop a liquid-level sensor based on the capacitive principle. A detailed study of sensor design and fabrication methods was carried out to meet the final objective. The objective of the thesis is then broadened into making sensor design and selecting fabrication methods and materials, followed by fabrication, testing, and analyzing the results of the sensor.

4. RESEARCH MATERIALS AND METHODOLOGY

In this chapter, the methods used in the thesis are explained. In Section 4.1, the geometry of the sensor is discussed. Sensor design and Fabrication of the sensors is presented in Sections 4.2 and 4.3, respectively. In Sections 4.4 and 4.5, sensor coating and thickness measurement of the coating layer is analyzed. Contact angle measurement used for investigating the fabrication quality and experimental setup and system are explained in Sections 4.6 and 4.7, respectively.

4.1 Geometry of Sensor:

The sensor was designed based on the theory of capacitors. Initially, there were three designs of sensors, and the pattern of the sensors was two parallel electrodes: Type A, an interdigital 1-1-1(1-n-1) pattern vertical finger electrode which is Type B and a horizontal finger electrode which is Type C Figure 13. Based on the theory, different versions and parameters were chosen when the sensor was designed. Initially, three versions of Type A were designed with different distances between the electrodes, such as 0.12 mm, 0.32 mm and 0.52 mm and Type B was designed in a 1-1-1 pattern where the number of vertical electrodes varies with the same distance between each finger electrode and Type C were designed based on the number of horizontal electrodes and the distance or gap between each horizontal electrode. A schematic representation of a different type of sensors are shown in Figure 13.

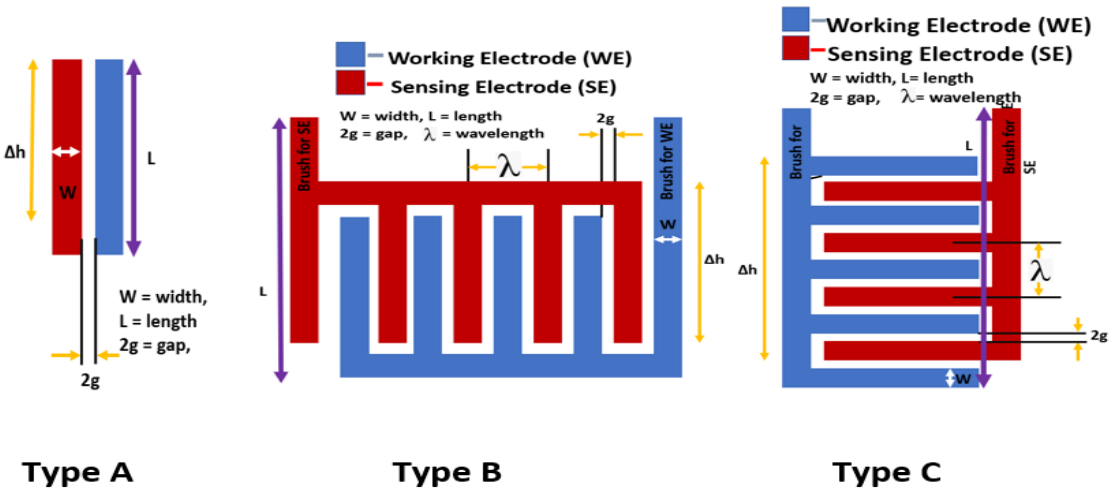

Figure 13: Sensor schematic diagram for different types.

4.2 Sensor Design:

Capacitive sensors were designed based on the theory and sensor geometry and considering the experimental plan in this work. There are multiple types of design of sensors, Type A, Type B and Type C. In Type A, there are different Versions of designs 1,2,3,4 depending on the gap between the electrodes and the dimension of the sensors and in Type B, the Versions are 1,2,3,4, where the design was made based on the number of electrodes and the dimension of the sensors. The design was made for Type C based on an interdigital comb electrodes sensor pattern. The distance between each electrode or comb was kept the same to design the layout of the interdigital capacitive sensor, which is Type B and Type C. The pattern of the sensor is 1-n-1. So, the sensor pattern was made 1-1-1 where the number of working and sensing electrode fingers were the same. The design of the sensor layout was done by AutoCAD 3D designing and modeling software. Figure 14 shows the sensor layout design in AutoCAD.

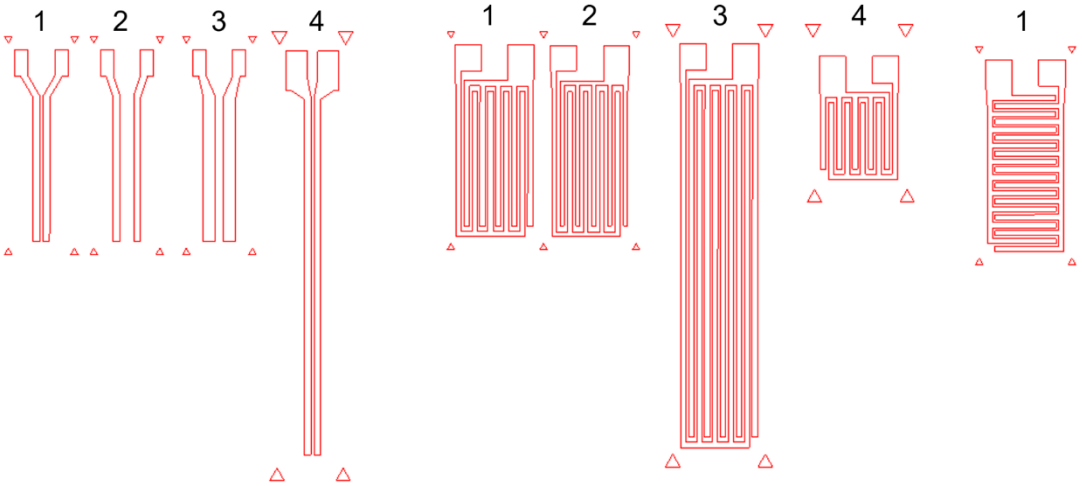

Figure 14: Sensor layout design by AutoCAD.

Table 4: Sensor details information

Name	Version	Image	Gap between electrodes (mm)	Length (mm)	width (mm)	pattern
Type A	1	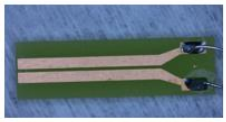	0.12	15.30	6.75	Parallel
	2	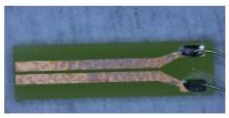	0.24	15.30	6.75	Parallel
	3		0.52	15.30	6.75	Parallel
	4		1.04	31.00	6.75	Parallel
Type B	1	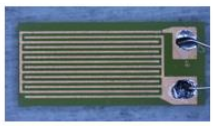	0.20	15.30	6.75	IDT
	2	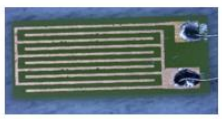	0.20	15.30	6.75	IDT
	3		0.20	31	6.75	IDT
	4		0.20	5	5	IDT

Type C	1		0.20	15.30	6.75	Comb

4.3 Sensor Fabrication

In the sensor fabrication process, the material that was used in PCB-FR4, copper wire to solder the sensor and make the insulation layer parylene C and SU-8 were used.

The first step of the fabrication process was to print the sensor layout mask and for theta, the film that was made for the design was printed with "AcccuRIP™ Ruby" software with an "EPSON T3200" printer. After the film mask was printed, it was left to dry the ink for around 30 minutes approximately so that wet ink did not spread throughout the mask. Then the mask was set to a PCB (Printing circuit board) FR4 board.

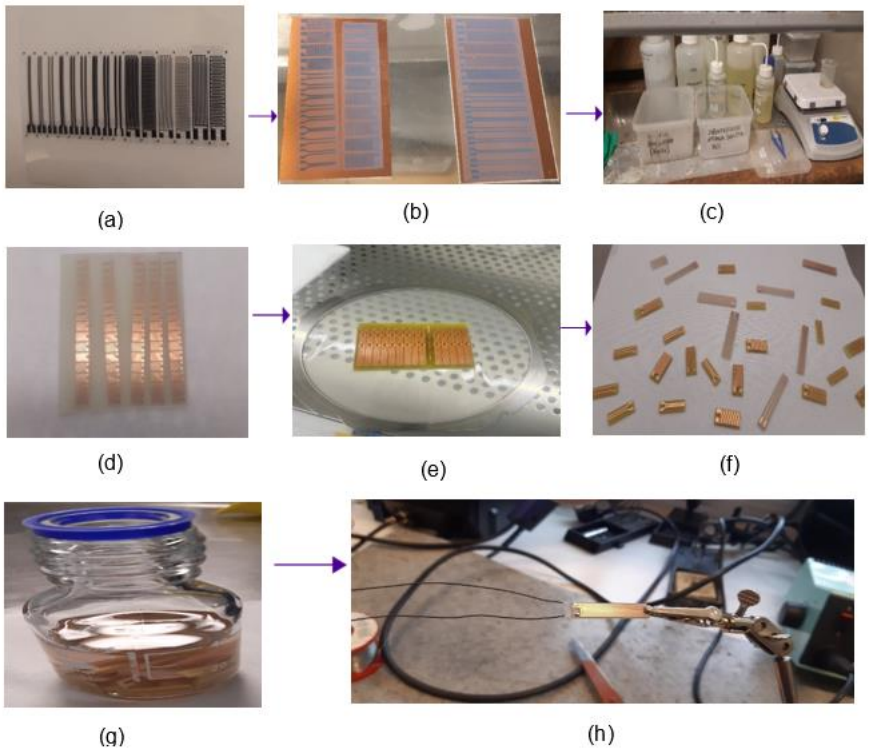

Figure 15: Fabrication process of interdigital fringe sensor, (a) Sensor printed mask, (b) Sensor mask placed on top of PCB for development, (c) Solution for developing the film, (d) Developed sensor (e) Sensor prepared for laser cutting (f) Sensor's in different shapes (g) Placed in a bottle for cleaning with Isopropanol (h) Sensors are soldered.

And PCB board was then cut into the size of the mask film with a manual saw device. Then PCB board was placed in a vacuum film sealer Aktina S (Walter Lemmen GmbH, Germany), and while sealing the film, safety and cautious steps were maintained as UV light was exposed during the process. After turning on the vacuum pump of the sealer and once the film was clamped, UV light was exposed for 90 seconds to make the deposition. Once the film was done, then the protocol for developing the film was performed. The PCB FR4 board is then put in the developer. The developer solution of NaOH was a pre-made solution where 30 ml NaOH and 70 ml water were used to make the solution for use, and the PCB board emerged in the solution; then the developer container was shaken well for around 40 to 60 seconds to make sure that the sensor film was appropriately developed and visible and once the development of the sensor layout finished, the PCB board was cleaned very carefully with cold water, and then the PCB board was put into the etching solution. The etching solution was made of 100 ml cold water, +30 ml HCL + 30 ml H_2O_2 and the PCB was poured into the etching solution, mixed it well for around 60 s to 70 seconds, and checked if the etching was done correctly or not. After the etching was finished, the PCB board was washed and cleaned with cold water on both sides of the PCB and then let the PCB board dry for 5- 10 minutes. After the etching was done, then the PCB board was set for the dicing of the sensor, and the dicing of the sensor was done in the cleanroom environment.

In the cleanroom, the PCB board was placed in a round shape of the frame attached with a thin layer of film. Then the PCB board was placed in the dicing device DAD 3221 dicing saw (DISCO Corporation, Japan) and cut the PCB board as sensor pieces. Then the sensor is cleaned & washed and then vacuumed. After the clean room works, the sensor is in ready shape. All the sensors were then put into a container dissolved in acetone and dipped for around 30 minutes to clean and after the cleaning, all the sensors were soldered in the electronics lab. During the soldering, single-phase copper wire with a diameter of 0.01 mm was used. The size of the sensor and the durability and adjustment for the experimental setup was considered while choosing the copper wire. The approximate length of the wire of sensors was 6-10 cm. After the sensors are soldered, they are checked and tested whether the sensors are still working. If there was any short circuit or cack or if the sensors were damaged in any other way during the fabrication process.

4.4 Sensor Coating:

When the sensor fabrication is done, the electrode layers are fully conducting to a medium like water or salt. So, the sensor layer should be coated to provide the insulation layer. In this Section, the details of the sensor coating will be discussed.

4.3.1 Sensor Coated with Parylene C:

Parylene C coating was done on top of PCB electrodes or the fabricated sensor by following the above steps with Parylene coated device named “LAB TOP PARYLENE DEPOSITION SYSTEM” manufactured by “PARA TECH”, from the UK. The coating was done every time with a different number of sensors, and the sensors' thickness varied. So, considering the thickness layer on the sensor surface, different amounts of parylene dimer were used. While coating the sensor, two ways were followed to make the coating sensors put into a plastic chamber or cup shown in Figure 16 and kept in the

metal frame outside the chamber. Parylene spreads uniformly over the substrate. The chamber or the plastic cups were used to make the coating more accurate.

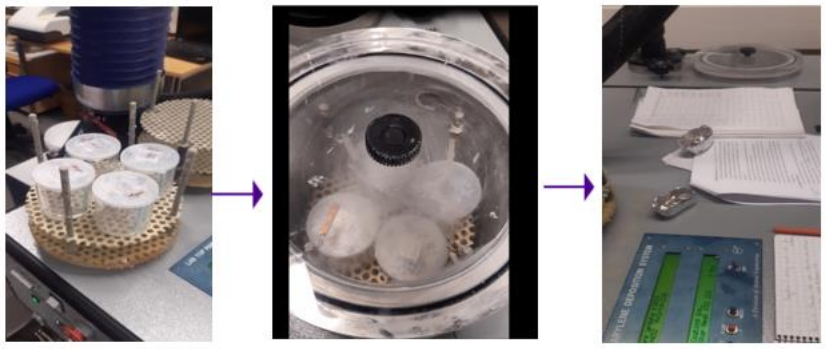

Figure 16: Parylene coating (a) Sensor are placed in chambers, (b) Sensors placed inside Parylene coater, (c) Parylene process started.

The parylene coater device was cleaned before using it. The vacuum valve was kept open, and the air valve was kept closed at the beginning. The glass tube is inserted into the heating tube with big tweezers considering that the glass tube reaches close to the edge of the O-ring orifice. Once the cooling element reached a temperature below -5°C, the hatch of the main deposition chamber was closed. Then the air valve was fully opened, the vacuum valve was fully closed, and the device controller was turned on

when the parameters showed in display 9999 mics. The parylene coater device was fully ready to operate.

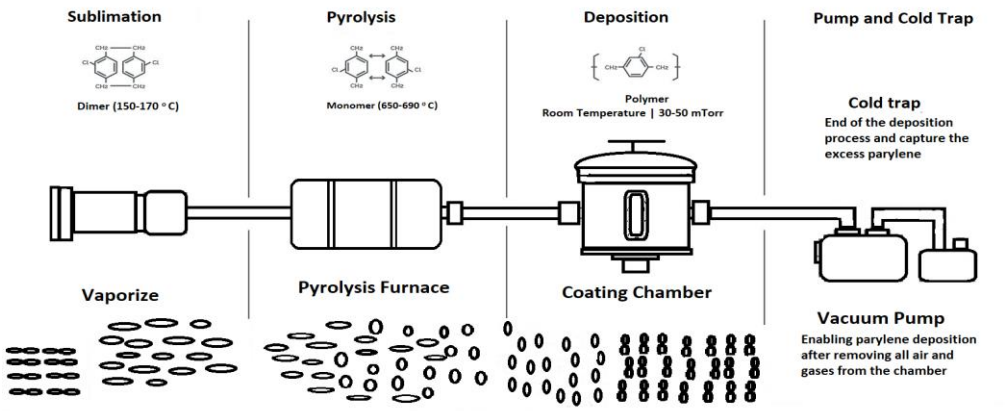

Figure 17: Process diagram of parylene coating, image is taken and modified from VSI web portal *[80]*.

When the device was ready for making the parylene deposition, the dimer mass was fixed based on the number of sensors and the expected thickness layer on top of the electrodes. In the initial batches, the dimer mass was around 5 gm, and there were 20 sensors. An aluminum foil pot was made where the dimer mass was placed, and then the soil pot was inserted inside the heating channel, keeping a distance of about 1 cm from the edge of the glass tube and the hatch of the heating channel is closed. After the device was set, the sensors were placed to the metal device's sample holder and put it inside the chamber of the devices. At the same time, the sensors were placed in the metal sample holders.

Table 5: Parylene coating recipe for 7 µm thickness insulation layer

Step	1	2	3	4	5	6	7	8	9	10	11	12
Time ramp	1	1	30	30	1	1	1	1	1	1	1	1
Temperature	120	120	145	171	170	171	170	171	170	171	170	171
Time soak	1	10	30	5	1	1	1	1	1	1	1	20

Door TD	Vac 1	Vac End	Pyrolysis	Postpy	Prepy	Gage	Champ
20	10	0	650	220	220	122	123

Then considering the thickness expected for the insulation layer, the recipe was manually set in the device controller. The recipe was made mainly to get desired thickness. One recipe (see Appendix A for other recipes) is explained in Table 5, where the steps were described. In Table 5, there is a time ramp that changed when the temperature started to change, the initial temperature of the coating process is 120°C which is preheated for the process, and the initial vaporization of the dimer happened to be started at 145°C shown in Table 5 where the time ramp is 20 minutes and then for that the time ramp is 5 minutes. Once the temperature reaches 170°C, the ramp is stabilized for 1 minute until the process ends following the further steps. When the temperature stabilized near 170°C the parylene dimer started to spread on the substrate material uniformly and for that, the time soak, which takes 28 minutes, followed by the steps shown in Table 5. was set because of the difference of layer thickness on top of the surface layer of the PCB. In the pyrolysis step, the temperature is 650°C which is before the deposition of the dimer is done and then in post and pre pyrolysis, the room temperature is maintained and the process for parylene coating takes around 2-3 hours, depending on the thickness, including the cooling down of the device.

4.3.2 Sensor Coated with SU-8:

The *s*ensor surface was spin-coated by a SU-8 5 photoresist. Spin coating was done in a clean room with the spin coater, model ws-650H2B-23NPPBO, manufactured by Laurell Technologies, USA. The hot plat was preheated at 65°C and then the spin coater was cleaned with acetone and covered it with aluminum foil and the 100 mm chuck was set into the spin coater.

Figure 18: SU-8 coating in the clean room.

Then the sensor was placed into the center of the chuck and the valve was turned on. Before the spin coating process, pressure and vacuum was turned on. After the sensors were placed, then SU-8 substrate was put on the surface of the sensor and the spin coater was turned on; where the rotational speed for the spin coater were 3000 rpm and the acceleration was set 250 and the duration of the spin coating process was 60 seconds so that the SU-8 spread throughout the sensor surface. Once the costing was finished, the spin coater was turned off and the vacuum was turned off also to take out the sensor and then using a tweezer, the sensor is then placed to a hot plate which was preheated at 65°C and then sensors were kept for 2 minutes on the hot plate and later the sensors were placed to another hot plate where the temperature was 95°C and sensors were kept for 10 minutes. After that, the sensors were placed in a petri dish and put into the mask aligner for exposure. The exposure time was around 2 minutes. After that, the petri dish was placed to a UV oven for hard baking was done at 150°C for 15 minutes and to cool it down, it was kept overnight.

4.5 Thickness Measurement of Coating Layer:

When the sensor coating was done, then in the cleanroom, the thickness measurement of the coating layer on top of the surface was measured with a Bruker Dektak stylus profilometer manufactured by Bruker, USA. While coating, there was a glass plate and PCB board kept on the metal plates so that the glass plate surface was also coated as

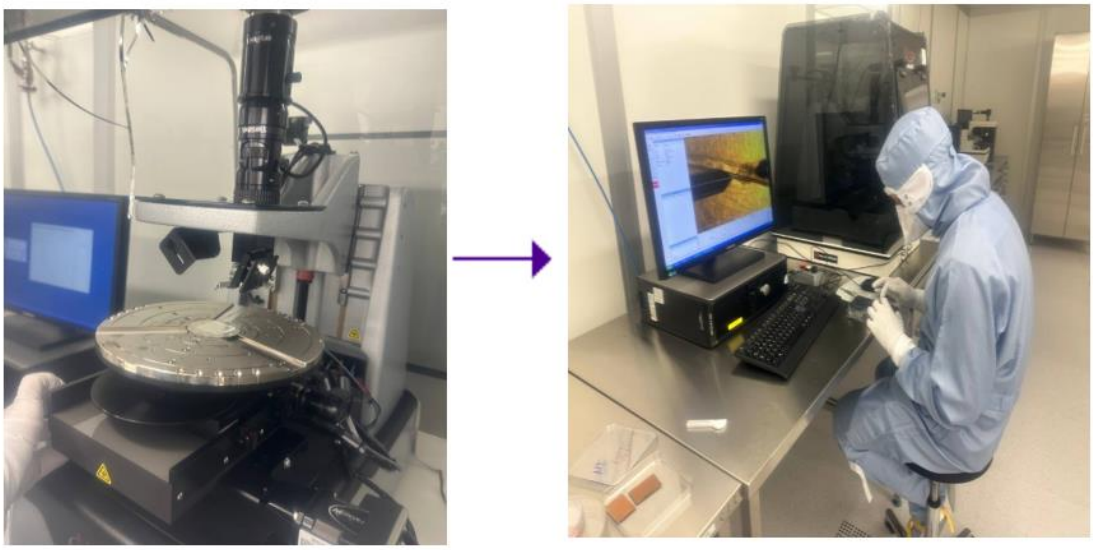

Figure 19: Sensor thickness measurement

Uniformly as the sensor's surface. For measuring the thickness of the sensor insulation layer the surface of the glass plate was scratched and was placed and then using the optical profilometry device, the thickness of the sensors was measured. The measurement was taken in different places on the surface and then the average of the measurement was considered.

4.6 Contact Angle Measurement:

The contact angle of the sensor was measured every time after the coating of the sensor was done. The parylene C coating should be hydrophobic if the contact angle is greater than 90°, the range for hydrophobicity is and 90°-150° and the SU-8 coating should be hydrophilic if the contact angle is less than 90° and then the range for hydrophilicity 50°-90°. The contact angle was measured with the contact angle measurement device named "Attention Theta Lite manufactured by Biolin Scientific, Sweden. The contact angle was measured with droplets of 5 µL to 7 µL on the surface of the glass plate.

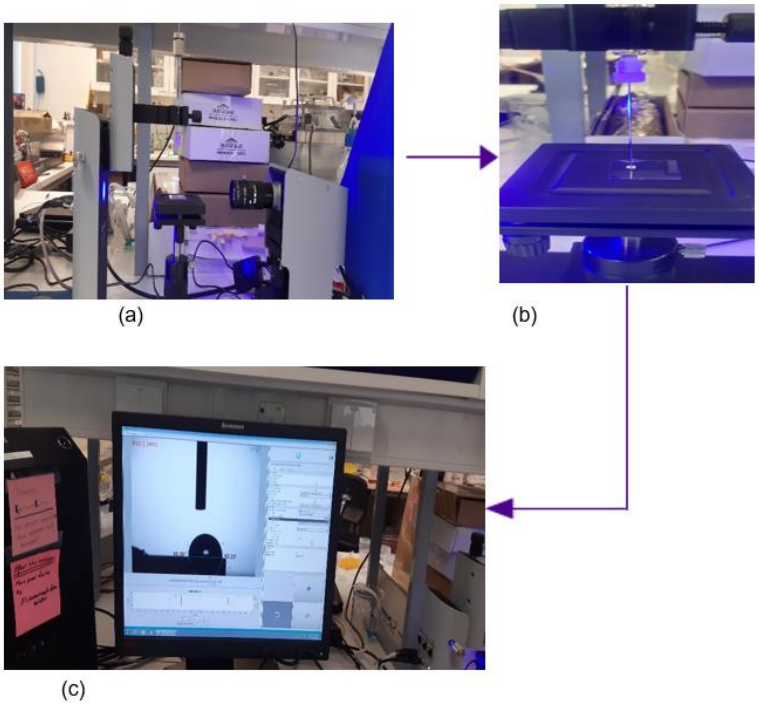

Figure 20: Measuring the contact angle, (a) Represents the contact angle device, (b) The droplet placed on glass plates coated with parylene, (c) Contact angle measurement value.

The contact angle was measured for all the sensors. Basically, each and every time the sensors were coated, a glass plate or a PCB board was placed in the metal frame where the sensors were placed during the coating so that the glass plate and PCB board were also uniformly coated. After that, the coating layer on top of the glass plate and PCB were used to measure the contact angle. Then while measuring the contact angle, the

glass plates were placed where the droplet of liquid was put to measure the contact angle.

4.7 Experimental Setup and System:

The details of the experiment setup and equipment that are used to perform the experiment are noted in this section. Figure 21 shows the experiment environment and the necessary equipment. During the experiment, a laptop was connected with a serial port to a Precision LCR meter ST2827A, manufactured by Sourcetronic, Germany, and with another serial port to a secondary dual syringe pump, model S41-371-1003 manufactured by World Precision Instruments, USA. The LCR meter was connected through a wire to the end of the sensor that was soldered with copper wire to get the measurement data.

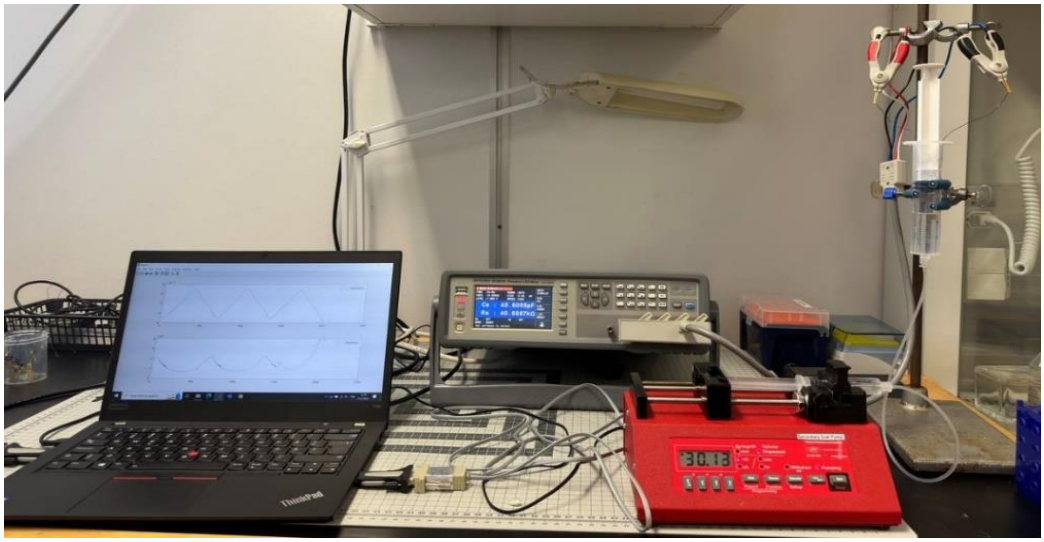

Figure 21: Experiment setup and equipment

In the experiment, syringes 2 ml, 10 ml and 50 ml soft ject luer locks were manufactured by HENKE SASS WOLF, Germany, used for both pumping the liquid and storage for the liquid where the sensor was placed to measure the change of liquid level. The liquid was filled in a syringe and that was connected to that syringe pump and the pump was pre-set with MATLAB coding so that it could pump a specific flow of liquid to the other syringe that was connected with a tube Figure 21 and the volume of the liquid was also pre-set by MATLAB code considering the height of the sensor and also the diameter of the syringe. In some of the experiments, the pump was operated manually to check for any differences between manual pumping and automatic pumping through code. As it was mentioned above that for different experiments, a pump syringe was selected according to the syringe which was used as a liquid reservoir.

During the experiment, the sensor was placed inside the syringe; it was partially dipped in the liquid so there were initially some capacitance values. The initial portion of the sensor was dipped, considering the effectiveness of the sensor. Before starting the experiment, the sensor was fully dipped automatically a couple of times by increasing and decreasing the liquid back and forth, so the sensor surface is fully wet. Once the liquid started to increase, the change of the capacitance is observed in the live manuscript of MATLAB and the same for decreasing the liquid level. The sensor's wired place was connected to an LCR meter which was connected to a laptop with a serial port and thus, the live images of the changes of capacitance with respect to changes in liquid level were identified. For each of the experiments, the liquid level was increased for a certain volume, and it was also decreased with the same amount of volume as well as same flow rate. For all the experiments, the increase and decrease cycle was repeated at least 5 times or at maximum ten times. After each cycle, when the liquid reached the maximum point while increasing and came back to the initial point after decreasing, there was 30 seconds of pausing time for the pump to get the stabilized position for the liquid level. While the experiment was done, all the connections were checked properly, and the if there was any bubble inside the syringe, that was also taken care of before performing the experiment. For all the experiments done, the liquid that was used is DPBS (Dulbecco's Phosphate-Buffered Saline). All the experimental data were taken and analyzed with MATLAB programming.

When all the sensors' performances were tested and the data were analyzed after that, there was an experiment with a customized sensor Type B Version 4 (Table 4) for 3D vascularization chip to check if the sensor can measure or monitor the changes of liquid in the chip.

5. RESULTS AND DISCUSSION

In this Section, results are shown and discussed. In Section 5.1 and Section 5.2, results related to contact angle and thickness measurements are described. In Section 5.3, data of the Type B Version 3 sensor is compared and analyzed along with other sensor types. Organ-on-Chip testing and challenges and future work are described respectively in Section 5.4 and Section 5.5.

5.1 Contact Angle:

Parylene C: Sensors coated with parylene C were then used to measure the contact angle. The contact angle was measured for both surfaces of the sensor. Firstly, the surface of the sensor where the electrode developed was measured 3 times in 3 different places of the surface and then in the smooth surface of the sensor, contact angles were also measured 3 times in 3 different positions. There were in total of 24 measurements as the sensors were placed in four different chambers (as shown in Figure 16 (a)) and each of them was measured to get the contact angle from both surfaces. The minimum contact angle for the sensor was 86.93 degrees in the sensor surface, while it was 87.20 degrees for the smooth surface. The maximum contact angle for the sensor was 102.00 degrees in the sensor surface while it was 97.07 degrees for the smooth surface. The average contact angle from the sensor surface was 91.19 degrees and from the smooth surface, the average contact angle was 91.92 degrees. The standard deviation of contact angle from the sensor surface and smooth surface are 4.07 degrees and 3.08 degrees, respectively. From the value of the contact angle, it indicates that the sensor surface is hydrophobic, and the surface coated with Parylene C is supposed to be hydrophobic as based on theory. The aim was to make the surface as hydrophobic as possible since the hydrophobic surface repels moisture and water and protects the surface from wetting. So parylene C had a better coating then SU-8 5 as it showed hydrophobicity.

SU-8 5: Sensor coated with SU-8 5 were measured to get the contact angle. Contact angles were measured from both surfaces. Each time 3 measurements were taken from different portions of the surface and then the average of the contact angle was measured. The minimum contact angle for the sensor was 64.61 degrees in the sensor surface, while it was 56.33 degrees for the smooth surface. The maximum contact angle for the sensor was 80.49 degrees in the sensor surface, while it was 81.02 degrees for the smooth surface. The average contact angle from the sensor surface was 73.89 degrees and from the smooth surface, the average contact angle was 69.63 degrees. The standard deviation of contact angle from the sensor surface and smooth surface are 5.85 degrees and 9.72 degrees, respectively. From the value of the contact angle, it indicates

that the sensor surface is hydrophilic, and surface coated with SU-8 5 is did not show good performance due to the surface being hydrophilic. So, the experiment with SU-8 5 was not further carried out.

5.2 Thickness Measurement:

The average thickness of the insulation layer of the initial batch sensor was 7.5 µm. The thickness was measured from 5 different glass plates which were placed in the parylene coater device on a metal frame shown in Figure 16 (a). From each glass plate, the thickness was measured four times from both surfaces of the plates, so in total 8 measurements for each plate. The minimum and maximum thickness was respectively 7.3 µm and 7.8 µm, and the standard deviation was 0.17 µm from the first batch of the sensor. During the experiment, there were errors in sensor performance like leakage of current and the sensors were not repeatable for more experiments, so a new batch of sensors was manufactured to have a thicker layer of thickness. A thicker insulation layer improves the electrical isolation between the IDT electrodes and the liquid being monitored, resulting in decreased electrical interference, reduced risk of short circuits or signal distortion, and more accurate and reliable readings. So, the plan was to make a thicker insulation layer to see if the layer could protect the sensor from leakage current and prevent the surface from getting rid of moisture. In the next batch of the sensor, the average thickness of the insulation layer with parylene C was 11.2 µm, with minimum and maximum thicknesses were 10.9 µm and 11.6 µm, and the standard deviation was 0.25 µm. The higher insulation thickness provided more protection than a lower thickness of insulation layers for the IDT electrodes, enhanced the durability of the sensor and reduced its vulnerability to harm caused by external factors such as moisture, contaminants, or physical strain. This led to a longer lifespan and improved performance over time.

However, the higher thickness had negative impacts also for the sensor’s performance, such as inaccuracies. Additionally, a thicker insulation layer lowers the likelihood of leakage current flowing between the IDT electrodes and the liquid, which can negatively affect the sensor's performance and introduce inaccuracies in capacitance measurements. The presence of a thicker insulation layer increased the distance between the IDT electrodes and the liquid, thereby reducing the capacitance value and the sensitivity also decreased due to higher thickness.

In the final batch of sensor, considering the effect of thickness and comparing the performance the insulation layer thickness was again made lower and this time, the average thickness was 7.65 µm and the minimum and maximum values of thickness

were 5.5 µm and 7.8 µm respectively with a standard deviation of 0.12 µm. During the experiment with this thickness, the performance was good though there were still some sensors showing short circuit phenomena.

On the other hand, SU-8 5 coated sensors thickness was measured, and the range of insulation layer thickness was 3.5- 6 µm where the minimum thickness was 3.5 µm and the maximum thickness was µm 6 µm and the average thickness was 5.12 µm with a standard deviation of 1.08 µm. The aim was to have a thickness of 5 µm; however, the insulation layers were not the same everywhere of the sensor surface and during the experiment, all the sensors that were coated with SU-8 5 did not show the expected performance. So, no further experiment was carried forward with SU-8 5.

5.3 Characterization of Sensors:

From all the sensors, experimental data were analyzed and compared the maximum and minimum capacitance of each sensor and then the sensitivity and signal-to-noise ratio (SNR) is also demonstrated. From all types and different versions of the sensor, only Type B Version 3 sensor's performance is graphically represented and explained. In Appendix B, other types of sensors along with their version's performance, are graphically shown.

5.3.1 Finding Maximum and Minimum Capacitance of Sensor:

The maximum value of the sensor was calculated from the mean value of peak points of 10 cycles of increased liquid. The value was also calculated theoretically and then compared. From Figure 22, the Y-axis shows the capacitance level, and the X-axis shows the time duration. So, the graph illustrates the change in liquid level with respect to time. From the graph, the maximum peak points are presented as data1 and from the maximum points of 10 cycles, the average was taken, and the mean of the capacitance was found using MATLAB script (Appendix C for details on how data were analyzed)

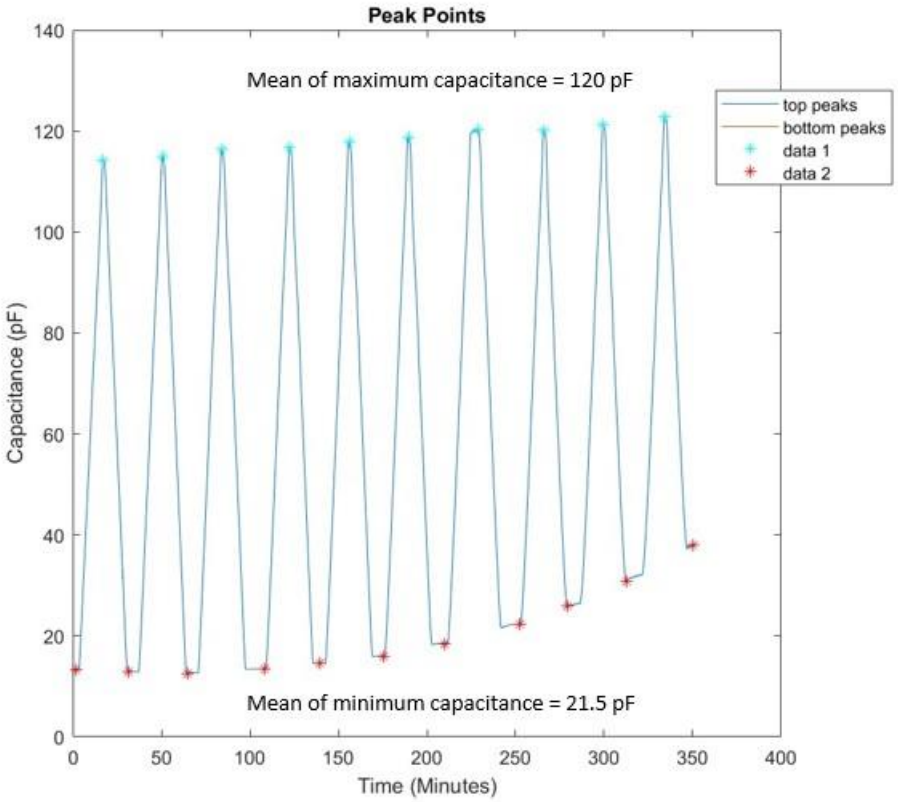

Figure 22: Maximum and minimum capacitance of sensor Type B Version 3.

and the value of Type B Version 3 maximum capacitance is 120 pF and similarly, when the liquid level was decreasing, the mean of minimum capacitance value was also calculated and using MATLAB script (Appendix C for details) and data 2 in Figure 22 represents the minimum peak points of capacitance. The experimental minimum capacitance value of the Type B Version 3 sensor is 21.5 pF. From the experimental value, the capacitance range is around 100 pF. Similarly, the minimum and maximum value for each Type, including all the versions, was calculated and presented in Table 6.

On the other hand, the maximum and minimum capacitance value was calculated theoretically by using equation (4) and equation (6). The maximum value of capacitance is 130 pF, and the minimum value of capacitance is 21.8 pF, which gives a range of approximately 108.2 pF.

From Figure 22, it is clearly visible that there is drift due to the repetition of a liquid level rising and decreasing over the changes of cycles. The minimum and maximum values started to change over time. As it was mentioned during the experiment, meniscus formation was seen around the sensor, especially at the bottom portion of the syringe that was used as a reservoir. This meniscus might have affected the changes of capacitance value both for rising and decreasing signals. The area of the syringe was so

narrow that there was not enough gap between the sensor surface and the syringe wall. When analyzing the data considering the drift, the mean of minimum and maximum capacitance values was taken to get the standard value.

In Figure 23, the box plot represents the comparison of the maximum capacitance of Type A and Type B, including different versions of the capacitive sensor. The box plot shows the difference in the experimental maximum capacitance values of the sensors.

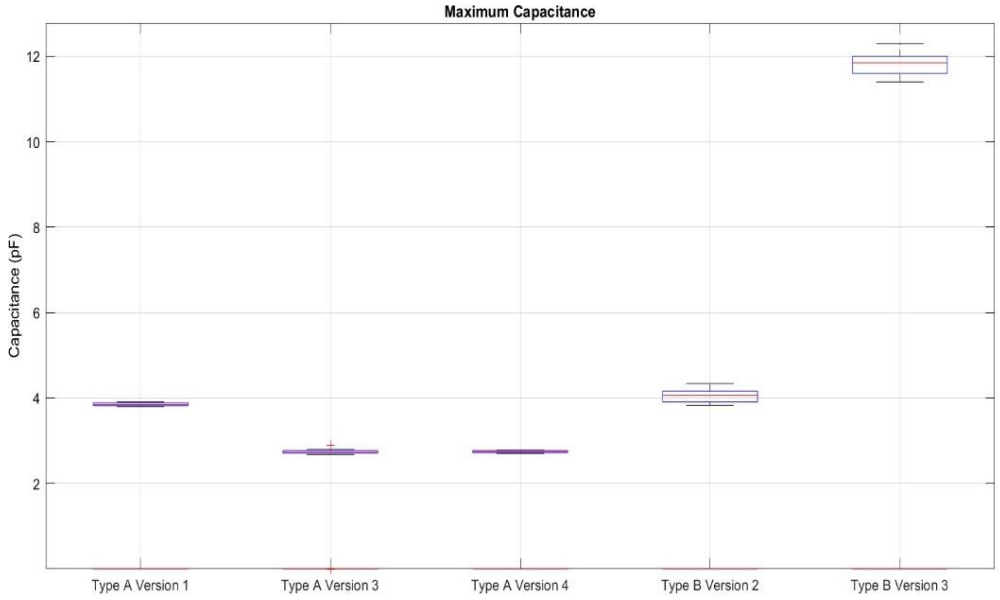

Figure 23: Comparison of maximum capacitance (Experimental value) of Type A and Type B sensor

It is noticeable that Type B Version 2 and Version 3 have better capacitance than Type A Version 1, Version 2, and Version 3. The box plot shows that Type B has a more capacitance range than Type A. For all types and different versions of sensor maximum and minimum capacitance, both theoretical and experimental values are compared in Table 6.

Theoretical minimum and maximum values of all types of sensors, along with their versions, are calculated using equations (2), (4) and (6). For Type A, the equation was used (2) and for both Type B and Type C, equations (4) and (6) were used and equation (6) varies as the version changes depending on the number of electrodes. The theoretical minimum value was calculated when the sensor was placed in the water and the maximum height of the sensor was in the air and the maximum was calculated when the sensor was almost fully dipped in the water except for some portions of the sensor's height were in the air.

Table 6: Comparison of theoretical and experimental capacitance of different sensors

Name	Version	Minimum Capacitance (pF) Theoretical Value	Minimum Capacitance (pF) Experimental Value	Maximum Capacitance (pF) Theoretical Value	Maximum Capacitance (pF) Experimental Value
Type A	1	2.89	2.12	228	38.6
	2	14.5	1.39	52.6	10.5
	3	17.8	1.13	26.3	10.5
	4	6.31	4.05	89.7	27.1
Type B	1	18.9	5.39	67.4	63.7
	2	19.5	3.14	40.6	40.5
	3	21.8	21.5	130	120
Type C	1	28.3	4.83	87.9	27.6

From Table 6, there are some noticeable differences is observed. For example, in Type A Version 1 sensor shows a minimum capacitance value in the experiment was 2.12 pF and in theory, it should be 2.89 pF, but the maximum value was much lower in the experiment than the theoretical value, which is 38.6 pF and 228 pF respectively. A similar difference has been observed for Type A Version 4 and Type C Version 1. However, there are some minor differences in theoretical and experimental capacitance values for all the sensors. This difference could be due to the fabrication of the sensor, and sensor material properties might have affected the results. In an ideal case, the theoretical value and the experimental value would match each other. However, there are always factors or errors in the experiment that make the experimental value different from the theoretical value.

5.3.2 Slope and Sensitivity of Sensor:

The change in Capacitance while increasing and decreasing the level of liquid is demonstrated and the slope of both the rising and decreasing period of liquid is illustrated for the Type B Version 3 sensor in Figure 24.

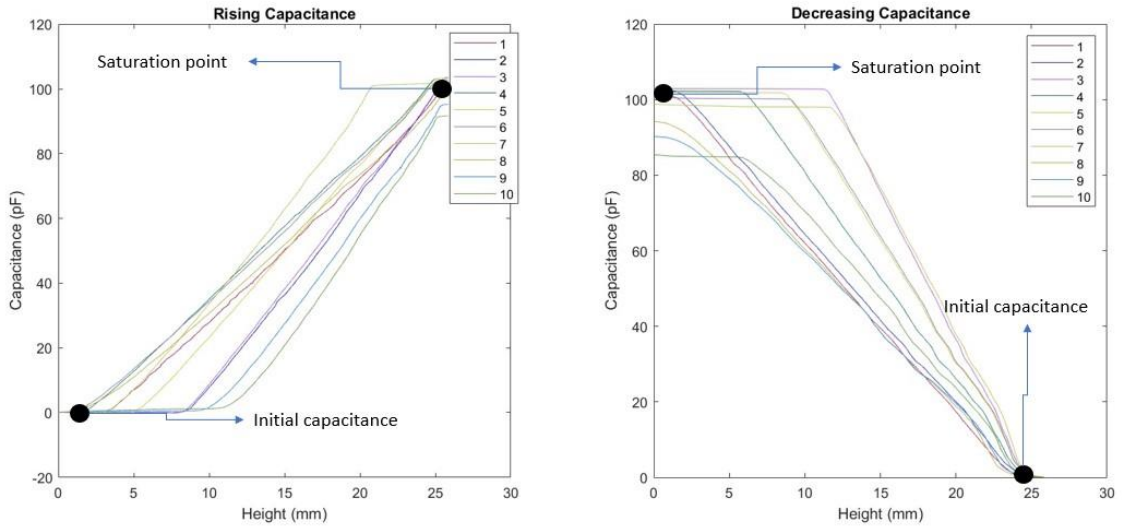

Figure 24: (a) Slope of increasing capacitance (b) Slope of decreasing capacitance

Figure 24(a) shows the slope of the rising period of liquid and Figure 24 (b) shows the decreasing cycle of liquid in where in X axis, the changes of level in height in mm and changes of capacitance in F and from the slope the sensitivity of the sensor is calculated. While analyzing the data, time was converted into height. Height was divided by the data point in the time axis for the rising part of the signal, as these time stamps (data points) represent the active sensor's height. Similarly, the height data points for decreasing part of the signal were calculated considering the required time data points. So, the conversion did not cause any complications in the results.

In Figure 24, both the increasing (a) and decreasing (b) of the graph of Type B Version 3 sensors represents the slope for each cycle which is in different color and presented from 1-10. From the graph, it is noticeable that there is a change in the graph for each cycle which over time. The sensor performance changed as both the increase and decrease graph shows variations during the whole 10 cycles. The factor that affected the change in sensitivity over time could be the surface tension properties of the sensor. Another reason could be the coating of the surface that started to oxidize due to moisture, which might have had an impact also over the period of the experiment in the sensor's performance. The average value from 10 cycles is calculated for both increasing and decreasing liquid levels and the standard deviation is also calculated and presented in Table 7

To get a better graphical representation of changes in capacitance with the changes in liquid level, only one cycle of liquid level increasing, and one cycle of liquid level decreasing is plotted in Figure 25. From the sensitivity, Type B Version 3 has comparatively better sensitivity than Type B Version 1 and Version 2 as well as from Type A and Type C. The average sensitivity for increasing and decreasing periods of liquid level is calculated using MATLAB and the code that was used is presented in the Appendix C.

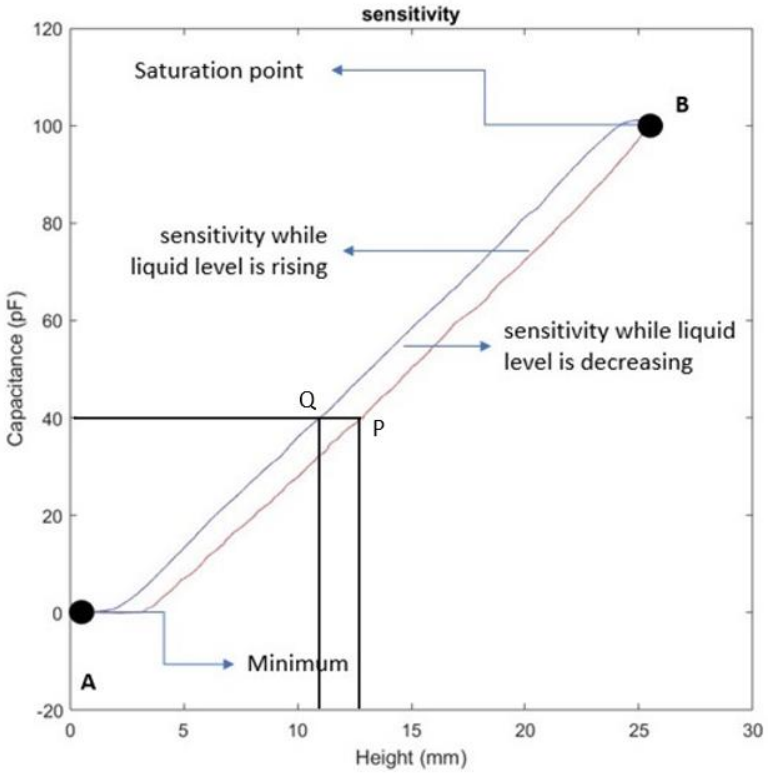

Figure 25: Sensitivity graph of Type B Version 3 sensor (Experimental value).

In the graph, the red line indicates the rising of the liquid level, and the blue line indicates the decrease of the liquid level. From the sensitivity graph, it is clearly noticeable that the change in slope while the increase happens at the liquid level and the change in a slope while the decrease happens at the liquid level are almost close to each other. In Figure 25, A is the minimum capacitance level, while B indicates the maximum saturation points. The response of increasing and decreasing slopes is almost linear. However, the rising and decreasing signal for changes of liquid level is not fully linear. This is known as hysteresis. In point P, while the liquid level rising and in point Q while the liquid level decreasing, both points represent 40 pF capacitance but they both have different heights for the same value which is approximately 13 mm and 11 mm, respectively. Due to the hysteresis, this might happen, and one of the reasons behind the hysteresis

phenomenon could be the gravitational force. When the liquid level is rising, it is moving against the gravitational force, which might make the change of level of liquid slower than when the liquid level was decreasing as in decreasing period; the gravitational force works in favor of the liquid movement. There might be other reasons, such as materials properties, environmental conditions or the measurement setup and system affecting the behavior. These factors could be solved by changing the materials' properties and making the setup more controllable. Though it had shown a hysteresis phenomenon, the sensor had reliable performance in sensitivity. The sensitivity value for both rising and decreasing signals is 3.92 pF/mm and 3.90 pF/mm.

Table 7: Comparison of the experimental value of different sensors

Name	Version	Sensitivity while liquid level rising (pF/mm)	Sensitivity while liquid level decreasing (pF/mm)	STD Sensitivity while liquid level rising (pF/mm)	STD Sensitivity while liquid level decreasing (pF/mm)
Type A	1	3.04	3.03	0.03	0.02
	2	2.17	2.18	0.01	0.01
	3	0.78	0.78	0.01	0.01
	4	0.89	0.89	0.01	0.01
Type B	1	3.81	3.82	0.13	0.14
	2	3.10	3.09	0.13	0.13
	3	3.92	3.90	0.16	0.23
Type C	1	1.87	1.86	0.10	0.09

In Figure 26 the graph shows the change of height in the X-axis and in the Y-axis, it represents the change in capacitance.

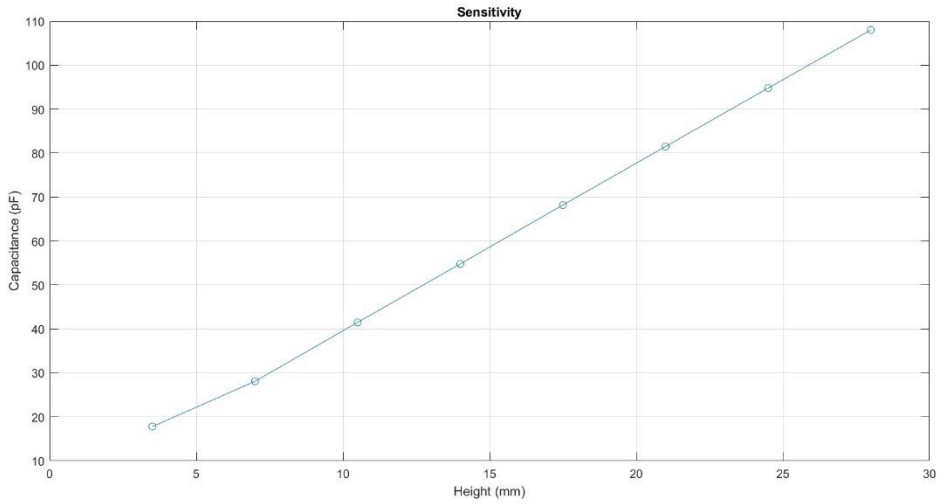

Figure 26: Sensitivity graph of Type B Version 3 sensor (Theoretical value)

The value of the capacitance is theoretically calculated using equations (4) and (6) from Section 2.4.7, and the value is shown in Table 9. From the graph, the average sensitivity is calculated and compared with the average sensitivity of the rising sensitivity of the experimental value. The average theoretical sensitivity of the Type B Version 3 sensor is 3.98 pF/mm, while the average sensitivity in experimental value is 3.92 pF/mm, which is quite close to the value in theory. However, in the experimental environment, there were some limitations, like the meniscus was visible, so the change of capacitance was not the same every time while increasing the liquid level and decreasing the liquid level. Another factor that might cause some errors in data is noise from electrical devices and from the environment. Furthermore, the syringe pump itself could cause issues like creating air bubbles in the syringe or reservoir during pumping liquid both for increasing and decreasing liquid which might affect the results. So, the sensitivity value shows that the sensor can measure the small amount of change in liquid level by observing the changes in capacitance.

Table 8: Theoretical capacitance value for Type B Version 3 sensor

Name	Type B Version 3							
Height (mm)	3.5	7	10.5	14	17.5	21	24.5	28
Capacitance (pF)	17.8	28.1	41.5	58.4	68.2	81.5	94.8	108

5.3.3 Measurement of Liquid Level in Pipetting Experiments:

The sensor performance was also checked manually by pipetting the liquid. This experiment was done considering the final application. In the final application, where there are multiple reservoirs in the vascularization chip where the reservoirs are filled manually one after another, and the change of liquid level is measured by measuring the change of capacitance and also the same for decreasing the liquid by emptying the reservoirs the capacitance changes were measured. So, the goal of this experiment was to check how it performed when the manual pipetting was done for both increasing and decreasing of liquid in the syringe and then data was analyzed.

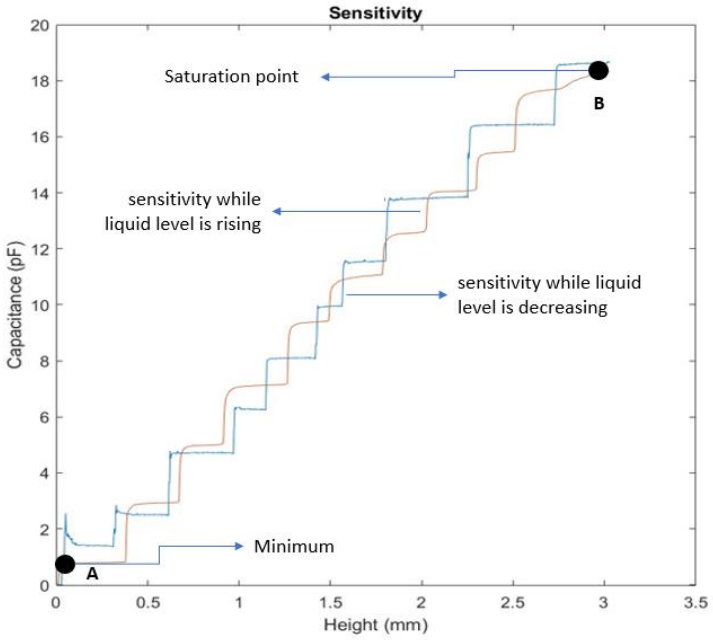

Figure 27: Sensitivity graph of Type B Version 3 sensor

Figure 27 represents the graphical presentation of liquid change. Each time the liquid was put inside the chamber, the level started to rise; the response in Figure 27, shown in blue, shows the increase and the response in Figure 27, shown in red, represents the decreasing value of capacitance in against of change of liquid level which is shown in X axis as the change of height. The changes are similar during increasing and decreasing periods of liquid level. The sensitivity value of rising and decreasing liquid levels as well as the maximum and minimum capacitance value of the Type B Version 3 sensor, is shown in Table 9.

Table 9: Different values of Type B Version 3 sensors (Pipetting).

Name	Version	Min Capacitance (pF)	Max Capacitance (pF)	Sensitivity while liquid level rising (average) (pF/mm)	Sensitivity while liquid level decreasing (average) (pF/mm)
Type B	3	18.20	39.50	7.10	7.05

5.3.4 Signal to Noise Ratio (SNR):

Signal to noise ratio is calculated from each signal and the noise generated to the actual signal. SNR is calculated for each type of sensor and the value shows that the noise compared to the actual signal is lower, which means the sensor has better accuracy and clear and effective performance. During the experiment, when the data signal was received, it was considered that there was white noise in the signal. To get the signal-to-noise ratio, the sampling frequency was computed. Then we used MATLAB's built-in function snr (signal, sampling frequency) to compute the Signal to Noise Ratio (SNR).

Table 10: Comparison of SNR of different sensor

Name	Version	SNR (dB)
Type A	1	27.60
	2	30.24
	3	35.95
	4	25.76
Type B	1	29.82
	2	35.64
	3	25.15
Type C	1	28.26

Comparing the value from Table 10, Type A Version 3 has the best signal-to-noise ratio, which is 35.95 dB. So, it can be said that Type A Version 3 has a strong desired signal than the background noise, which means the sensor has higher accuracy. On the other hand, Type B Version 3 has the lowest signal-to-noise ratio, 25.15 dB. However, the SNR can be improved by changing the environmental factors and by changing the substrate material of the SNR of each sensor and repeatability.

After analyzing all the data from each type, including their versions, it can be said that Type B Version 3 has better sensitivity, better repeatability, and better range of capacitance value than Type B Version 1 and Version 2 and also from Type A and Type B, including all versions. Type B Version 3 has shown that it is more reliable than other types and versions. However, Type B Version 3 had the lowest signal-to-noise ratio of any other Type and Version of the sensor.

5.4 Organ-on-Chip Testing:

For vascularization chips, a sensor is designed and customized considering the chip dimension. The Type B Version 4 is an IDT sensor that is fabricated with different dimensions (as presented in Table 4). However, the characteristics and properties of this sensor are similar to Type B Version 3. This was made for the final application considering the vascularization chip. The sensor was placed in one of the Reservoirs of the chip, as shown in Figure 28(b). The experiment was performed to see how the sensor behaved.

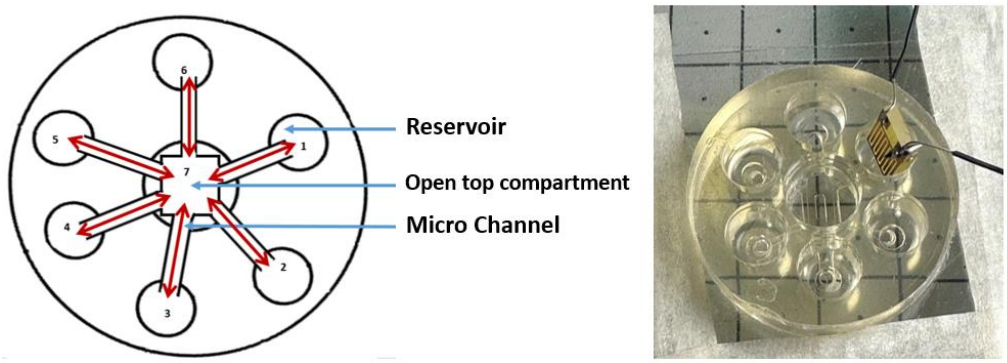

Figure 28: Vascularisation chip, (a) Schematic diagram of the vascularisation chip, (b) Sensor placed in 3D vascularisation chip.

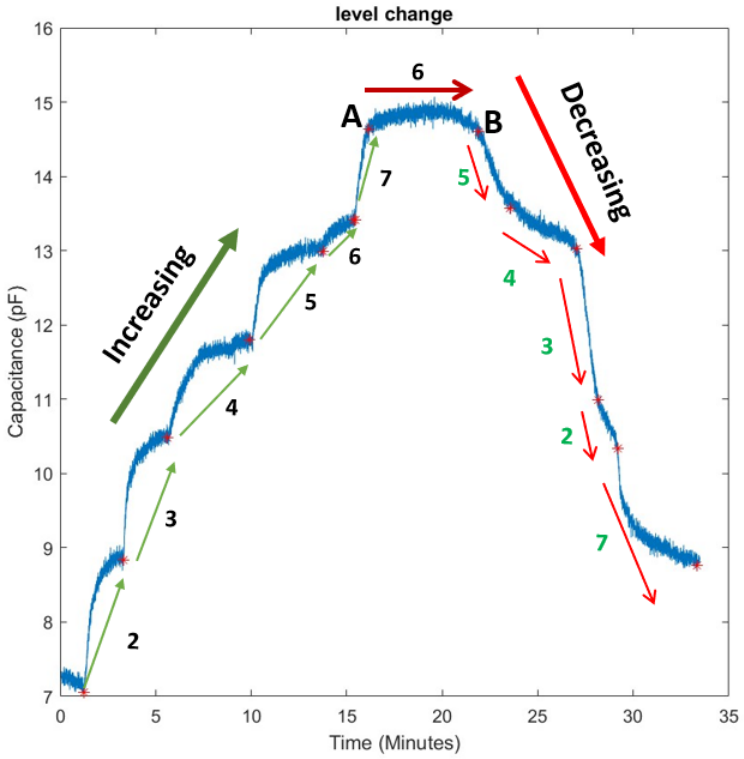

Figure 29: Level of capacitance change due to change of liquid.

In Figure 28 (a) a schematic image of a 3D vascularized chip is shown, and wherein Figure 28(b) the actual 3D vascularization chip is presented where in Reservoir 1, the customized sensor was placed. The experiment was started by filling the Reservoir 2 with liquid through pipetting and the volume was 150 µl and then the, Reservoirs 3 to 7 was respectively filled with the same amount of liquid one after another.

From Figure 29, during the increasing cycle, the change of liquid level is illustrated where 2-7 represents the Reservoirs shown in Figure 28 (a) and (b). When the liquid was filled in Reservoir 2 and it started to increase, which is shown in Figure 29 with a green arrow and then filling the Reservoir with liquid continued until Reservoir 7 was filled and it reached the maximum point A and for each time, the liquid level changes is represented with green arrows in Figure 29 and the changes while decreasing is shown with red arrows. When the liquid was taken out from each Reservoir from Figure 29, as the center open-top compartment Reservoir had a larger diameter, it was not emptied at the beginning. The liquid was emptied from Reservoir 6 at first and the level should change when Reservoir 6 was emptied. But Figure 29 indicates that there was no liquid level change from point A to B. As the maximum level of increase of liquid level was at point A, it should decrease from that point. But it started to decrease from point B when Reservoir 5 was emptied. After that, the Reservoirs 4,3 and 2 were emptied, as mentioned in Figure 29. The open-top compartment, which is Reservoir 7, was emptied

at least. After analyzing the data with MATLAB, the maximum capacitance value was 29.1 pF and signal to noise ratio (SNR) is 19.30 dB.

However, the changes in the liquid level while it was increasing for Reservoirs 2-7 and also emptying the liquid from decreasing the liquid level from Reservoirs 6-2 and then Reservoir 7, the changes are not same for each of the Reservoirs especially in Reservoir 6 while increasing and in Reservoir 2 while decreasing. There could be some factors behind this behavior:

Fluid Flow Dynamics and Liquid Redistributions: The architecture and microchannel network of the vascularized chip affect fluid flow dynamics. Depending on the microchannels' size, geometry, and connection, the liquid may redistribute differently as the level rises. When the liquid level rises, the liquid starts to redistribute among all the reservoirs and liquid starts to flow from the reservoir that has a higher level of liquid to the reservoir with a lower liquid level to balance the liquid level. Variables, including channel width, length, and constrictions or barriers, affect the flow resistance and paths and may affect the redistribution process. Factors like hydrostatic pressure and surface tension and dynamic contact angle are responsible for this phenomenon.

Hydrostatic Pressure: An equilibrium fluid pressure caused by gravity is commonly known as hydrostatic pressure. It is the main force for liquid redistribution. The hydrostatic pressure in the bottom Reservoirs grows with the increased liquid levels. The increased pressure forces the liquid to move upward and toward the reservoirs at a higher level.

Surface Tension: The cohesive force between liquid molecules at the liquid-air contact is known as surface tension. The liquid-air interface widens as the liquid level rises. As the liquid level started to rise, the liquid might form a meniscus with the wall of the Reservoirs and due to the surface tension properties, the shape of the meniscus and the wettability of the sensor surface might have changed.

Pressure Differential: When the first reservoir is emptied, the liquid may not be immediately drawn from the adjacent Reservoirs due to fluid viscosity, flow resistance, or air bubbles. This can result in no change in the liquid level at first. As the second reservoir is emptied, a pressure differential may be established between the second reservoir and the connected microchannels. Emptying the second reservoir creates a pressure drop, causing the liquid to flow from the neighboring reservoirs toward the second reservoir to equalize the pressure. This results in a decrease in the liquid level in those reservoirs.

Dynamic Contact angle: Since the sensor surface is hydrophobic, however, the contact angle measured for the surface was different, so it might have a dynamic contact angle when the liquid forms a meniscus with the sensor surface and Reservoir walls. The term "dynamic contact angle" refers to how the contact angle changes when the liquid level changes. In this case, the liquid starts the dynamic contact angle behavior when it contacts the Reservoir walls or surfaces. Changes in the dynamic contact angle can impact the liquid's wetting behavior, adhesion, and flow patterns within the microchannels. The fundamental reason for the observed differences in liquid level is still most likely hydrostatic pressure.

Air Displacement: When emptying a Reservoir, air may enter the Reservoir or microchannels, displacing the liquid. This air displacement can create pressure differentials and flow paths that lead to liquid redistribution from other Reservoirs.

5.5 Challenges and Future Steps:

Challenges:

Oxidation: Oxidation due to moisture was one of the main challenges during the experiment. The sensor surface got oxidized and thus it affected the repeatability and accuracy of the sensor. In some sensors, the oxidation was too high that the sensor showed higher resistance that affected the capacitance value. So, better coating could be an option to get rid of oxidation.

Noise effect: During the experiment, factors might affect the sensor performance, and noise is one of them. Any sort of environmental factors like a change in temperature or any noise due to the electronic devices were used during the experiment might had effects on the experiment that resulted in the sensors' output performance. Utilizing shielding materials on the organ-on-chip system can minimize the noise and proper grounding techniques can reduce it further.

Sensor placement: During the experiment, the placement of the sensor in the liquid was a challenge as the experiment was performed in a very narrow space. If there was any movement of the sensor due to any external force that affected the sensor’s output. Ensuring protection from external movement can improve the experiment quality in this regard.

Surface Tension: The surface tension of the liquid had an effect during the experiment that might affect experimental sensor data. During the experiment, there was a meniscus formed close to the wall of the syringe and there were some bubbles on the liquid and on the sensor surface that might affect the data. The viscosity property of liquid might also affect the data of the sensor especially because it can affect the flow of the liquid.

However, it was tried to get rid of the meniscus and formation of bubbles while performing the experiment and the sensor design and coating on top of the surface were done that mitigates the viscosity problem.

Syringe pump effect: During the pumping of liquid while increasing and decreasing the liquid level, syringe pump speed or movement might have some effects like fluctuations that might cause errors in taking the experimental value. Another factor is that the syringe pump might have generated some air bubbles that affected the sensor reading and that might cause some errors.

Future Work:

Sensor design could be changed to get better output. The design was used is 1-1-1 pattern of interdigital sensors for the final application. However, other patterns for example, 1-5-1 or 1-11-1, can be used for future experiments. From theory, if more electrodes are used then the sensing area will increase which will help to measure the changes more accurately and the larger the width of the electrode better the capacitance and the gap between the electrodes are smaller which increases the capacitance. So, a sensor having more sensing area, with larger width of the electrode and a smaller gap between electrodes, make the better output for the sensor.

The substrate material that was used for fabricating the sensor was PCB-FR4. However, there were some challenges or errors for example, sensor surface roughness, during the experiment that might be possible to overcome by changing the substrate material. One replacement of substrate material could be glass.

Another option could be the microfabrication of the sensor in Clean Room using lithography. The sensor substrate material could be glass. It might have less oxidation effect than PCB substrate material. In addition, lithography is easy, and microfabrication will not take much time.

6. CONCLUSION

The goal of the thesis work was to develop a miniature capacitive sensor that can measure the liquid level in organ-on-chip applications. Different types of sensors were designed, fabricated, and tested to get accurate measurements of changes of liquid level based on the interdigital sensor theory. All the designed sensors had been successfully designed and validated through a methodical methodology and extensive experimentation. After the experimentation was done and the sensors showed accurate response along with high sensitivity, good range of capacitance and linearity then, all the sensor's performance were taken into consideration and comparisons between each sensor were done. From all the sensors, the best sensor was chosen which was Type B Version 3 and then it was customized considering the dimensions of the 3D vascularization chip. The experiment was performed in a 3D vascularization chip with the customized sensor named as Type B Version 4, which had similar properties as Type B Version 3 and has been successfully able to measure the changes of liquid level in the 3D vascularization chip. However, there were some limitations such as noise, drift, and fabrication errors due to materials properties that were discussed before and the solutions for the limitations are also discussed.

In conclusion, the designed and fabricated interdigital capacitive sensors for liquid-level measurement have been developed for organ-on-chip applications. The liquid that was used for the experiment was DPBS. As it was mentioned before, Type B Version 3 had shown better sensitivity, linearity and repeatability compared to all the sensors, so the theoretical and experimental data, such as sensitivity, and range of capacitance, were compared. The average theoretical sensitivity for the Type B Version 3 IDT sensor was 3.98 pF/mm when the liquid level was increasing. From the measurement findings, the average experimental sensitivity for Type B Version 3 while the liquid level was rising was 3.92 pF/mm. The theoretical sensitivity was almost close enough to the experimental sensitivity, except there were some minor errors due to experimental limitations.

Each sensor responds to changes in liquid level almost linearly. Fabrication of the sensor is simple, fast, inexpensive, and easily accessible. The findings show that the sensors are capable of accurately measuring liquid levels, and the customized sensor made for organ-on-chip applications was suitable as it responded well. So, it can be said that the goal of this study is achieved.

7. REFERENCES

[1] M. C. Koyilot *et al.*, “Breakthroughs and Applications of Organ-on-a-Chip Technology,” *Cells*, vol. 11, no. 11, Art. no. 11, Jan. 2022, doi: 10.3390/cells11111828.

[2] N. A. Ashammakhi and A. Elzagheid, “Organ-on-a-Chip: New Tool for Personalized Medicine,” *J. Craniofac. Surg.*, vol. 29, no. 4, p. 823, Jun. 2018, doi: 10.1097/SCS.0000000000004604.

[3] D. Paczesny, G. Tarapata, M. Michał, and R. Jachowicz, “The Capacitive Sensor for Liquid Level Measurement Made with Ink-jet Printing Technology,” *Procedia Eng.*, vol. 120, pp. 731–735, Jan. 2015, doi: 10.1016/j.proeng.2015.08.776.

[4] H. Canbolat, “A Novel Level Measurement Technique Using Three Capacitive Sensors for Liquids,” *IEEE Trans. Instrum. Meas.*, vol. 58, no. 10, pp. 3762–3768, Oct. 2009, doi: 10.1109/TIM.2009.2019715.

[5] S. N. Bhatia and D. E. Ingber, “Microfluidic organs-on-chips,” *Nat. Biotechnol.*, vol. 32, no. 8, pp. 760–772, Aug. 2014, doi: 10.1038/nbt.2989.

[6] T. Ahmed, “Organ-on-a-chip microengineering for bio-mimicking disease models and revolutionizing drug discovery,” *Biosens. Bioelectron. X*, vol. 11, p. 100194, Sep. 2022, doi: 10.1016/j.biosx.2022.100194.

[7] J. M. Donkers, H. Eslami Amirabadi, and E. van de Steeg, “Intestine-on-a-chip: Next level in vitro research model of the human intestine,” *Curr. Opin. Toxicol.*, vol. 25, pp. 6–14, Mar. 2021, doi: 10.1016/j.cotox.2020.11.002.

[8] C. M. Leung *et al.*, “A guide to the organ-on-a-chip,” *Nat. Rev. Methods Primer*, vol. 2, no. 1, Art. no. 1, May 2022, doi: 10.1038/s43586-022-00118-6.

[9] Y. A. Jodat *et al.*, “Human-Derived Organ-on-a-Chip for Personalized Drug Development,” *Curr. Pharm. Des.*, vol. 24, no. 45, pp. 5471–5486, Apr. 2019, doi: 10.2174/1381612825666190308150055.

[10] A. E. Danku, E.-H. Dulf, C. Braicu, A. Jurj, and I. Berindan-Neagoe, “Organ-On-A-Chip: A Survey of Technical Results and Problems,” *Front. Bioeng. Biotechnol.*, vol. 10, p. 840674, Feb. 2022, doi: 10.3389/fbioe.2022.840674.

[11] M. Potente and T. Mäkinen, “Vascular heterogeneity and specialization in development and disease,” *Nat. Rev. Mol. Cell Biol.*, vol. 18, no. 8, pp. 477–494, Aug. 2017, doi: 10.1038/nrm.2017.36.

[12] S. Fleischer, D. N. Tavakol, and G. Vunjak-Novakovic, “From Arteries to Capillaries: Approaches to Engineering Human Vasculature,” *Adv. Funct. Mater.*, vol. 30, no. 37, p. 1910811, 2020, doi: 10.1002/adfm.201910811.

[13] A. Hasan *et al.*, “Microfluidic techniques for development of 3D vascularized tissue,” *Biomaterials*, vol. 35, no. 26, pp. 7308–7325, Aug. 2014, doi: 10.1016/j.biomaterials.2014.04.091.

[14] S. Rafii, J. M. Butler, and B.-S. Ding, “Angiocrine functions of organ-specific endothelial cells,” *Nature*, vol. 529, no. 7586, pp. 316–325, Jan. 2016, doi: 10.1038/nature17040.

[15] S. Kim, W. Kim, S. Lim, and J. Jeon, “Vasculature-On-A-Chip for In Vitro Disease Models,” *Bioengineering*, vol. 4, no. 4, p. 8, Jan. 2017, doi: 10.3390/bioengineering4010008.

[16] Y. Martin and P. Vermette, “Bioreactors for tissue mass culture: Design, characterization, and recent advances,” *Biomaterials*, vol. 26, no. 35, pp. 7481–7503, Dec. 2005, doi: 10.1016/j.biomaterials.2005.05.057.

[17] J. W. Weisel and R. I. Litvinov, “Fibrin Formation, Structure and Properties,” in *Fibrous Proteins: Structures and Mechanisms*, D. A. D. Parry and J. M. Squire, Eds., in Subcellular Biochemistry, vol. 82. Cham: Springer International Publishing, 2017, pp. 405–456. doi: 10.1007/978-3-319-49674-0_13.

[18] G. K. Owens, M. S. Kumar, and B. R. Wamhoff, “Molecular Regulation of Vascular Smooth Muscle Cell Differentiation in Development and Disease,” *Physiol. Rev.*, vol. 84, no. 3, pp. 767–801, Jul. 2004, doi: 10.1152/physrev.00041.2003.

[19] P. Carmeliet, “Angiogenesis in life, disease and medicine,” *Nature*, vol. 438, no. 7070, pp. 932–936, Dec. 2005, doi: 10.1038/nature04478.

[20] M. Potente, H. Gerhardt, and P. Carmeliet, “Basic and Therapeutic Aspects of Angiogenesis,” *Cell*, vol. 146, no. 6, pp. 873–887, Sep. 2011, doi: 10.1016/j.cell.2011.08.039.

[21] A. M. A. O. Pollet and J. M. J. den Toonder, “Recapitulating the Vasculature Using Organ-On-Chip Technology,” *Bioengineering*, vol. 7, no. 1, p. 17, Feb. 2020, doi: 10.3390/bioengineering7010017.

[22] C. F. Buchanan, E. E. Voigt, C. S. Szot, J. W. Freeman, P. P. Vlachos, and M. N. Rylander, “Three-Dimensional Microfluidic Collagen Hydrogels for Investigating Flow-Mediated Tumor-Endothelial Signaling and Vascular Organization,” *Tissue Eng. Part C Methods*, vol. 20, no. 1, pp. 64–75, Jan. 2014, doi: 10.1089/ten.tec.2012.0731.
[23] L. Li, B. Li, J. Dong, and J. Zhang, “Roles of silanes and silicones in forming superhydrophobic and superoleophobic materials,” *J. Mater. Chem. A*, vol. 4, no. 36, pp. 13677–13725, 2016, doi: 10.1039/C6TA05441B.
[24] M. I. Bogorad, J. DeStefano, A. D. Wong, and P. C. Searson, “Tissue-engineered 3D microvessel and capillary network models for the study of vascular phenomena,” *Microcirculation*, vol. 24, no. 5, p. e12360, 2017, doi: 10.1111/micc.12360.
[25] R. Zhang and N. B. Larsen, “Stereolithographic hydrogel printing of 3D culture chips with biofunctionalized complex 3D perfusion networks,” *Lab. Chip*, vol. 17, no. 24, pp. 4273–4282, 2017, doi: 10.1039/C7LC00926G.
[26] P. Datta, B. Ayan, and I. T. Ozbolat, “Bioprinting for vascular and vascularized tissue biofabrication,” *Acta Biomater.*, vol. 51, pp. 1–20, Mar. 2017, doi: 10.1016/j.actbio.2017.01.035.
[27] Q. Gao *et al.*, “3D Bioprinting of Vessel-like Structures with Multilevel Fluidic Channels,” *ACS Biomater. Sci. Eng.*, vol. 3, no. 3, pp. 399–408, Mar. 2017, doi: 10.1021/acsbiomaterials.6b00643.
[28] S. Son, M. Cho, and J. Lee, “Crumbs proteins regulate layered retinal vascular development required for vision,” *Biochem. Biophys. Res. Commun.*, vol. 521, no. 4, pp. 939–946, Jan. 2020, doi: 10.1016/j.bbrc.2019.11.013.
[29] V. van Duinen, D. Zhu, C. Ramakers, A. J. van Zonneveld, P. Vulto, and T. Hankemeier, “Perfused 3D angiogenic sprouting in a high-throughput in vitro platform,” *Angiogenesis*, vol. 22, no. 1, pp. 157–165, Feb. 2019, doi: 10.1007/s10456-018-9647-0.
[30] L. L. Bischel, S.-H. Lee, and D. J. Beebe, “A Practical Method for Patterning Lumens through ECM Hydrogels via Viscous Finger Patterning,” *SLAS Technol.*, vol. 17, no. 2, pp. 96–103, Apr. 2012, doi: 10.1177/2211068211426694.
[31] S. Kim, M. Chung, J. Ahn, S. Lee, and N. L. Jeon, “Interstitial flow regulates the angiogenic response and phenotype of endothelial cells in a 3D culture model,” *Lab. Chip*, vol. 16, no. 21, pp. 4189–4199, 2016, doi: 10.1039/C6LC00910G.
[32] “Water Level Sensor | What, How, Where, Benefits, Types - Renke.” https://www.renkeer.com/water-level-sensor-definition-applications-benefits-types/ (accessed Mar. 27, 2023).
[33] A. Gholamzadeh, Y. Qiu, M. Zhang, S. Dang, and N. Hossain, “Sensor system to detect accidental bucket contact with structures and people,” in *2015 IEEE International Conference on Signal Processing, Informatics, Communication and Energy Systems (SPICES)*, Kozhikode, India: IEEE, Feb. 2015, pp. 1–4. doi: 10.1109/SPICES.2015.7091474.
[34] Y. Singh, S. K. Raghuwanshi, and S. Kumar, “Review on Liquid-level Measurement and Level Transmitter Using Conventional and Optical Techniques,” *IETE Tech. Rev.*, vol. 36, no. 4, pp. 329–340, Jul. 2019, doi: 10.1080/02564602.2018.1471364.
[35] T. Islam, O. P. Maurya, and A. U. Khan, “Design and Fabrication of Fringing Field Capacitive Sensor for Non-Contact Liquid Level Measurement,” *IEEE Sens. J.*, vol. 21, no. 21, pp. 24812–24819, Nov. 2021, doi: 10.1109/JSEN.2021.3112848.
[36] R. Xu, B. Wang, M. Zhang, N. Hossain, X. Zhang, and L. Yang, “Capacitive measurement system for liquid level measurement,” in *2016 5th International Conference on Computer Science and Network Technology (ICCSNT)*, Changchun, China: IEEE, Dec. 2016, pp. 810–815. doi: 10.1109/ICCSNT.2016.8070271.
[37] D. Wang, “Capacitive-Based Liquid Level Sensing Sensor Reference Design,” 2015.
[38] Y.-T. Li, C.-M. Chao, and K. Wang, “A capacitance level sensor design and sensor signal enhancement,” in *2011 6th IEEE International Conference on Nano/Micro Engineered and Molecular Systems*, Kaohsiung, Taiwan: IEEE, Feb. 2011, pp. 847–850. doi: 10.1109/NEMS.2011.6017486.
[39] C.-S. A. Gong, H. K. Chiu, L. R. Huang, C. H. Lin, Z. D. Hsu, and P.-H. Tu, “Low-Cost Comb-Electrode Capacitive Sensing Device for Liquid-Level Measurement,” *IEEE Sens. J.*, vol. 16, no. 9, pp. 2896–2897, May 2016, doi: 10.1109/JSEN.2016.2524696.
[40] T. Islam and O. P. Maurya, “Design and fabrication of non-contact fringing field capacitive sensor for liquid level measurement,” in *2019 IEEE 16th India Council International*

Conference (INDICON), Rajkot, India: IEEE, Dec. 2019, pp. 1–4. doi: 10.1109/INDICON47234.2019.9029048.

[41] A. Le, “Ultrasonic Sensing Basics for Liquid Level Sensing, Flow Sensing, and Fluid Identification Applications,” 2015.

[42] A. Inc., “A Dozen Ways to Measure Fluid Level, How They Work.” ABB. [Online]. Available: https://library.e.abb.com/public/c516a8b5766d4b25a9e02836f79a4db7/AT_A_Dozen_Ways_to_Measure_Fluid_Level.pdf

[43] L. Umar, “Self-Controled PTC Sensor For Level Measurement of Liquids in Tanks,” Jan. 2001, Accessed: May 18, 2023. [Online]. Available: https://www.academia.edu/8901379/Self_Controled_PTC_Sensor_For_Level_Measurement_of_Liquids_in_Tanks

[44] K. R. Efferson, “A Superconducting (Nb-Ti) Liquid Helium Level Detector,” in *Advances in Cryogenic Engineering*, K. D. Timmerhaus, Ed., in Advances in Cryogenic Engineering. Boston, MA: Springer US, 1995, pp. 124–131. doi: 10.1007/978-1-4757-0513-3_18.

[45] Ashlin, “What is an optical level sensor and how does it work?,” *Instrumentation and Control Engineering*, Jan. 01, 2021. https://automationforum.co/what-is-an-optical-level-sensor-and-how-does-it-work/ (accessed May 08, 2023).

[46] theinstrument guru, “Working principle of optical Type level Switch,” *THE INSTRUMENT GURU*, Dec. 08, 2020. https://theinstrumentguru.com/working-principle-of-optical-type-level-switch/ (accessed May 08, 2023).

[47] C. Yang, S. Chen, and G. Yang, “Fiber optical liquid level sensor under cryogenic environment,” 2001.

[48] J. Shim, “Liquid level measurement system using capacitive sensor and optical sensor,” *J. Korean Soc. Mar. Eng.*, vol. 37, no. 7, pp. 778–783, Nov. 2013, doi: 10.5916/jkosme.2013.37.7.778.

[49] H. Golnabi, “Design and operation of a fiber optic sensor for liquid level detection,” *Opt. Lasers Eng.*, vol. 41, no. 5, pp. 801–812, May 2004, doi: 10.1016/S0143-8166(03)00035-6.

[50] C.-W. Lai, Y.-L. Lo, J.-P. Yur, and C.-H. Chuang, “Application of Fiber Bragg Grating Level Sensor and Fabry-Pérot Pressure Sensor to Simultaneous Measurement of Liquid Level and Specific Gravity,” *IEEE Sens. J.*, vol. 12, no. 4, pp. 827–831, Apr. 2012, doi: 10.1109/JSEN.2011.2161075.

[51] P. Raatikainen, I. Kassamakov, R. Kakanakov, and M. Luukkala, “Fiber-optic liquid-level sensor,” 1997.

[52] V. Bello and E. Bodo, “A NIR-Spectroscopy-Based Approach for Detection of Fluids in Rectangular Glass Micro-Capillaries,” in *7th International Electronic Conference on Sensors and Applications*, MDPI, Nov. 2020, p. 43. doi: 10.3390/ecsa-7-08250.

[53] Utmel, “What is a Capacitive Sensor?” https://www.utmel.com/blog/categories/sensors/what-is-a-capacitive-sensor (accessed May 08, 2023).

[54] “Capacitive sensing - Sensor technology.” https://wiki.metropolia.fi/display/sensor/Capacitive+sensing

[55] X. Hu and W. Yang, “Planar capacitive sensors – designs and applications,” *Sens. Rev.*, vol. 30, no. 1, pp. 24–39, Jan. 2010, doi: 10.1108/02602281011010772.

[56] X. B. Li, S. D. Larson, A. S. Zyuzin, and A. V. Mamishev, “Design principles for multichannel fringing electric field sensors,” *IEEE Sens. J.*, vol. 6, no. 2, pp. 434–440, Apr. 2006, doi: 10.1109/JSEN.2006.870161.

[57] K. Chetpattananondh, T. Tapoanoi, P. Phukpattaranont, and N. Jindapetch, “A self-calibration water level measurement using an interdigital capacitive sensor,” *Sens. Actuators Phys.*, vol. 209, pp. 175–182, Mar. 2014, doi: 10.1016/j.sna.2014.01.040.

[58] S. C. Bera, J. K. Ray, and S. Chattopadhyay, “A Low-Cost Noncontact Capacitance-Type Level Transducer for a Conducting Liquid,” *IEEE Trans. Instrum. Meas.*, vol. 55, no. 3, pp. 778–786, Jun. 2006, doi: 10.1109/TIM.2006.873785.

[59] F. Reverter, X. Li, and G. C. M. Meijer, “Liquid-level measurement system based on a remote grounded capacitive sensor,” *Sens. Actuators Phys.*, vol. 138, no. 1, pp. 1–8, Jul. 2007, doi: 10.1016/j.sna.2007.04.027.

[60] K. Loizou, E. Koutroulis, D. Zalikas, and G. Liontas, “A low-cost capacitive sensor for water level monitoring in large-scale storage tanks,” in *2015 IEEE International Conference on Industrial Technology (ICIT)*, Seville: IEEE, Mar. 2015, pp. 1416–1421. doi: 10.1109/ICIT.2015.7125295.

[61] S. Prabhu, C. Gooneratne, K. Hoang, S. C. Mukhopadhyay, A. Davidson, and G. Liu, “Interdigital Sensing System for Kidney Health Monitoring,” 2021, pp. 267–309. doi: 10.1007/978-3-030-62684-6_11.
[62] Lu Guirong and Chen Shuyue, “A capacitive liquid level sensor with four electrodes,” in *2010 3rd International Conference on Computer Science and Information Technology*, Chengdu, China: IEEE, Jul. 2010, pp. 628–632. doi: 10.1109/ICCSIT.2010.5564467.
[63] S. Khan *et al.*, “A non-contact capacitance type level transducer for liquid characterization,” in *2008 International Conference on Computer and Communication Engineering*, Kuala Lumpur, Malaysia: IEEE, May 2008, pp. 1264–1269. doi: 10.1109/ICCCE.2008.4580808.
[64] “What is Stray Capacitance?” http://www.learningaboutelectronics.com/Articles/What-is-stray-capacitance (accessed May 09, 2023).
[65] A. Lata, B. Kumar, and N. Mandal, “Design and development of a level transmitter using force resistive sensor as a primary sensing element,” *IET Sci. Meas. Technol.*, vol. 12, no. 1, pp. 118–125, 2018, doi: 10.1049/iet-smt.2016.0513.
[66] B. Kumar, G. Rajita, and N. Mandal, “A Review on Capacitive-Type Sensor for Measurement of Height of Liquid Level,” *Meas. Control*, vol. 47, no. 7, pp. 219–224, Sep. 2014, doi: 10.1177/0020294014546943.
[67] A. V. Mamishev, K. Sundara-Rajan, Fumin Yang, Yanqing Du, and M. Zahn, “Interdigital sensors and transducers,” *Proc. IEEE*, vol. 92, no. 5, pp. 808–845, May 2004, doi: 10.1109/JPROC.2004.826603.
[68] M. Varshney and Y. Li, “Interdigitated array microelectrodes based impedance biosensors for detection of bacterial cells,” *Biosens. Bioelectron.*, vol. 24, no. 10, pp. 2951–2960, Jun. 2009, doi: 10.1016/j.bios.2008.10.001.
[69] R. Igreja and C. J. Dias, “Analytical evaluation of the interdigital electrodes capacitance for a multi-layered structure,” *Sens. Actuators Phys.*, vol. 112, no. 2–3, pp. 291–301, May 2004, doi: 10.1016/j.sna.2004.01.040.
[70] A. R. Mohd Syaifudin, S. C. Mukhopadhyay, and P. L. Yu, “Modelling and fabrication of optimum structure of novel interdigital sensors for food inspection,” *Int. J. Numer. Model. Electron. Netw. Devices Fields*, vol. 25, no. 1, pp. 64–81, Jan. 2012, doi: 10.1002/jnm.813.
[71] J. Z. Chen, A. A. Darhuber, S. M. Troian, and S. Wagner, “Capacitive sensing of droplets for microfluidic devices based on thermocapillary actuation,” *Lab. Chip*, vol. 4, no. 5, p. 473, 2004, doi: 10.1039/b315815b.
[72] “Advantages of Resistive Sensor | disadvantages of Resistive Sensor.” https://www.rfwireless-world.com/Terminology/Advantages-and-Disadvantages-of-Resistive-Sensor.html (accessed May 18, 2023).
[73] E. Staff, “What is Thermal Differential Level Measurement? - InstrumentationTools,” *Inst Tools*, Dec. 09, 2019. https://instrumentationtools.com/thermal-differential-level-measurement/ (accessed May 18, 2023).
[74] humans.txt, “Capacitive level sensor Endress+Hauser Liquicap FMI21-A1A1C1|500mm.” https://www.automation24.fr/capteur-de-niveau-capacitif-endress-hauser-liquicap-fmi21-a1a1c1-500-mm (accessed Mar. 29, 2023).
[75] “MFS Microfluidic Thermal Flow Sensor,” *Darwin Microfluidics*. https://darwin-microfluidics.com/products/microfluidic-thermal-flow-sensor (accessed Mar. 29, 2023).
[76] “Bronkhost.” https://www.bronkhorst.com/int/
[77] “Microfluidic flow control - Elveflow - setup.” https://www.elveflow.com/microfluidic-application-notes/setup-microfluidic-flow-control/ (accessed Mar. 29, 2023).
[78] “Microfluidic Pressure Sensor, uPS,” *LabSmith*. https://labsmith.com/product/uprocess-pressure-sensor-ups/ (accessed Mar. 29, 2023).
[79] “Ultrasonic distance measuring sensors: UNAM 12U9914/S14D.” https://www.baumer.com/ch/en/p/27803 (accessed Mar. 29, 2023).
[80] P. VSI, “What is Parylene Coating?” https://vsiparylene.com/about-parylene/#deposition-process
[81] J. Ortigoza-Diaz *et al.*, “Techniques and Considerations in the Microfabrication of Parylene C Microelectromechanical Systems,” *Micromachines*, vol. 9, no. 9, Art. no. 9, Sep. 2018, doi: 10.3390/mi9090422.
[82] Micro Metal, “Parylene is the ultimate protective coating.” https://www.micrometal.de/en/service-portfolio/additional-services/paratechcoating/
[83] D. B. Mitzi, L. L. Kosbar, C. E. Murray, M. Copel, and A. Afzali, “High-mobility ultrathin semiconducting films prepared by spin coating,” *Nature*, vol. 428, no. 6980, Art. no. 6980, Mar. 2004, doi: 10.1038/nature02389.

[84] “Spin Coat Theory – Cleanroom Research Laboratory.” https://cleanroom.utdallas.edu/manuals/spin-coat-theory/ (accessed May 18, 2023).
[85] “Professor Robert B. Laughlin, Department of Physics, Stanford University.” http://large.stanford.edu/courses/2007/ph210/hellstrom1/ (accessed May 18, 2023).
[86] A. Bagwari, J. Bagwari, and G. S. Tomar, “Smart Sensor for the Underwater Communication Signal,” *Wirel. Pers. Commun.*, vol. 116, no. 2, pp. 1463–1480, Jan. 2021, doi: 10.1007/s11277-020-07995-8.
[87] “AN367: Understanding Capacitive Sensing Signal to Noise Ratios”.

APPENDIX:

In Appendix, there are supplementary information regarding the thesis work. The Appendix is divided in three chapter.
In chapter A, Table A1 and Table A2 are presented where the thickness of parylene C coating is shown for 5 µm and 10 µm thickness.

In chapter B, the images showing maximum and minimum capacitance, slope for 10 cycles while liquid level is increasing and decreasing and sensitivity of one cycle while liquid level increasing and decreasing of different types of sensors including their versions are presented.

In chapter C MATLAB code along with algorithm and functions are shown. The algorithm is to understand how the code was made and then using the functions and the code the results and data were analyzed.

APPENDIX A:

Table A1: Parylene coating recipe for 5 µm thickness insulation layer

Step	1	2	3	4	5	6	7	8	9	10	11	12
Time ramp	1	1	20	5	1	1	1	1	1	1	1	1
Temperature	120	130	145	171	170	171	170	171	170	171	170	171
Time soak	1	1	5	1	1	1	1	1	1	1	1	20

Door TD	Vac 1	Vac End	Pyrolysis	Postpy	Prepy	Gage	Champ
20	10	0	650	220	220	122	123

APPENDIX A:

Table A2: Parylene coating recipe for 10 µm thickness insulation layer

Step	1	2	3	4	5	6	7	8	9	10	11	12
Time ramp	1	1	60	30	1	1	1	1	1	1	1	1
Temperature	120	130	145	171	170	171	170	171	170	171	170	171
Time soak	1	10	45	5	1	1	1	1	1	1	1	20

Door TD	Vac 1	Vac End	Pyrolysis	Postpy	Prepy	Gage	Champ
20	10	0	650	220	220	122	123

APPENDIX B-1: TYPE-A, V-1

Figure 01 represents the minimum and maximum value for capacitance of Type A Version 1 sensor and Figure 02 represents the increasing and decreasing slope while Figure 03 represents sensitivity for only one cycle rising and decreasing of liquid level.

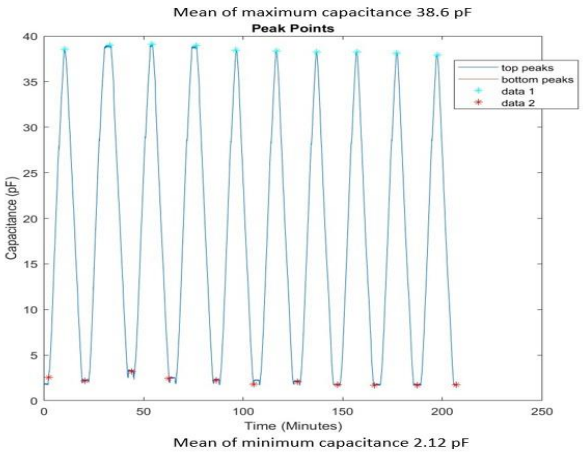

Figure 01: Maximum and minimum capacitance.

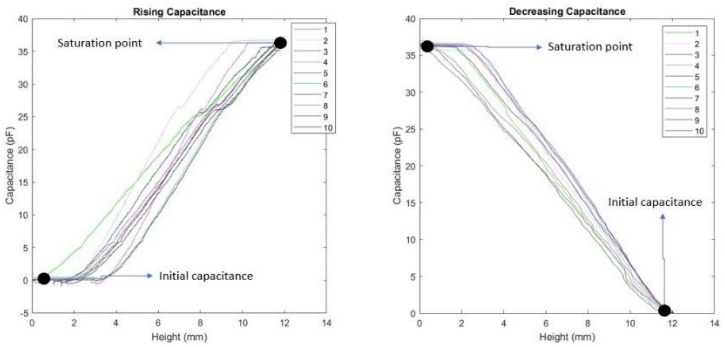

Figure 02: Slope of increasing and decreasing capacitance.

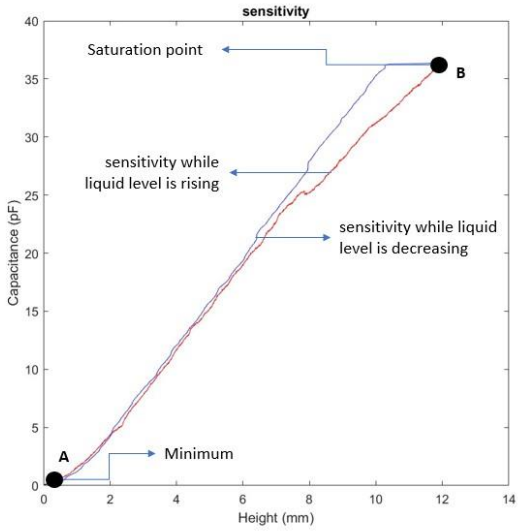

Figure 03: Sensitivity graph.

APPENDIX B-2: TYPE-A, V-2

Figure 04 represents the minimum and maximum value for capacitance of Type A Version 2 sensor and Figure 05 represents the increasing and decreasing slope while Figure 06 represents sensitivity for only one cycle rising and decreasing of liquid level.

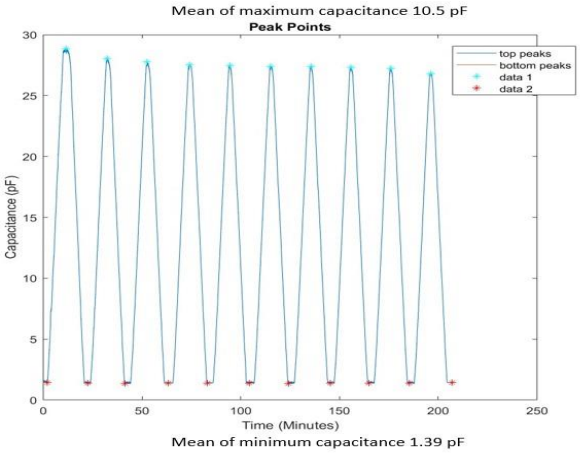

Figure 04: Maximum and minimum capacitance.

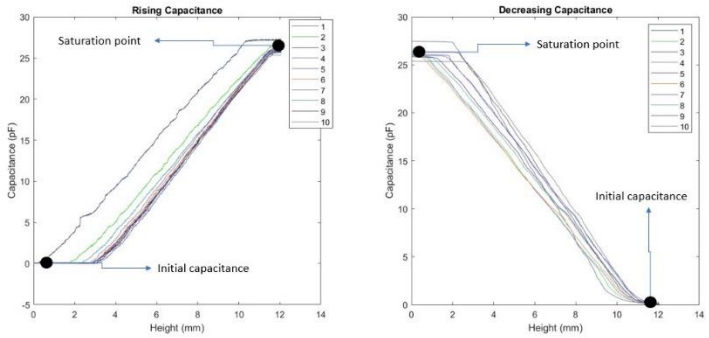

Figure 05: Slope of increasing and decreasing capacitance.

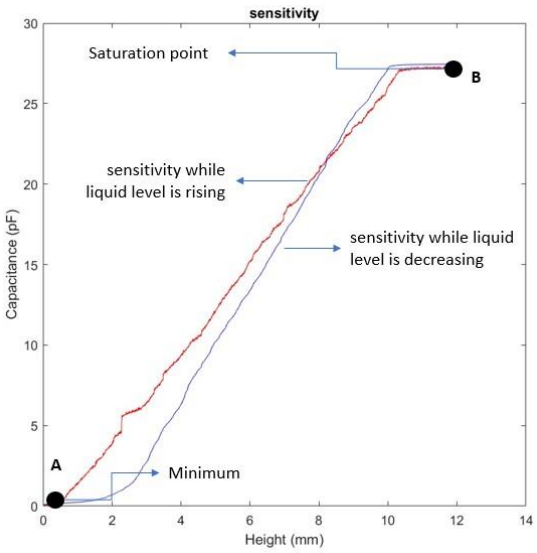

Figure 06: Sensitivity graph

APPENDIX B-3: TYPE-A, V-3

Figure 07 represents the minimum and maximum value for capacitance of Type A Version 3 sensor and Figure 08 represents the increasing and decreasing slope while Figure 09 represents sensitivity for only one cycle rising and decreasing of liquid level.

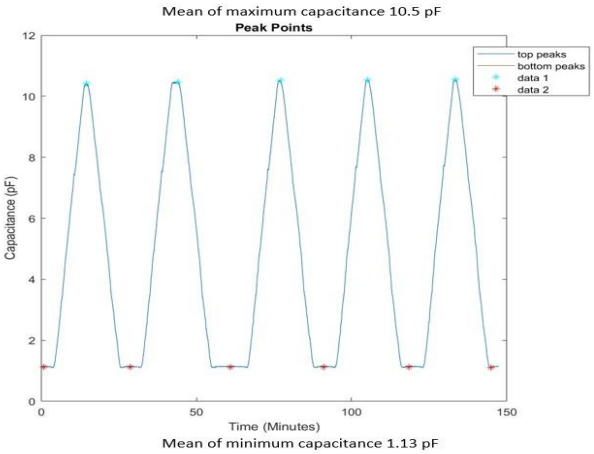

Figure 07: Maximum and minimum capacitance.

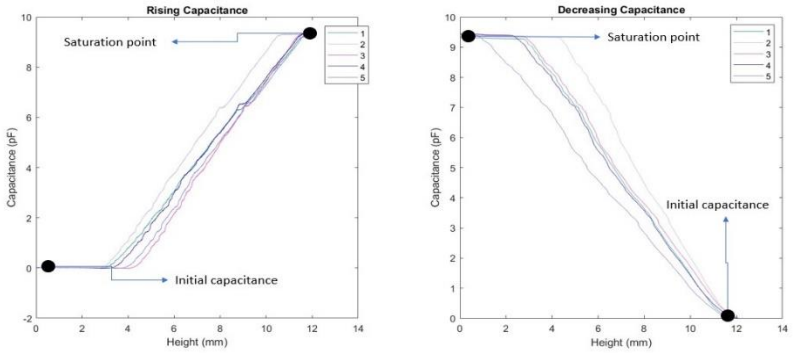

Figure 08: Slope of increasing and decreasing capacitance.

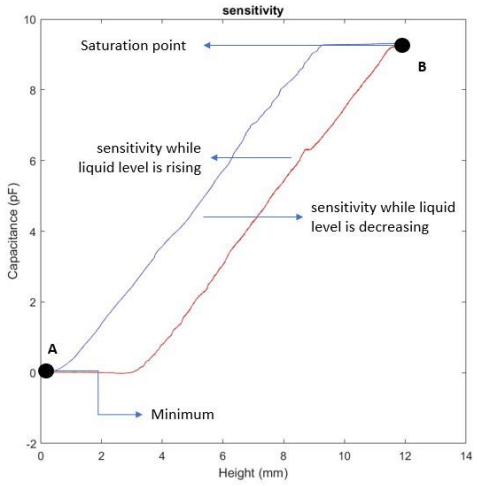

Figure 09: Sensitivity graph.

APPENDIX B-4: TYPE-A, V-4

Figure 010 represents the minimum and maximum value for capacitance of Type A Version 4 sensor and Figure 011 represents the increasing and decreasing slope while Figure 012 represents sensitivity for only one cycle rising and decreasing of liquid level.

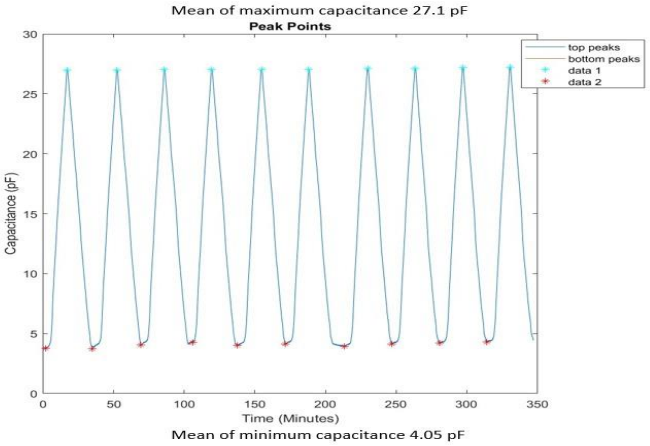

Figure 010: Maximum and minimum capacitance.

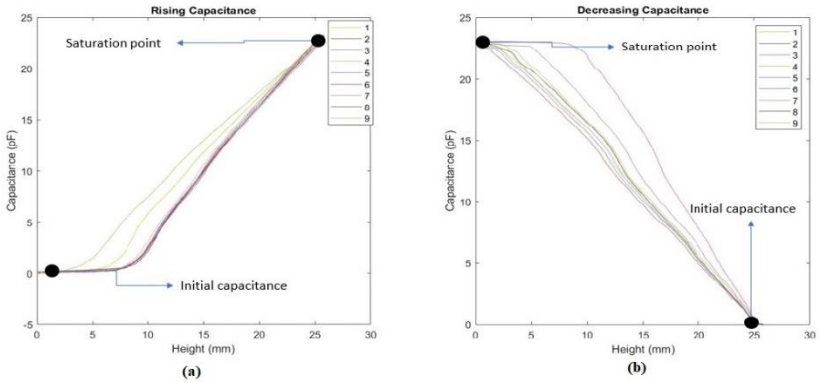

Figure 011: Slope of increasing and decreasing capacitance.

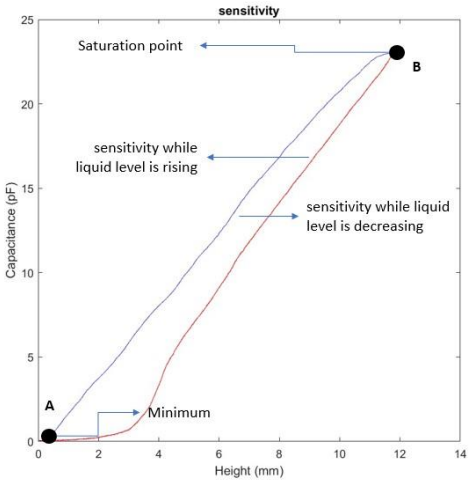

Figure 012: Sensitivity graph.

APPENDIX B-5: TYPE-B, V-1

Figure 013 represents the minimum and maximum value for capacitance of Type B Version 1 sensor and Figure 014 represents the increasing and decreasing slope while Figure 015 represents sensitivity for only one cycle rising and decreasing of liquid level.

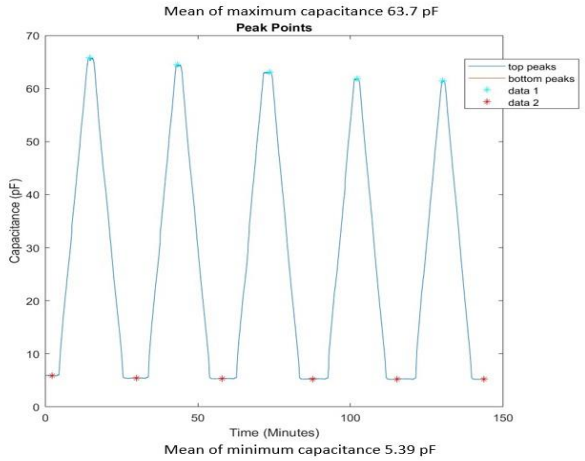

Figure 013: Maximum and minimum capacitance.

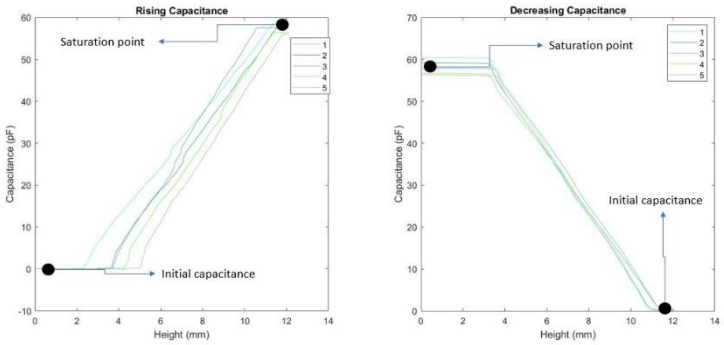

Figure 014: Slope of increasing and decreasing capacitance.

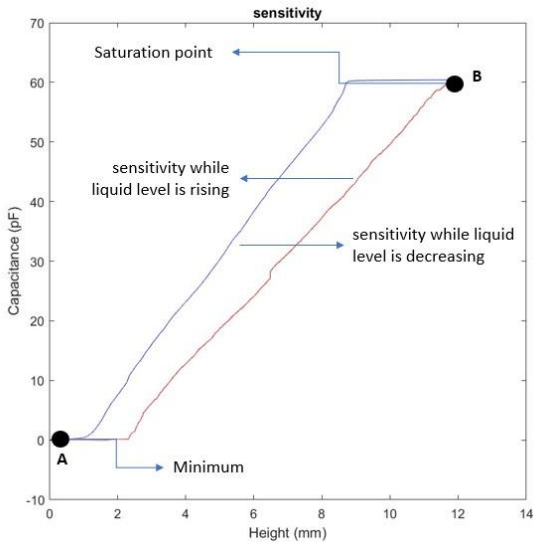

Figure 015: Sensitivity graph.

APPENDIX B-6: TYPE-B, V-2

Figure 016 represents the minimum and maximum value for capacitance of Type B Version 2 sensor and Figure 017 represents the increasing and decreasing slope while Figure 018 represents sensitivity for only one cycle rising and decreasing of liquid level.

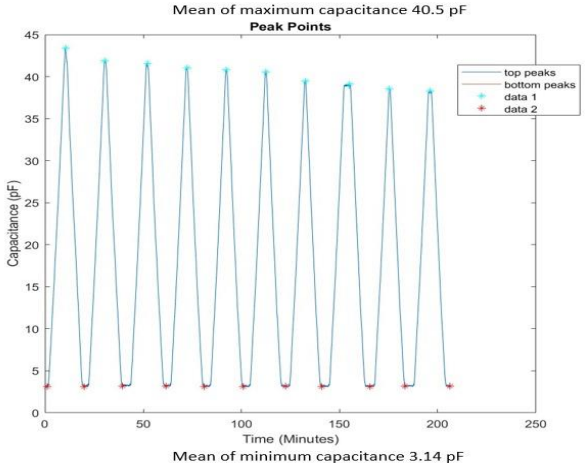

Figure 016: Maximum and minimum capacitance.

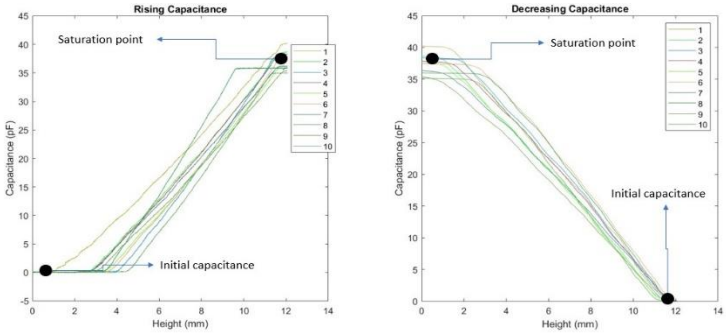

Figure 017: Slope of increasing and decreasing capacitance.

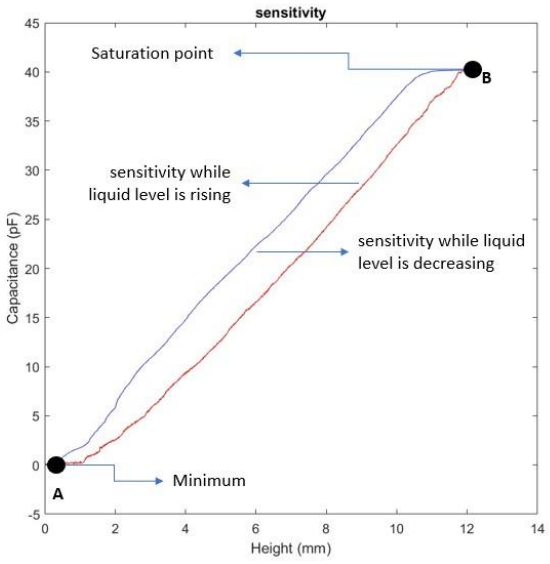

Figure 018: Sensitivity graph.

APPENDIX B-7: TYPE-C, V-1

Figure 019 represents the minimum and maximum value for capacitance of Type C Version 1 sensor and Figure 020 represents the increasing and decreasing slope while Figure 021 represents sensitivity for only one cycle rising and decreasing of liquid level.

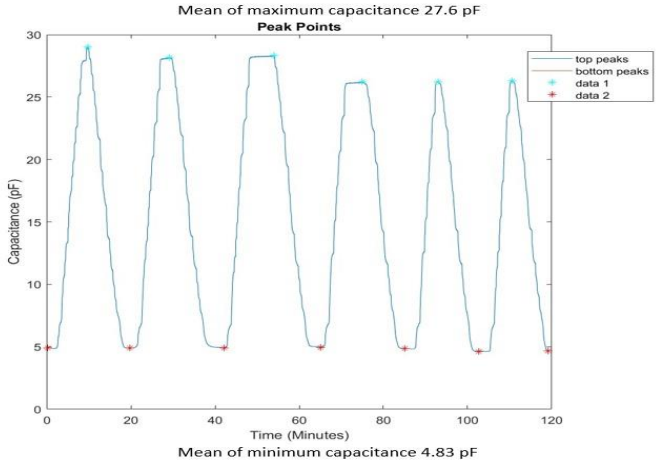

Figure 019: Maximum and minimum capacitance.

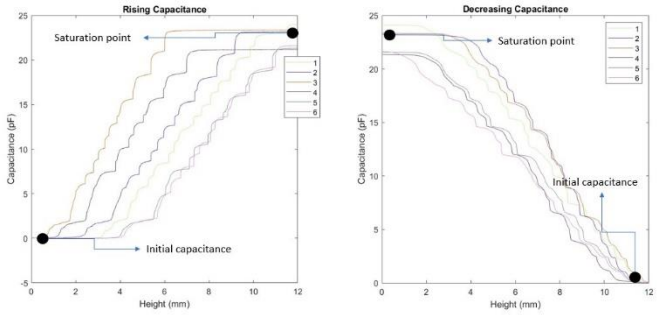

Figure 020: Slope of increasing and decreasing capacitance.

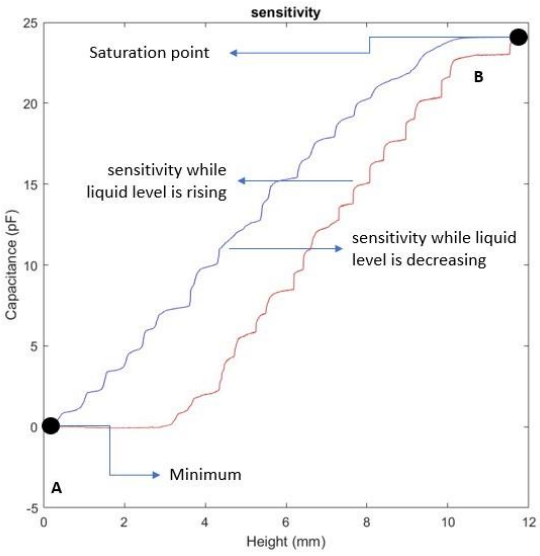

Figure 021: Sensitivity graph.

APPENDIX C :

%%%%%%%%%%%%%% File name: peak_slope_finder.m %%%%%%%%%%%%

%%

```
% Time series data Analysis
% Signal top and bottom Peaks estimation
% Signal slope estimation
% Author: D_M
%Date:
% Inputs:
% Capacitance: nx1 array
% Time: nx1 array
% Outputs:
% Top and bottom signal Peaks
% signal slope considering sliding window
%%%%%%%%%%%%%%%%%%%%%%%%%%%%%%%%%%%%
%%
clc
clear all;
close all;
load('filename, 'data')   %%% File name can be replaced with appropriate file that contains capacitance value with corresponding time stamp
time = data(:,1);
capacitance = data(:,2);
sSHight = H; % Sensor's sensing height, replace H by sensor’s sensing height
figure(1)
plot(time, capacitance)
% Estimate the SNR of the signal
dt = mean(diff(time));
fs = 1/dt ;
SNR_sig = snr(capacitance, fs);
%%
% Sensitivity Computation related parameters
% sSHight = 27 ;% Unit in mm. change this value to get other sensor sensitivity information
% len = length(time(25:3000));
% sig_r = capacitance(25:3000);
% sensi = sensitivity(sig_r, "rise");
% height_arr = nparticition(sSHight, len);
% length(height_arr)
% length(sensi)
% plot( height_arr, sensi)

%%
% Fixed window is used to find the signal top and bottom peaks
%
[tPeaks1, tIdx1, bPeaks1, bIdx1] = signallocalPeakFinder(capacitance, capacitance, w);% window size, w= 65

figure(2);
```

```
43.             plot(time,capacitance);
44.             hold on
45.             plot(time(tIdx1),capacitance(tIdx1),'c*');
46.             plot(time(bIdx1),capacitance(bIdx1),'r*');
47.             hold off
48.
49.             %%
50.             % please adjust the last parameter of "next_min_max" function
51.             % last parameter decide how many neighbors will be considered to find the
52.             % top peaks position  or bottom peak position of the curve !
53.             [rtpeaks, rbpeaks, rtidx, rbidx] = next_min_max(capacitance, tPeaks1,
bPeaks1,2);
54.             %[rtpeaks1, rbpeaks1, rtdx1, rbidx1] = next_min_max2(capacitance, rtpeaks,
rbpeaks, 2);
55.             figure(3);
56.             plot(time,capacitance);
57.             hold on
58.             plot(time(rtidx),capacitance(rtidx),'c*');
59.             plot(time(rbidx),capacitance(rbidx),'r*');
60.             hold off
61.
62.             %%
63.             [rtpeaks1, rbpeaks1, rtidx1, rbidx1] = global_peaks(capacitance,rtpeaks,
rbpeaks, rtidx, rbidx);
64.             %  a=figure('Units','centimeters','Position',[10 10 8 6*8/6]);
65.              figure(4)
66.             plot(time/60,capacitance*1e12);
67.             axis square
68.             title('Peak Points')
69.             xlabel("Time (Minutes)")
70.             ylabel("Capacitance (pF)")
71.             % legend('bottom peaks');
72.             % legend ( 'topeaks', 'bottom peaks', 'Location', 'northeast', 'Color',[1 1 1]);
73.             hold on
74.             % box off
75.             % legend box off
76.
77.             plot(0,0)
78.             plot(time(rtidx1)/60,capacitance(rtidx1)*1e12,'c*');
79.             plot(time(rbidx1)/60,capacitance(rbidx1)*1e12,'r*');
80.             hold off
81.             legend('top peaks','bottom peaks','data 1','data 2')
82.             %  print(a,'peakpoints.png','-dpng','-r600')
83.
84.             %%
85.             % estimate slope of a fixed window using bottom and top peak values
86.             % sliding window-based slope estimation
87.             % forcing the slope to remain postive
88.             tpIdx = rtidx1;
89.             bpIdx =  rbidx1;
90.             slope_w_size = 50; % change this variable to get different number of slope
values
```

```
91.             slope_val11 = {};
92.             slope_val22 = {};
93.             cnt_inc5 = 1;
94.             cnt_dec5 = 1;
95.             cnt5 = 1;
96.             cnt55 = 1;
97.             inc_nw = {};
98.             dec_nw = {};
99.             len = abs(length(bpIdx) - length(tpIdx))+1;
100.            for p = 1:length(tpIdx)-len
101.               low_res = bpIdx(p);
102.               high_res = tpIdx(p);
103.
104.               d_low_res = tpIdx(p) ;% window lower resolution
105.               d_high_res = bpIdx(p+1) ;% window upper resolution
106.
107.               rising1 = capacitance(low_res:high_res);
108.               decreasing1 = capacitance(d_low_res:d_high_res);
109.               rising_time1 = time(low_res:high_res);
110.               decreasing_time1 = time(d_low_res:d_high_res);
111.
112.               incr_rng = 0;
113.               for q = 1:slope_w_size:length(rising1)-(slope_w_size+1)
114.                  incr_rng = q+slope_w_size;
115.                  time_w_inc = rising_time1(q:incr_rng);
116.                  cap_w_inc =  rising1(q:incr_rng); % each window is subdivided by the slope
window size
117.                  rcln = length(cap_w_inc);
118.                  rise_time_x1 = time_w_inc(1);
119.                  rise_time_x2 = time_w_inc(rcln);
120.                  rise_y1 = cap_w_inc(1);
121.                  rise_y2 = cap_w_inc(rcln);
122.                  w_inc_slope = slope_estimation(rise_time_x1, rise_y1, rise_time_x2,
rise_y2);
123.                  slope_val11{cnt5} = w_inc_slope;%slope value of each small window of
rising section
124.                  cnt5 = cnt5 + 1;
125.               end
126.
127.               dec_rng = 0;
128.               for r = 1:slope_w_size:length(decreasing1)-(slope_w_size+1)
129.                  dec_rng = r+slope_w_size;
130.                  time_w_dec = decreasing_time1(r:dec_rng);
131.                  cap_w_dec = decreasing1(r:dec_rng); % each window is subdivided by the
slope window size
132.                  dcln = length(cap_w_dec);
133.                  % decreasing part
134.                  dec_rtime_x1 = time_w_dec(1);
135.                  dec_rtime_x2 = time_w_dec(dcln);
136.                  dec_dec_y1 = cap_w_dec(1);
137.                  dec_dec_y2 = cap_w_dec(dcln);
```

```
138.                 w_dec_slope = slope_estimation(dec_rtime_x1,dec_dec_y1, dec_rtime_x2,
dec_dec_y2);
139.                 slope_val22{cnt55} = w_dec_slope;
140.                 cnt55 = cnt55 + 1;
141.               end
142.
143.           end
144.
145.           slope_incr_11 = cell2mat(slope_val11);
146.           slope_dec_22 = cell2mat(slope_val11);
147.           figure(5);
148.           subplot(3,1,1)
149.           plot(time,capacitance);
150.           hold on
151.           plot(time(tpIdx),capacitance(tpIdx),'c*');
152.           plot(time(bpIdx),capacitance(bpIdx),'r*');
153.           subplot(3,1,2)
154.           plot(slope_incr_11, '--')
155.           subplot(3,1,3)
156.           plot(slope_dec_22, '--')
157.           hold off
158.
159.           %% estimate slope of a fixed window using bottom and top peak values
160.           slope_w_size1 = 100; % change this variable to get different number of slope
values
161.           slope_val1 = {};
162.           slope_val2 = {};
163.           riseAll_std = {};
164.           decAll_std = {};
165.           riseh= {};
166.           rise_sensi= {};
167.           dcrh= {};
168.           dcrh_sensi= {};
169.           cnt6 = 1;
170.           cnt7 = 1;
171.           rcnt= 1;
172.           dcnt= 1;
173.
174.           if length(bpIdx) > length(tpIdx)
175.              %len = (length(bpIdx) - length(tpIdx))
176.              for p = 1:length(tpIdx)
177.                 low_res1 = bpIdx(p);
178.                 high_res1 = tpIdx(p);
179.                 d_low_res = tpIdx(p) ;% window lower resolution
180.                 %if length(bpIdx) == length(tpIdx) + 1
181.                 d_high_res = bpIdx(p+1) ;% window upper resolution
182.                 %end
183.                 rising = capacitance(low_res1:high_res1);
184.                 decreasing = capacitance(d_low_res:d_high_res);
185.                 rising_time = time(low_res1:high_res1);
186.                 decreasing_time = time(d_low_res:d_high_res);
187.
```

```
188.                % sensitivity estimation
189.                rtime_len = length(rising_time);
190.                rheight_arr = nparticition(sSHight, rtime_len);
191.                rsensitivity = cap_sensitivity(rising, "rise");
192.                dtime_len = length(decreasing_time);
193.                dheight_arr = nparticition(sSHight, dtime_len);
194.                dsensitivity = cap_sensitivity(decreasing, "decrease");
195.
196.
197.                riseh{rcnt}= rheight_arr;
198.                rise_sensi{rcnt}= rsensitivity;
199.                dcrh{dcnt}=  dheight_arr;
200.                dcrh_sensi{dcnt}= dsensitivity;
201.
202.               color_val=rand(1,3);
203.
204.                figure(61)
205.                subplot(121)
206.          %        hold on
207.                plot(rheight_arr,
(rsensitivity)*1e12,'DisplayName',num2str(rcnt),'Color',color_val)
208.          %        legend(num2str(rcnt))
209.                hold on
210.                axis square
211.                title('Rising Capacitance')
212.                xlabel("Height (mm)")
213.                ylabel("Capacitance (pF)")
214.          %        hold off
215.                legend
216.
217.                subplot(122)
218.          %        hold on
219.                plot(dheight_arr, (sort(dsensitivity,
'descend'))*1e12,'DisplayName',num2str(dcnt),'Color',color_val );
220.          %        legend(num2str(dcnt))
221.                hold on
222.
223.                axis square
224.                title('Decreasing Capacitance')
225.                xlabel("Height (mm)")
226.                ylabel("Capacitance (pF)")
227.          %        hold off
228.                 legend
229.
230.                rcnt=rcnt+1;
231.                dcnt=dcnt+1;
237.                figure(6);
238.                subplot(121)
239.                hold on
240.                plot(rising);
241.                title('rising curves')
242.                xlabel("Change of time (\Delta t) in seconds")
```

```
243.                    ylabel("Capacitance Change (\Delta C) in (F)")
244.                    hold off
245.                    subplot(122)
246.                    hold on
247.                    plot(decreasing);
248.                    title('decreasing curves')
249.                    xlabel("Change of time (\Delta t) in seconds")
250.                    ylabel("Capacitance Change (\Delta C) in (F)")
251.                    hold off
252.                    if ~isempty(rising) && ~isempty(rising_time)  &&
~isempty(decreasing_time) && ~isempty(decreasing)
253.                       rcln = length(rising);
254.                       dcln = length(decreasing);
255.                       % rising part
256.                       rise_time_x1 = rising_time(ceil(rcln-(rcln*0.65)));
257.                       rise_time_x2 = rising_time(ceil(rcln-(rcln*0.35)));
258.                       rise_y1 = rising(ceil(rcln-(rcln*0.65)));
259.                       rise_y2 = rising(ceil(rcln-(rcln*0.35)));
260.                       rise_signal = rising(ceil(rcln-(rcln*0.65)):ceil(rcln-(rcln*0.35)));
261.                       rstd = std(rise_signal);
262.                       riseAll_std{cnt6} = rstd;
263.                       w_inc_slope1 = slope_estimation(rise_time_x1, rise_y1, rise_time_x2,
rise_y2);
264.                       slope_val1{cnt6} = w_inc_slope1;
265.                       cnt6 = cnt6 + 1;
266.                       % decreasing part
267.                       dec_rtime_x1 = decreasing_time(ceil(dcln-(dcln*0.65)));
268.                       dec_rtime_x2 = decreasing_time(ceil(dcln-(dcln*0.35)));
269.                       dec_dec_y1 = decreasing(ceil(dcln-(dcln*0.65)));
270.                       dec_dec_y2 = decreasing(ceil(dcln-(dcln*0.35)));
271.                       dec_dec_signal = decreasing(ceil(dcln-(dcln*0.65)):ceil(dcln-(dcln*0.35)));
272.                       dstd = std(dec_dec_signal);
273.                       decAll_std{cnt7} = dstd;
274.                       w_slope2 = slope_estimation(dec_rtime_x1,dec_dec_y1, dec_rtime_x2,
dec_dec_y2);
275.                       slope_val2{cnt7} = w_slope2;
276.                       cnt7 = cnt7 + 1;
277.                       figure(7);
278.                       subplot(121)
279.                       hold on
280.                       plot( rise_signal );
281.                       title('rising curves')
282.                       hold off
283.                       subplot(122)
284.                       hold on
285.                       plot(dec_dec_signal);
286.                       title('decreasing curves')
287.                       hold off
288.                    end
289.                 end
290.              end
291.              if length(bpIdx)< length(tpIdx)
```

```
292.            len22 = abs(length(bpIdx)- length(tpIdx));
293.            for p = 1:length(tpIdx)-len22
294.               low_res1 = bpIdx(p);
295.               high_res1 = tpIdx(p);
296.               d_low_res = tpIdx(p) ;% window lower resolution
297.               %if length(bpIdx) == length(tpIdx) + 1
298.               d_high_res = bpIdx(p+1) ;% window upper resolution
299.               %end
300.               rising = capacitance(low_res1:high_res1);
301.               decreasing = capacitance(d_low_res:d_high_res);
302.               rising_time = time(low_res1:high_res1);
303.               decreasing_time = time(d_low_res:d_high_res);
304.
305.               % sensitivity estimation
306.               rtime_len = length(rising_time);
307.               rheight_arr = nparticition(sSHight, rtime_len);
308.               rsensitivity = cap_sensitivity(rising, "rise");
309.               dtime_len = length(decreasing_time);
310.               dheight_arr = nparticition(sSHight, dtime_len);
311.               dsensitivity = cap_sensitivity(decreasing, "decrease");
312.
313.
314.               riseh{rcnt}= rheight_arr;
315.               rise_sensi{rcnt}= rsensitivity;
316.               dcrh{dcnt}=  dheight_arr;
317.               dcrh_sensi{dcnt}= dsensitivity;
318.               rcnt=rcnt+1;
319.               dcnt=dcnt+1;
320.               figure(81)
321.               subplot(131)
322.               hold on
323.               plot(rheight_arr, rsensitivity)
324.               axis square
325.               title('Rising sensitivity')
326.               xlabel("Sensor's height")
327.               ylabel("Capacitance Change")
328.               hold off
329.               subplot(132)
330.               hold on
331.               plot(dheight_arr, sort(dsensitivity, 'descend') );
332.               axis square
333.               title('Decreasing sensitivity')
334.               xlabel("Sensor's height")
335.               ylabel("Capacitance Change")
336.               hold off
337.               subplot(133)
338.               hold on
339.               plot(rheight_arr, rsensitivity, dheight_arr, sort(dsensitivity) );
340.               axis square
341.               title('Increasing and Decreasing sensitivity')
342.               xlabel("Sensor's height")
343.               ylabel("Capacitance Change")
```

```
344.                hold off
345.
346.                % plot the increasing and decreasing signal parts separately
347.                figure(8);
348.                subplot(121)
349.                hold on
350.                plot(rising);
351.                title('rising curves')
352.                hold off
353.                subplot(122)
354.                hold on
355.                plot(decreasing);
356.                title('decreasing curves')
357.                hold off
358.                if ~isempty(rising) && ~isempty(rising_time)  &&
~isempty(decreasing_time) && ~isempty(decreasing)
359.                    rcln = length(rising);
360.                    dcln = length(decreasing);
361.                    % rising part
362.                    rise_time_x1 = rising_time(ceil(rcln-(rcln*0.65)));
363.                    rise_time_x2 = rising_time(ceil(rcln-(rcln*0.35)));
364.                    rise_y1 = rising(ceil(rcln-(rcln*0.65)));
365.                    rise_y2 = rising(ceil(rcln-(rcln*0.35)));
366.                    rise_signal = rising(ceil(rcln-(rcln*0.65)):ceil(rcln-(rcln*0.35)));
367.                    rstd = std(rise_signal);
368.                    riseAll_std{cnt6} = rstd;
369.                    w_inc_slope1 = slope_estimation(rise_time_x1, rise_y1, rise_time_x2,
rise_y2);
370.                    slope_val1{cnt6} = w_inc_slope1;
371.                    cnt6 = cnt6 + 1;
372.                    % decreasing part
373.                    dec_rtime_x1 = decreasing_time(ceil(dcln-(dcln*0.65)));
374.                    dec_rtime_x2 = decreasing_time(ceil(dcln-(dcln*0.35)));
375.                    dec_dec_y1 = decreasing(ceil(dcln-(dcln*0.65)));
376.                    dec_dec_y2 = decreasing(ceil(dcln-(dcln*0.35)));
377.                    dec_dec_signal = decreasing(ceil(dcln-(dcln*0.65)):ceil(dcln-(dcln*0.35)));
378.                    dstd = std(dec_dec_signal);
379.                    decAll_std{cnt7} = dstd;
380.                    w_slope2 = slope_estimation(dec_rtime_x1,dec_dec_y1, dec_rtime_x2,
dec_dec_y2);
381.                    slope_val2{cnt7} = w_slope2;
382.                    cnt7 = cnt7 + 1;
383.                    figure(9);
384.                    subplot(121)
385.                    hold on
386.                    plot( rise_signal );
387.                    title('rising curves')
388.                    hold off
389.                    subplot(122)
390.                    hold on
391.                    plot( dec_dec_signal);
392.                    title('decreasing curves')
```

```
393.                     hold off
394.                 end
395.             end
396.         end
397.
398.
399.         if length(bpIdx)== length(tpIdx)
400.             %len33 = abs(length(bpIdx)- length(tpIdx))
401.             for p = 1:length(tpIdx)-1
402.                 low_res1 = bpIdx(p);
403.                 high_res1 = tpIdx(p);
404.                 d_low_res = tpIdx(p) ;% window lower resolution
405.                 %if length(bpIdx) == length(tpIdx) + 1
406.                 d_high_res = bpIdx(p+1) ;% window upper resolution
407.                 %end
408.                 rising = capacitance(low_res1:high_res1);
409.                 decreasing = capacitance(d_low_res:d_high_res);
410.                 rising_time = time(low_res1:high_res1);
411.                 decreasing_time = time(d_low_res:d_high_res);
412.
413.                 % sensitivity estimation
414.                 rtime_len = length(rising_time);
415.                 rheight_arr = nparticition(sSHight, rtime_len);
416.                 rsensitivity = cap_sensitivity(rising, "rise");
417.                 dtime_len = length(decreasing_time);
418.                 dheight_arr = nparticition(sSHight, dtime_len);
419.                 dsensitivity = cap_sensitivity(decreasing, "decrease");
420.
421.
422.                 riseh{rcnt}= rheight_arr;
423.                 rise_sensi{rcnt}= rsensitivity;
424.                 dcrh{dcnt}=  dheight_arr;
425.                 dcrh_sensi{dcnt}= dsensitivity;
426.         %       rcnt=rcnt+1;
427.         %       dcnt=dcnt+1;
428.         color_val=rand(1,3);
429.
430.                 figure(101)
431.                  subplot(121)
432.         %       hold on
433.                 plot(rheight_arr,
(rsensitivity)*1e12,'DisplayName',num2str(rcnt),'Color',color_val)
434.         %       legend(num2str(rcnt))
435.                 hold on
436.                 axis square
437.                 title('Rising Capacitance')
438.                 xlabel("Height (mm)")
439.                 ylabel("Capacitance (pF)")
440.         %       hold off
441.                 legend
442.
443.                 subplot(122)
```

```
444.            %       hold on
445.                    plot(dheight_arr, (sort(dsensitivity,
'descend'))*1e12,'DisplayName',num2str(dcnt),'Color',color_val );
446.            %       legend(num2str(dcnt))
447.                    hold on
448.
449.                    axis square
450.                    title('Decreasing Capacitance')
451.                    xlabel("Height (mm)")
452.                    ylabel("Capacitance (pF)")
453.            %       hold off
454.                     legend
455.
456.                    rcnt=rcnt+1;
457.                    dcnt=dcnt+1;
458.
459.                    figure(10);
460.                    subplot(121)
461.                    hold on
462.                    plot(rising);
463.                    title('rising curves')
464.                    hold off
465.                    subplot(122)
466.                    hold on
467.                    plot(decreasing);
468.                    title('decreasing curves')
469.                    xlabel("Sensor's height")
470.                    ylabel("Capacitance Change")
471.                     hold off
472.                    if ~isempty(rising) && ~isempty(rising_time)  &&
~isempty(decreasing_time) && ~isempty(decreasing)
473.                       rcln = length(rising);
474.                       dcln = length(decreasing);
475.                       % rising part
476.                       rise_time_x1 = rising_time(ceil(rcln-(rcln*0.65)));
477.                       rise_time_x2 = rising_time(ceil(rcln-(rcln*0.35)));
478.                       rise_y1 = rising(ceil(rcln-(rcln*0.65)));
479.                       rise_y2 = rising(ceil(rcln-(rcln*0.35)));
480.                       rise_signal = rising(ceil(rcln-(rcln*0.65)):ceil(rcln-(rcln*0.35)));
481.                       rstd = std(rise_signal);
482.                       riseAll_std{cnt6} = rstd;
483.                       w_inc_slope1 = slope_estimation(rise_time_x1, rise_y1, rise_time_x2,
rise_y2);
484.                       slope_val1{cnt6} = w_inc_slope1;
485.                       cnt6 = cnt6 + 1;
486.                       % decreasing part
487.                       dec_rtime_x1 = decreasing_time(ceil(dcln-(dcln*0.65)));
488.                       dec_rtime_x2 = decreasing_time(ceil(dcln-(dcln*0.35)));
489.                       dec_dec_y1 = decreasing(ceil(dcln-(dcln*0.65)));
490.                       dec_dec_y2 = decreasing(ceil(dcln-(dcln*0.35)));
491.                       dec_dec_signal = decreasing(ceil(dcln-(dcln*0.65)):ceil(dcln-(dcln*0.35)));
492.                       dstd = std(dec_dec_signal);
```

```
493.                     decAll_std{cnt7} = dstd;
494.                     w_slope2 = slope_estimation(dec_rtime_x1,dec_dec_y1, dec_rtime_x2,
dec_dec_y2);
495.                     slope_val2{cnt7} = w_slope2;
496.                     cnt7 = cnt7 + 1;
497.                     figure(11);
498.                     subplot(121)
499.                     hold on
500.                     plot( rise_signal );
501.                     title('rising curves')
502.                     hold off
503.                     subplot(122)
504.                     hold on
505.                     plot( dec_dec_signal);
506.                     title('decreasing curves')
507.                     hold off
508.                 end
509.               end
510.           end
511.           slope_incr = cell2mat(slope_val1);
512.           slope_dec = cell2mat(slope_val2);
513.           inc_std = std(slope_incr);
514.           dec_std = std(slope_dec);
515.
516.           slope_rSTD = cell2mat(riseAll_std);
517.           slope_dSTD = cell2mat(decAll_std);
518.           disp('STD of Rising Signal:')
519.           disp(slope_rSTD)
520.           disp('STD of decreasing Signal:')
521.           disp(slope_dSTD)
522.           disp('SNR:')
523.           disp(SNR_sig)
524.
525.           figure(12);
526.           subplot(5,1,1)
527.           plot(time,capacitance);
528.           hold on
529.           plot(time(tpIdx),capacitance(tpIdx),'c*');
530.           plot(time(bpIdx),capacitance(bpIdx),'r*');
531.           subplot(5,1,2)
532.           plot(slope_incr_11, '--')
533.           subplot(5,1,3)
534.           plot(slope_incr_11, '--')
535.           subplot(5,1,4)
536.           plot(slope_incr, '--o')
537.           title('Rise STD:', num2str(inc_std))
538.           subplot(5,1,5)
539.           plot(slope_dec, '--o')
540.           title('Decrease STD:', num2str(dec_std))
541.           hold off
542.           figure(13);
543.            plot(riseh{1},rise_sensi{1}*1e12,"r",dcrh{1},sort(dcrh_sensi{1})*1e12,"b")
```

```
% plot(riseh{1},rise_sensi{1}*1e12,"r")
axis square
title('sensitivity')
xlabel("Height (mm)")
ylabel("Capacitance (pF)")
hold off

%% per unit area sensitivity calculation
%
sensi_slope_r= {};
sensi_slope_d= {};
len_r=length(rise_sensi);
len_d= length(dcrh_sensi);

for ii=1:1:len_r
rise_sensitivity_per_unit_height= (max(rise_sensi{ii})-min(rise_sensi{ii}))/sSHight;
sensi_slope_r{ii}=rise_sensitivity_per_unit_height;
end


for ii=1:1:len_d
dcr_sensitivity= (max(dcrh_sensi{ii})-min(dcrh_sensi{ii}))/sSHight;
sensi_slope_d{ii}=dcr_sensitivity;
end
sensi_r_mat=cell2mat(sensi_slope_r)
sensi_d_mat=cell2mat(sensi_slope_d)
```

%%
%%%%%%% Function name: SignallocalPeakfinder.m %%%%%%%%%%%%%

```
function [topPeaks, topIdx, bottomPeaks, bottomIdx] = signallocalPeakFinder(s1, s2, w)
% Local top and bottom peaks finder
%Author:
%Date:
% Parameters:
% s1: nx1 array, original signal, however, if we call multiple time to
% refine the location of the peaks, then s1: (n-m)x1, each time n matrix will reduce a scaler, m
% s2: nx1, original signal.
% outputs:
% Peaks values and their corresponding indexs,
%%%%%%%%%%%%%%%%%%%%%%%%%%%%
res_high = w;
max_re = {}; % cell array, it is similar to python list
max_idx = {};
min_re = {};
min_idx = {};
counter = 1;
res_high_incr = 0;
```

```
signal1 = s1;
signal2 = s2;
if nargin
for ii = 1:res_high: length(signal1)-(res_high+1)
res_high_incr = ii + res_high;
patch = signal1(ii:res_high_incr);
max_val = max(patch);
max_re{counter} = max_val;
max_idx{counter} = find(signal2==max_val);
min_val = min(patch);
min_re{counter} = min_val ;
min_idx {counter} = find(signal2==min_val);
counter = counter + 1;
end

min_idx2 = {};
max_idx2 = {};
for jj = 1: length(min_idx)
min_idx_val = min_idx{jj};
max_idx_val = max_idx{jj};
if length(min_idx_val)>1
min_idx2{jj} = min(min_idx_val);
else
min_idx2{jj} = min_idx_val;
end

if length(max_idx_val)>1
max_idx2{jj} = min(max_idx_val);
else
max_idx2{jj} = max_idx_val;
end
end
bottomPeaks = cell2mat(min_re)';
topPeaks = cell2mat(max_re)';
bottomIdx = cell2mat(min_idx2)';
topIdx = cell2mat(max_idx2)';
end
```

%%%%%%%%%%%%% Function name: next_min_max.m %%%%%%%%%%%%%

```
function [rtop_Peaks1, rbottom_Peaks1, rtop_idx1, rbottom_idx1  ] =
next_min_max(osignal, topPeaks, bottomPeaks, howManyNeighbor)

reco_max = {};
first_top = 0;
mall_top = 0;
top_cnt = 1;
for ii = 1: length(topPeaks)
if ii == howManyNeighbor + 10

for jj = 3:1: howManyNeighbor + 10
```

```
%disp(ii)
%disp(jj)
if topPeaks(1) - topPeaks(ii-(jj-1))> 0
    a. %disp(jj)
    b. first_top = first_top +1;
end
end
if first_top == howManyNeighbor + 10
%disp(first_top)
reco_max{top_cnt} = topPeaks(1) ;
top_cnt = top_cnt + 1;
first_top = 0;
end
end

if ii == length(topPeaks)

for kk = length(topPeaks)-1: -1: length(topPeaks) - howManyNeighbor
if topPeaks(1) - topPeaks(kk)< 0
    a. first_top = first_top +1;
end
end
if first_top == howManyNeighbor
reco_max{top_cnt} = topPeaks(length(topPeaks)) ;
top_cnt = top_cnt + 1;
first_top = 0;
end
end

if ii > howManyNeighbor +1 && ii< length(topPeaks) - (howManyNeighbor + 1)
for aa = 2: howManyNeighbor +1
if topPeaks(ii)-topPeaks(ii+aa)>0 && topPeaks(ii) - topPeaks(ii-aa)>0
    a. mall_top = mall_top + 1;
end
end
if mall_top >= (howManyNeighbor*0.95)
%disp(mall_top)
reco_max{top_cnt} = topPeaks(ii).
top_cnt = top_cnt + 1;
mall_top = 0;
end
end
end
tpeaks = cell2mat(reco_max);
tavg = mean(tpeaks);
rtop_Peaks = {};
rtop_idx  = {};
tpcnt = 1;
for nn = 1:length(tpeaks)
top_idx = find(osignal==tpeaks(nn));
if length(top_idx) > 1
for jj = 1: length(top_idx)
```

```
54. if osignal(top_idx(jj)) > tavg
        a. if osignal(top_idx(jj)) - osignal(top_idx(jj)-1) > 0 && osignal(top_idx(jj)) -
           osignal(top_idx(jj)+1) > 0 && osignal(top_idx(jj)) - osignal(top_idx(jj)-2) > 0 &&
           osignal(top_idx(jj)) - osignal(top_idx(jj)+2)>0
        b. rtop_Peaks{tpcnt} = osignal(top_idx(jj));
        c. rtop_idx{tpcnt} = top_idx(jj);
        d. tpcnt = tpcnt + 1;
        e. end
55. end

56. end

57. else
58. if osignal(top_idx) > tavg
59. if osignal(top_idx) - osignal(top_idx-1) > 0 && osignal(top_idx) - osignal(top_idx+1) > 0
    && osignal(top_idx) - osignal(top_idx-2) > 0 && osignal(top_idx) - osignal(top_idx+2)>0
        a. rtop_Peaks{tpcnt} = osignal(top_idx);
        b. rtop_idx{tpcnt} = top_idx;
        c. tpcnt = tpcnt + 1;
60. end
61. end
62. end
63. end

64. reco_min = {};
65. first_bot = 0;
66. bot_cnt = 1;
67. mall_bot = 0;

68. for ii = 1:length(bottomPeaks)
69. if ii == howManyNeighbor +10

70. for jj = 3:1: howManyNeighbor +10
71. %disp(ii)
72. %disp(jj)
73. if bottomPeaks(1) - bottomPeaks(ii-(jj-1))< 0
        a. %disp(jj)
        b. first_bot = first_bot +1 ;
74. end
75. end
76. if first_top >= (howManyNeighbor +10)*0.75
77. %disp(first_top)
78. reco_min{bot_cnt} = bottomPeaks(1) ;
79. bot_cnt = bot_cnt + 1;
80. first_bot = 0;
81. end
82. end

83. if ii == length(bottomPeaks)
84. %disp(ii)
85. for kk = (length(bottomPeaks)-1):-1: (length(bottomPeaks) - (howManyNeighbor + 10))
86. % disp(kk)
```

```
87. if bottomPeaks(length(bottomPeaks)) - bottomPeaks(kk)< 0
        a. first_bot = first_bot +1 ;
88. end
89. end
90. if first_bot >= (howManyNeighbor + 10)*0.50
91. reco_min{bot_cnt} = bottomPeaks(length(bottomPeaks)) ;
92. bot_cnt = bot_cnt + 1;
93. first_bot = 0;
94. end
95. end

96. if ii > howManyNeighbor +1 && ii< length(bottomPeaks) - (howManyNeighbor + 1)
97. for aa = 2: howManyNeighbor +1
98. if bottomPeaks(ii)-bottomPeaks(ii+aa)<0 && bottomPeaks(ii) - bottomPeaks(ii-aa)<0
        a. mall_bot = mall_bot + 1;
99. end
100.        end
101.        if mall_bot >= (howManyNeighbor*0.9)
102.        %disp(mall_top)
103.        reco_min{bot_cnt} = bottomPeaks(ii);
104.        bot_cnt = bot_cnt + 1;
105.        mall_bot = 0;
106.        end
107.        end
108.        end
109.        bpeaks = cell2mat(reco_min);
110.        bavg = mean(bpeaks);
111.        bmin = min(bpeaks);
112.        rbot_Peaks ={};
113.        rbot_idx  = {};
114.        bcnt = 1;
115.        for nn = 1:length(bpeaks)
116.        bot_idx = find(osignal==bpeaks(nn));
117.        if length(bot_idx) > 1
118.        for jj = 1:length(bot_idx)
119.        if osignal(bot_idx(jj)) < (bavg + bmin*2)
        a. if osignal(bot_idx(jj)) - osignal(bot_idx(jj)-1) < 0 && osignal(bot_idx(jj)) -
           osignal(bot_idx(jj)+1) < 0 && osignal(bot_idx(jj)) - osignal(bot_idx(jj)-2) < 0 &&
           osignal(bot_idx(jj)) - osignal(bot_idx(jj)+2)<0
        b. rbot_Peaks{bcnt} = osignal(bot_idx(jj));
        c. rbot_idx{bcnt} = bot_idx(jj);
        d. bcnt = bcnt + 1;
        e. end
120.        end

121.        end

122.        else
123.        if osignal(bot_idx) < (bavg + bmin*2)
124.        if osignal(bot_idx) - osignal(bot_idx-1) < 0 && osignal(bot_idx) -
    osignal(bot_idx+1) < 0 && osignal(bot_idx) - osignal(bot_idx-2) < 0 && osignal(bot_idx)
    - osignal(bot_idx+2)<0
```

```
        a.  rbot_Peaks{bcnt} = osignal(bot_idx);
        b.  rbot_idx{bcnt} = bot_idx;
        c.  bcnt = bcnt + 1;
125.      end
126.      end
127.      end
128.      end
129.      rtop_Peaks1 = cell2mat(rtop_Peaks);
130.      rbottom_Peaks1 = cell2mat(rbot_Peaks);
131.      rtop_idx1 = cell2mat(rtop_idx)';
132.      rbottom_idx1 = cell2mat(rbot_idx)';
133.      end
```

%%%%%%%%%%%% Function name: global_peaks.m %%%%%%%%%%%%
%%

```
function [gtop_peaks, gbot_peaks, gtIdx, gbIdx] = global_peaks(osignal, topPeaks, botPeaks,
topIdx, botIdx)

1.  tpks = {};
2.  tcnt = 1;
3.  bpks = {};
4.  bcnt = 1;
5.  distance = {};
6.  all_neighbor = {};
7.  all_cnt = 1;
8.  tmin = min(topIdx);
9.  tmax = max(topIdx);
10. bmin = min(botIdx);
11. bmax = max(botIdx);
12. topIdx = unique(topIdx);
13. botIdx = unique(botIdx);
14. if length(topIdx) > length(botIdx)
15. all_idx = topIdx;
16. for ii = 1:length(botIdx)
17. all_idx(end+1) = botIdx(ii);
18. end
19. end
20. if length(topIdx) < length(botIdx)
21. all_idx =botIdx;
22. for ii = 1:length(topIdx)
23. all_idx(end+1) = topIdx(ii);
24. end
25. end
26. if length(topIdx) == length(botIdx)
27. all_idx =botIdx;
28. for ii = 1:length(topIdx)
29. all_idx(end+1) = topIdx(ii);
30. end
31. end

32. order_all_idx = sort(all_idx);
```

```
% length(order_all_idx)
% length(topIdx)
% length(botIdx)
bst_peaks = {};
bst_cnt = 1;
% if bmin < tmin
temp_bpk = {};
tmp_bcntr = 1;
for ii = 1:length(botIdx)
idx_val = botIdx(ii);
bot_idx_order = find (order_all_idx == idx_val);
temp_bpk{tmp_bcntr} = bot_idx_order;
tmp_bcntr = tmp_bcntr + 1;
end
%temp_bpk

temp_tpk = {};
tmp_tcntr = 1;
for ii = 1:length(topIdx)
idx_val = topIdx(ii);

bot_idx_order = find (order_all_idx == idx_val);
for jj = 1:length(bot_idx_order)
temp_tpk{tmp_tcntr} = bot_idx_order;
tmp_tcntr = tmp_tcntr + 1;
end
end
%temp_bpk
if bmin < tmin
tmp_bpk = cell2mat(temp_bpk);
for jj = 1:length(tmp_bpk)
brng1 = tmp_bpk(jj) ;
if jj < length(tmp_bpk)
brng2 = tmp_bpk(jj+1);
end
if jj > 1 &&jj< length(tmp_bpk)
tval = order_all_idx(brng1+1:brng2-1);
else
tval = order_all_idx(brng1+1:end);
end
if length(tval) >0
tpks{tcnt} = tval;
tcnt = tcnt + 1;
end

end

%tpks{end}
tmp_tpk = cell2mat(temp_tpk);

for jj = 1:length(tmp_tpk)
```

```
79. if jj == 1
80. trng1 = tmp_tpk(jj);
81. end
82. if jj > 1 && jj<length(tmp_tpk)
83. trng1 = tmp_tpk(jj);
84. trng2 = tmp_tpk(jj+1);
85. end
86. if jj == length(tmp_tpk)
87. trng1 = tmp_tpk(jj);
88. end
89. if jj == 1
90. bval = order_all_idx(1:trng1-1);
91. end
92. if jj > 1 && jj<length(tmp_tpk)
93. bval = order_all_idx(trng1+1:trng2-1);
94. end
95. if jj == length(tmp_tpk)
96. bval = order_all_idx(trng1+1:end);
97. end
98. if length(bval) >0
99. bpks{bcnt} = bval;
100.        bcnt = bcnt + 1;
101.        end
102.        end
103.        end

104.        if bmin > tmin
105.        tmp_bpk = cell2mat(temp_bpk);
106.        for jj = 1:length(tmp_bpk)
107.        if jj == 1
108.        brng1 = tmp_bpk(jj);
109.        end
110.        if jj > 1 && jj < length(tmp_bpk)
111.        brng1 = tmp_bpk(jj);
112.        brng2 = tmp_bpk(jj+1);
113.        end
114.        if jj == length(tmp_bpk)
115.        brng1 = tmp_bpk(jj);
116.        end
117.        if jj == 1
118.        tval = order_all_idx(1:brng1 -1);
119.        if jj> 1 && jj< length(tmp_bpk)
        a.  tval = order_all_idx(brng1+1:brng2-1);
120.        end
121.        if jj == length(tmp_bpk)
        a.  tval = order_all_idx(brng1+1:end);
122.        end
123.        if length(tval) >0
        a.  tpks{tcnt} = tval;
        b.  tcnt = tcnt + 1;
124.        end
```

```
125.        end

126.        tmp_tpk = cell2mat(temp_tpk);

127.        for jj = 1:length(tmp_tpk)
128.        if  jj<length(tmp_tpk)
        a.   trng1 = tmp_tpk(jj);
        b.   trng2 = tmp_tpk(jj+1);
129.        end
130.        if jj == length(tmp_tpk)
        a.   trng1 = tmp_tpk(jj);
131.        end
132.        if  jj<length(tmp_tpk)
        a.   bval = order_all_idx(trng1+1:trng2-1);
133.        end
134.        if jj == length(tmp_tpk)
        a.   bval = order_all_idx(trng1+1:end);
135.        end
136.        if length(bval) >0
        a.   bpks{bcnt} = bval;
        b.   bcnt = bcnt + 1;
137.        end
138.        end
139.        end
140.        end
141.        fbpeaks = {};
142.        fbpeak_idx = {};
143.        fbcnt = 1;
144.        for ii = 1:length(bpks)
145.        tm_fbpks = {};
146.        tm_fbcnt = 1;
147.        tmp_bpks = bpks{ii};
148.        for jj = 1:length(tmp_bpks)
149.        tmp_bidx = tmp_bpks(jj);
150.        tmp_capb = osignal(tmp_bidx);
151.        tm_fbpks{tm_fbcnt} = tmp_capb ;
152.        tm_fbcnt = tm_fbcnt + 1;
153.        end
154.        tm_fbpks_ar = cell2mat(tm_fbpks);
155.        tmp_bpks_cap_val = max(tm_fbpks_ar);
156.        min_bpIdx  = find( tm_fbpks_ar == tmp_bpks_cap_val);
157.        if length(min_bpIdx) > 1
158.        %for kk = 1:length(min_bpIdx)
159.        fbpks_idx = tmp_bpks(min_bpIdx(1)) ;
160.        %end
161.        else
162.        fbpks_idx = tmp_bpks(min_bpIdx) ;
163.        end
164.        fbpeaks{fbcnt} =  tmp_bpks_cap_val;
165.        fbpeak_idx{fbcnt} = fbpks_idx;
166.        fbcnt = fbcnt + 1;
167.        end
```

```
168.        ftpeaks = {};
169.        ftpeak_idx = {};
170.        ftcnt = 1;
171.        for ii = 1:length(tpks)
172.        tm_ftpks = {};
173.        tm_ftcnt = 1;
174.        tmp_tpks = tpks{ii};
175.        for jj = 1:length(tmp_tpks)
176.        tmp_tidx = tmp_tpks(jj);
177.        tmp_capt = osignal(tmp_tidx);
178.        tm_ftpks{tm_ftcnt} = tmp_capt ;
179.        tm_ftcnt = tm_ftcnt + 1;
180.        end
181.        %tm_fbpks
182.        tm_ftpks_ar = cell2mat(tm_ftpks);
183.        tmp_tpks_cap_val = max(tm_ftpks_ar);
184.        min_tpIdx  = find(tm_ftpks_ar == tmp_tpks_cap_val);
185.        if min_tpIdx > 1
186.        %for kk = 1:length(min_tpIdx)
187.        ftpks_idx = tmp_tpks(min_tpIdx(1)) ;
188.        %end
189.        else
190.        ftpks_idx = tmp_tpks(min_tpIdx);
191.        end
192.        ftpeaks{ftcnt} =  tmp_tpks_cap_val;
193.        ftpeak_idx{ftcnt} = ftpks_idx;
194.        ftcnt  = ftcnt + 1;
195.        end
196.        gtop_peaks = cell2mat(ftpeaks);
197.        gbot_peaks = cell2mat(fbpeaks)';
198.        gtIdx = unique(sort(cell2mat(ftpeak_idx)'));
199.        gbIdx = unique(sort(cell2mat(fbpeak_idx)'));
200.        end
```

%%%%%%%%%%% Function name: slope_estimation.m %%%%%%%%%

```
1.  function  slope = slope_estimation(x1, y1, x2, y2)
2.  % slope estimation
3.  % Author:
4.  % Date :
5.  % Inputs:
6.  % x1, x2, y1, y2: scalar values
7.  slope = (y2 - y1) / (x2 - x1); % tan(theta) = (y2-y1) / (x2-x1)
8.  end
```

%%%%%%%%%%% Function name: nparticition.m %%%%%%%%%%%%

```
function arr = nparticition(num, len) %% time stamp was converted to height
        1.  portion = num / len;
```

```
2.  all_portion = {};
3.  add_portion = 0;
4.  for ii = 1:1:len
5.  if ii ==1
6.  all_portion{ii} = portion;
7.  add_portion = portion;
8.  else
9.  add_portion = add_portion + portion;
10. all_portion{ii} = add_portion;
11. end
12. end
13. arr = cell2mat(all_portion);
14. end
```

%%%%%%%%%% Function name: cap_sensitivity.m %%%%%%%%%%%%%%%%%

```
1.  function cap_sen = cap_sensitivity(cap_arr, att)
2.  sen_cell = {};
3.  if att == "rise"
4.  for ii = 1:1:length(cap_arr)-1
5.  val2 = cap_arr(ii+1);
6.  val1 = cap_arr(1);
7.  diff = val2 - val1 ;
8.  sen_cell{ii} = diff;
9.  end
10. sen_arr = cell2mat(sen_cell);
11. cap_sen = [0, sen_arr];
12. end
13.
14. if att == "decrease"
15. %     cnt = 1;
16. for ii = 1:1:length(cap_arr)-1
17. val2 = cap_arr(ii+1);
18. val1 = cap_arr(1);
19. diff = abs(val1 - val2) ;
20. sen_cell{ii} = diff;
21. %         cnt = cnt + 1;
22.     end
23. sen_arr = cell2mat(sen_cell);
24. cap_sen = [ sen_arr, 0];
25. end
```